MODEL BASED CUTTER ANALYSIS AND EVALUATION
IN
MILLING TITANIUM ALLOYS

by

Hsin-Yu Kuo

A dissertation submitted in partial fulfillment
of the requirements for the degree of
Doctor of Philosophy
(Mechanical Engineering)
in The University of Michigan
2011

Doctoral Committee Members:

Professor Jun Ni , Chair
Professor James R. Barber
Professor J. Wayne Jones
David A. Stephenson, Ford Motor Company

ACKNOWLEDGEMENTS

I would like to express my sincere gratitude to my advisor Professor Jun Ni for his guidance, advice, and support of my research. Without him, I would not even have a chance to study in the Ph.D. program and start this research topic at the University of Michigan. I am grateful to my dissertation committee members, Professor James Barber, Professor Wayne Jones and Doctor David Stephenson for devoting their precious time to giving me advice and reviewing this dissertation. Thanks for Jaewook Oh for helping me with experiments and providing precious knowledge related to the research. I also appreciate the discussions with Adam Brzezinski, not only in technical area but also the language and cultural issues I had in the past few years.

I would also like to thank the sponsors of this research, GE Aviation. Special thanks go to Roger Lindle, the patient project leader. Howard Weaver and John Pfeiffer provided me their experience in the machining area and helped me to relate the industrial need with academic world. Last but not least, special thanks to Kevin Meyer, without his works and efforts, this work would not have been possible to be initiated and completed.

Finally, I would like to thank the support from my family, and the companion of my lab mates and friends during the five years of PhD study.

TABLE OF CONTENTS

LIST OF FIGURES

LIST OF TABLES

CHAPTER 1
INTRODUCTION

1.1 Overview

In recent years, the improvement of aircraft engines has depended on the properties of materials. Because of the extreme working environment of aviation engines, material properties such as wear resistance and thermal capacity are very important. Moreover, the requirement of making light and small engines also makes the density and strength of material important considerations. Among all the choices, titanium alloy has become one of the most widely used materials in the aerospace industry.

Titanium alloy is a suitable material in the aerospace industry because it has all the required properties. First, it has very high strength-to-weight ratio. This property makes titanium alloy a lightweight material with high strength. Second, it has very high mechanical resistance, a property that can result in lengthened engine life. Furthermore, it has high strength at elevated temperatures, a property that enables it to stand the aircraft engine environment. However, titanium is classified as a difficult-to-cut material because of its several inherent properties. The first of these, its low thermal conductivity increases the temperature at the tool/ workpiece interface, which affects tool performance dramatically. The second, its high chemical reactivity causes problems of material bonding and chip evacuation, which commonly leads to severe tool failure. Finally, its high strength at elevated temperatures, although it has been mentioned above as one advantage, requires extremely large cutting forces and power, which leads to several difficulties during the machining process. Thus, the machining of titanium alloy has become an important issue in both industial and academic field.

Milling is considered a critical process not only because it can remove the unwanted part of materials efficiently, but also because it can create almost all kinds of contour surfaces smoothly. However, milling is a very complicated machining process. It is a discontinuous cutting process with varying chip load, forces and heat generation. Moreover, the tool geometry in milling is complex. Along the milling tool edges, the rake and clearance angles vary with respect to the distance from the milling tool tip. For the ball-end mills, the cutting velocity and chip load also vary because of the increasing radius along the edges. Therefore, the analysis of milling process and milling tool performance is always a big challenge.

Milling titanium alloys has drawn attention because of two main reasons. First, they are used for manufacturing high-end parts, not just components used in aerospace industry, but also medical parts, for example. Second, a broader reason for covering titanium milling relates to the procedures for machining effectively when the material is difficult to cut or the available speed is low (Zelinski , 2004). The combination of titanium alloys and milling process leads to two damaging factors: the high temperature and the high cutting pressures. A large amount of heat generated during the cutting process conducts to the tool instead of the chips or workpiece due to the low thermal conductivity of titanium alloys. The high temperature in the tool not only degrades the tool properties but also results in thermal stress and causes excessive damage to the tool.

The high cutting pressure is another major damaging factor to the tool when milling titanium alloys. This might be attributed to the extraordinary small chip-tool contact area on the rake face because small chip load is always preferred in order to lengthen the tool life (Ezugwu and Wang, 1997). The difficulty in milling titanium alloys makes the selection of cutting tool material very critical. Straight tungsten carbide (WC-Co) is generally suggested to be the most appropriate cutting tool material in machining titanium alloys (Ezugwu and Wang, 1997, Zelinski, 2004). The combination of high hardness tungsten carbide grains and the high toughness cobalt binder has proven its superiority in titanium machining process.

Experimental approach is still the dominant method to investigate the tool performance in titanium milling process. Numerous studies focused on testing for different cutting conditions (López et al., 2000, Ginting and Nouari, 2006, Haron et al., 2007, Geng and Xu, 2009); some works concerned the cutter geometry at the tip of the cutting edge (Komanduri and Reed, 1983) and limited works have been done to analyze the flute geometry in the milling tools (Lu et al., 2005). However, experimental investigations are time-consuming and costly due to the high cost of titanium alloys (Froes, 2007). With proper modeling methods, the tool performance in the titanium milling process can be analyzed in a more efficient way. Moreover, the modeling approach provides higher flexibility to evaluate different tool designs and cutting conditions without the necessity to produce the tool and test in real cutting process.

1.2 Research Objective

1.2.1 Research Objective and Scope

The objective of this study is to develop models for evaluating tool performance in milling titanium alloy. The developed models require only calibration and validation experiments therefore it is economic and efficient. It is expected that through the modeling technique developed in this study, the tool performance can be analyzed under different cutting conditions. Moreover, the new tool designs can be evaluated by the models instead of the time-consuming and costly cutting tests.

To achieve the ultimate research goal, the study focuses on several models for analyzing the milling process. Each of the models has been studied to some extent by other researchers; however, the current study improves upon the previous works by integrating more realistic factors closely related to the milling process. The first model is for predicting cutting force, which is one of the most important factors that affect the whole cutting process and the tool performance. The second model is for the cutting temperature estimation. High cutting temperature is always concerned as a major issue in titanium milling process, and the lack of appropriate measurement technique in milling makes temperature a big unknown in this field. The third model is to estimate the progression of wear and use it as an indicator to predict the milling tool life. Finally, a stress calculation model is proposed to analyze the stress distribution along the milling tool flutes and for evaluating the cutter design. Each of the models is important for understanding the cutting process and for evaluating the tool performance in the milling of titanium alloys.

1.2.2 The Research Outlines

This dissertation contains six Chapters.

Chapter 1 presents the motivation and objectives of this study. The poor machinability of titanium alloys calls for more investigation on their machined process, but their high cost limits the possibility of more experimental study. A brief review shows the important parameters which affect tool performance and the disadvantage of experimental approaches. Thus, proper modeling methods replacing the experimental approach can improve the titanium milling technique by avoiding the expenses of costly materials.

Chapter 2 is devoted to the construction of the mechanistic force model. The model is based on existing literature with the improvement of a novel chip thickness calculation method, which enables the model to predict cutting forces with arbitrary tool geometry. The tool geometry is extracted directly from the CAD model including the varying rake and clearance angle along the cutting edge. Moreover, the effect of tool wear is also covered in the model. The forces at the wear land are added to the forces of the sharp tool and the cyclic forces during milling process are modeled. The most important of all, the calculated cutting forces in this chapter are the basis for all the models in the following chapters.

Chapter 3 focuses on the temperature modeling technique for milling process. The cyclic forces result in varying heat generation during the cutting process. At the same time, the changing chip thickness and tool-chip contact length lead to the varying area of heat flows into the tool. In this study, the heat flows in both the space and time domains are discretized piecewise to consider the varying cutting parameters during milling process. The effects of coolant and tool wear are both considered in the model. Finally, a tool-foil thermocouple technique has been designed to measure cutting temperature in the milling tests.

Chapter 4 proposes an integrated model that combines the existing tool wear model and the cutting force model for tool wear progression estimation. When there is flank wear appearance, extra forces are generated on the flank wear area. The increasing force results in more tool wear. With the iteration between the tool wear and the forces, the flank wear progression along with cutting time is estimated. Flank wear is commonly used as the criterion to determine whether the tool life is reached or not. Thus, with the proposed model, the tool lives under different cutting conditions are estimated and validation experiments are conducted.

Chapter 5 considers another parameter which also leads to tool failure, the stress in the tool. The wedge-shaped elemental cutting tool is decomposed into two half-space loading problem, one on the rake surface and the other on flank. Boundary element method is used to solve the real loads on both surfaces. Finally, the stress in the tool is the summation of the thermal stress and the mechanical stress from the real loads on both surfaces and. The modeling results have been shown and discussed. Brittle fracture analysis is used to analyze the stress distribution along the milling tool edge. Tool chipping has been observed at the location where the model identifies as high stress concentration points.

Chapter 6 is the conclusion which summarizes the research works that have been finished and provides the directions for the future works.

CHAPTER 2

INTEGRATED FORCE MODEL FOR ARBITRARY TOOL GEOMETRY WITH FLANK WEAR

2.1 Nomenclature

A_c	chip area
DOC_t	axial depth of cut in turning
F_{cut}	cutting force of elemental cutting tool (ECT)
F_{cw}	friction force on flank surface due to tool wear
F_f	friction force on rake surface of ECT
F_{lat}	lateral force of ECT
F_n	normal force on rake surface of ECT
F_{th}	thrust force of ECT
F_{tw}	normal force on flank surface due to tool wear
f	feed rate in milling
f_t	feed rate in turning
h	height of cone
K_f	specific friction force

K_n	specific normal force
L	width of cutting edge of ECT
N_{teeth}	number of cutting edge flutes on the cutter
R	radius of cone
R_t	radius of turning insert
t_c	uncut chip thickness
V	cutting velocity
VB	flank wear width
$VB*$	critical wearland width
α_n	normal rake angle of ECT
α_t	rake angle of turning insert
β_n	angle position of ECT on turning insert
η_c	chip flow angle of ECT
θ	clearance angle of ECT
λ	oblique angle of ECT
μ	friction coefficient between the tool and workpiece
σ_0	tool tip normal stress of ECT
τ_0	tool tip shear stress of ECT
ϕ	angle of the cone
δ_1	the first engagement angle on turning insert
δ_2	the second engagement angle on turning insert

ω spindle speed

2.2 Introduction

Titanium alloys are high strength material, which means that they require more energy to be deformed. The more energy required for material to be cut, the larger cutting forces the tool experiences during the machining process. Moreover, large cutting forces might result in chatter, tool deflection, and other instability of the cutting system. All these factors affect the tool performance, the cutting efficiency and the product quality. Therefore, it is very important to know the forces for controlling the machining process and analyzing the tool performance.

Cutting force modeling has been studied and researched for more than fifty years. In early days, the forces were often estimated from machinability handbooks or database. This approach is generally reliable, but a large amount of experimental data must be gathered according to various tool materials, workpiece materials, and under different cutting conditions. Therefore, an alternative approach is to develop models for analyzing those complex cutting processes through machining theory. As the understanding of the mechanism of metal-cutting processes improved, analytical models for orthogonal and oblique cutting were developed (Merchant, 1944, Shaw et al., 1952, Oxley, 1961).

Pure analytical approach modeled the forces from a theoretical view point; therefore, it might not capture the realistic issues. Moreover, when it comes to milling, the complicated cutter geometry and the varying cutting condition along the flutes make pure analytical approach difficult to be applied. Thus, mechanistic models have become the most commonly used method for modeling the forces in milling. In this study, mechanistic approach has been used for developing the model. The previous works of cutting force model are reviewed and the limitations of existing models are discussed. A cutting force model of sharp tool is proposed by extending the existing model. Moreover, the forces due to flank wear are added to the forces of sharp tool to model those of worn tool. Validation experiments for the cutting forces of both sharp and worn tools have been conducted at the end of the study.

2.3 Literature Review

2.3.1 Mechanistic Force Model of Sharp Tool

Mechanistic models have become popular for the prediction of cutting force in recent years. The mechanistic approach used the basic concept of the analytical models, and obtained the specific cutting force from empirical equations related to fundamental cutting parameters. Thus it not only covered the theoretical side by including the most important parameters in the empirical equations, but also considered the practical issue by obtaining the coefficients in real cutting experiments. The determination of the empirical equations was studied extensively (Feng and Menq, 1993, Lee and Altintas, 1995, Arsecularatne and Oxley, 1997, Yun and Cho, 2001, Wang and Zheng, 2002, Zhang et al., 2005). Several combinations of parameters have been used to construct the empirical equations, and the coefficients needed to be determined when cutting different materials.

When researchers applied the mechanistic models to the milling processes, the complicated cutter geometry became an important issue. DeVor and his coworkers (1980, 1982, 1984) were one of the first groups to develop a mechanistic model for the prediction of cutting force in end milling. The end-mill was divided into layers of disc-like elements, and the forces on each layer were calculated from empirical equations. All the forces were aggregated to give the total cutting force on the cutter. This discretization concept has been applied to most mechanistic models of milling force in later researches.

However, in order to discretize the cutting edge, the tool geometry needs to be defined first. In DeVor et al.'s works, the cutting edge was described by a function of the number of flutes, angular position of the cutter, and the helix angle of the flutes. The tool geometry is limited to be constant helix angle and identical profile for all the flutes, and it is not applicable for more complicated-shape mills, such as the ball-end mill. Yang and Park (1991) assumed the cutting edge on the ball-end mill as a function of the cutter radius, normal rake angle and angle of the point in the spherical coordinate. Tai and Fuh (1994, 1995) composed the ball-end mill into the ball part and end-mill part, which means, the profile is regarded as the combination of a cylindrical surface and a semi-spherical surface mounted on the tip end of the cylindrical surface. All these methods limited the cutter geometry into "perfect" ball shape, and also, identical flutes. Chiang et al. (1995) measured the cutting edge profile using a three-dimensional coordinate measurement machine, and obtained a fourth order equation for describing the edge. The accuracy depended a lot on the measurement technique, and the fourth order approximation equation could not perfectly represent the real tool geometry.

Altintas and his coworkers did a series of studies about the mechanics and dynamics of milling process, and developed a new mechanistic model to predict milling force. First, Yucesan and Altintas (1996) developed a model for the cutter geometry. The flutes of the ball-end cutter met at the tip of the sphere, and were ground with a constant helix. Due to the reduction of radius at the ball part, the local helix angle along the cutting flute reduced proportionally. At the same time, the reduction of radius was proportional to the lag angle, which was the angle between the tip of flute and the cutting edge point. Thus, the geometry of the cutter could be simply represented by a function of lag angle. Later on, Budak et al. (1996) constructed the empirical equations based on both mechanistic theory and experimental evaluation. The cutting forces for each elemental cutting tool were modeled in terms of two fundamental phenomena, an edge force component due to rubbing or ploughing at the cutting edge, and a cutting component due to shearing at the shear zone and friction at the rake face. The milling force coefficients in the empirical equations could be obtained from the oblique cutting analysis and the orthogonal cutting data base. With the use of the geometry model and empirical equations, Lee and Altintas (1995) constructed a complete model for the prediction of ball-end milling forces from orthogonal cutting data. After several years of studying on the milling process, Engin and Altintas (2001) summarized different shapes of mills, and developed a general geometric model for describing all the mills. They used several geometric parameters to define the milling cutters, and then used a helical cutting edge to wrap round the end-mill geometry to define the flutes. Their model indeed covered most of the end-mills currently used in industry. However, the model is still limited by the existing classification of the tool geometry and the defined parameters which describe that.

Moreover, in the model all the flutes are still assumed to be the same, and the helix angle remains constant. Another issue the existing models did not consider is the rake and clearance surface of the cutters. Because of the curvature of the mills, the chip evacuation space of the flutes is also a curved surface, which makes the rake angle along the cutting edge vary. Therefore, it is necessary to propose a new mechanistic cutting force model with the capability to analyze arbitrary milling tool geometry.

2.3.2 Force Model of Worn Tool

Numerous researchers worked on the mechanistic force modeling. However, only few attempts have been made to simulate the cutting forces of worn cutting tool, even for orthogonal or oblique cutting. In order to develop such a model, it is necessary to have an understanding of the nature of tool flank contact. The plastic deformation of both the tool flank surface and the workpiece surface increases the difficulty and complexity of the model. Teitenberg et al. (1992) assumed the total forces on a worn tool were the summation of forces of the sharp tool and the forces due to the tool wear. Moreover, they assumed the same empirical equations can be applied to both the forces on the sharp tool and the forces caused by tool wear. Thus by conducting experiments with both sharp and worn tool, they subtracted the forces due to tool wear and found the coefficients in the empirical equations for their force model of worn tool.

DeVor and his coworkers also contributed to the modeling of cutting force of worn tool for orthogonal cutting processes. Waldorf et al. (1998) proposed a slip-line field model as a predictor of forces and used the ploughing characteristics to predict the stresses on the flank area of a worn tool. With their proposed combination of elastic contact and plastic flow on the wear area, two sets of equations for the flank stresses were summarized in Smithey et al.'s work (2000). The stresses were closely related to the flank wear, which was assumed to be known from the measurement during experiments. The other important topic studied by Smithey et al. (2001) was the definition of the plastic flow region. This region was determined from series of tool wear experiments, and it was assumed to be dependent on materials but independent on cutting conditions. Their model was applied in several further studies where cutting force of worn tool were considered important (Karpat and Özel, 2006, Li and Liang, 2007). However, these works only focused on simple turning process and have not been extended to milling process yet.

2.4 Limitations of the Existing Force Model

From the literature review, it is shown that the existing mechanistic force models can only be applied to a "well-defined" tool geometry, such as the classification and definition of tool geometry in Engin and Altintas works (2001). However, with the improvement of tool grinding technology, these models may not be applicable for newly designed tool shape and cutting edge geometry. In this study, the cutter geometry data is directly extracted from the CAD model of the milling tool. The extracted data includes not only the points on the cutting edge, but also the vectors which define the rake and flank surfaces on those points.

Another restriction on predicting cutting force of "well-defined" tool is because of the calculation of the uncut chip thickness, which is generally agreed to be one important parameter in the empirical equations of specific cutting force. It is also the parameter that defines the “chip load” and directly affects the elemental cutting force. In the literature and previous studies for milling process, the uncut chip thickness was always calculated approximately according to a sinusoidal function related to the cutting feed direction and magnitude. In this study, a universal uncut chip thickness calculation method has been proposed. Based on the definition of chip load in the cutting process and the uncut chip thickness direction defined in an oblique cutting model, the uncut chip thickness for each elemental cutting tool in the mechanistic model can be obtained.

The second part of this study is to estimate the cutting force of a worn milling tool. When a milling tool is new, the cutter geometry is assumed to be the same as the CAD design. However, when the tool starts to wear, the cutter geometry changes and so does the cutting force. The increasing cutting force not only causes larger loading on the tool but also leads to higher cutting temperature which will result in shorter tool life. In the study, the force model of worn tool in oblique cutting process from literature has been applied to milling. By comparing to the sharp tool, the effects of tool wear on the cyclic forces in the milling process can be observed and discussed.

2.5 Cutting Force Model of Sharp Tool

2.5.1 Basic Model Construction

The basic construction of a mechanistic model involves dividing the total cutting edges of a tool into a number of elemental cutting tools (ECTs), treating each element as though it is independently involved in oblique cutting. This concept has been widely accepted in the calculation of cutting force in milling process in the literature (DeVor et al., 1980, Kline et al., 1982, Yang and Park, 1991, Tai and Fu, 1994, 1995, Chiang et al., 1995). Next, an algorithm for relating orthogonal and oblique cutting geometry and process conditions to elementary cutting tool forces using experimental techniques is needed. DeVor and his coworkers (1980, 1982, 1984, 1993, 1995) have been working thoroughly in the mechanistic force modeling area for more than twenty years. In this study, the elemental force calculation is based on the methodology by Endres (1995).

Figure 2.1 shows the oblique cutting model for each ECT on the cutting edge of milling tool. Two coordinate systems have been shown, the rake-face system, which contains forces acting on the rake surface, and the ECT coordinate system. Cutting force occurs mainly at the tool-chip contact area, therefore the mechanistic model starts from calculating the forces on the rake surface. In the rake-face system, two force components are included. One of them is the friction force, which acts along the chip flow direction on the tool-chip interface (See Figure 2.1). The other is the normal force, which acts in the direction perpendicular to cutting edge on the cutting surface.

The friction and normal forces in the rake-face system can be calculated by equations (2.1) and (2.2).

$$\left|\overline{F}_n\right| = K_n A_c \tag{2.1}$$

$$\left|\overline{F}_f\right| = K_f A_c \tag{2.2}$$

The chip area A_c is defined as the surface of the chip normal to the direction of cutting velocity.

$$A_c = t_c \times L \times \cos\lambda \tag{2.3}$$

L is the length of ECT. λ is the oblique angle, which is defined as the angle between cutting edge and the direction perpendicular to cutting speed at the workpiece plane.

K_n and K_f are obtained by the empirical equations which consider uncut chip thickness, cutting speed and normal rake angle as the main factors.

$$\ln K_n = a_0 + a_1 \ln t_c + a_2 \ln V + a_3 \ln(1-\sin\alpha_n) + a_4 \ln t_c \ln V \tag{2.4}$$

$$\ln K_f = b_0 + b_1 \ln t_c + b_2 \ln V + b_3 \ln(1-\sin\alpha_n) + b_4 \ln t_c \ln V \tag{2.5}$$

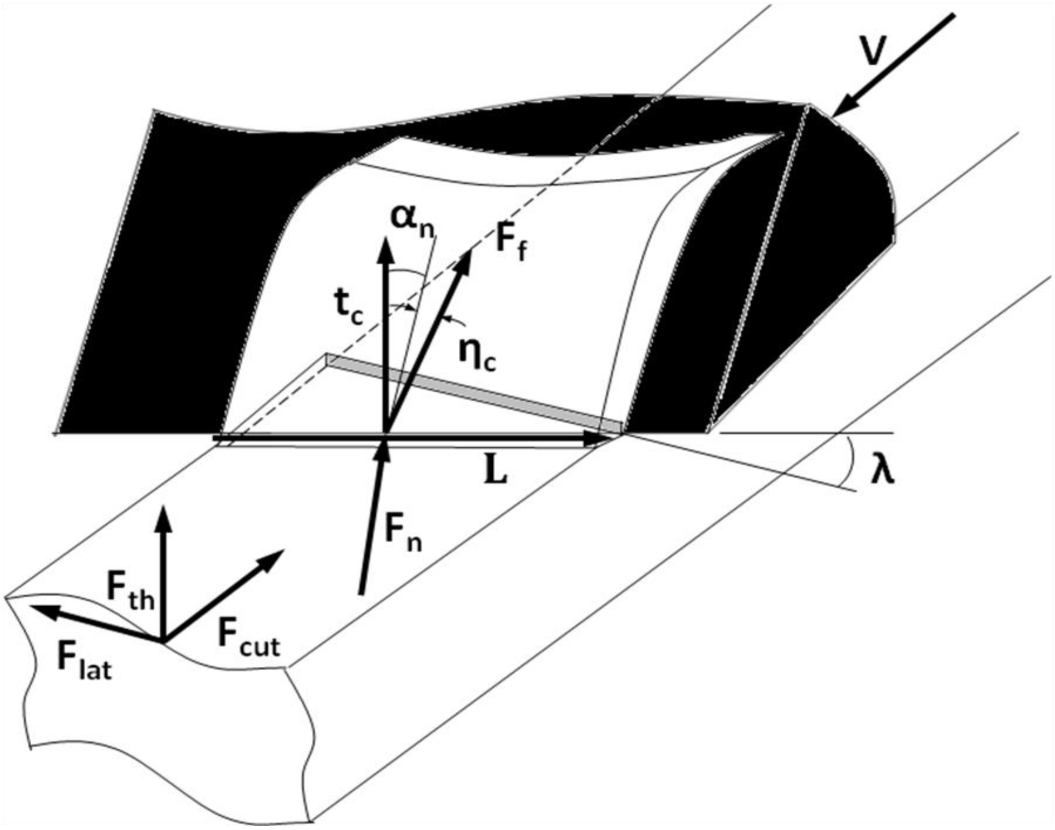

Figure 2.1: Oblique cutting model (Chandrasekharan, 1995)

$a_0, a_1, a_2, a_3, a_4, b_0, b_1, b_2, b_3, b_4$ are the coefficients, which are obtained from Meyer's work (2007). The calculation of all the parameters will be introduced later.

From all the above equations, the forces in the rake-surface system can be obtained. By coordinate transformation between the rake-surface and ECT coordinate system, the magnitude of three force components are calculated as the following equations.

$$\left|\overline{F}_{th}\right| = \left|\overline{F}_{f}\right| \cos\eta_c \cos\alpha_n - \left|\overline{F}_{n}\right| \sin\alpha_n \tag{2.6}$$

$$\left|\overline{F}_{cut}\right| = \left|\overline{F}_{f}\right| \left(\sin\eta_c \sin\lambda + \cos\eta_c \cos\lambda \sin\alpha_n\right) + \left|\overline{F}_{n}\right| \cos\lambda \cos\alpha_n \tag{2.7}$$

$$\left|\overline{F}_{lat}\right| = \left|\overline{F}_{f}\right| \left(\cos\eta_c \sin\lambda \sin\alpha_n - \sin\eta_c \cos\lambda\right) + \left|\overline{F}_{n}\right| \sin\lambda \cos\alpha_n \tag{2.8}$$

With the assumption of Stabler’s Rule, the chip flow angle η_c is equal to the oblique angle in the construction of cutting force model. Equations (2.9), (2.10) and (2.11) show the final expression of the three force components in the ECT coordinate system, the thrust force (F_{th}), the cutting force (F_c) and the lateral force (F_{lat}).

$$\left|\overline{F}_{th}\right| = \left|\overline{F}_{f}\right| \cos\lambda \cos\alpha_n - \left|\overline{F}_{n}\right| \sin\alpha_n \tag{2.9}$$

$$\left|\overline{F}_{cut}\right| = \left|\overline{F}_{f}\right| \left(\sin^2\lambda + \cos^2\lambda \sin\alpha_n\right) + \left|\overline{F}_{n}\right| \cos\lambda \cos\alpha_n \tag{2.10}$$

$$\left|\overline{F}_{lat}\right| = \left|\overline{F}_{f}\right| \left(\cos\lambda \sin\lambda \sin\alpha_n - \sin\lambda \cos\lambda\right) + \left|\overline{F}_{n}\right| \sin\lambda \cos\alpha_n \tag{2.11}$$

The definition of each force component is clearly illustrated in Figure 2.1. The cutting force is in the opposite direction of the cutting velocity, the thrust force is in the direction of the uncut chip thickness, and the lateral force is in the direction perpendicular to both the cutting velocity and the uncut chip thickness. According to the direction vectors of each force component, the elemental cutting forces in the milling tool coordinate system can be obtained by equation (2.12).

$$\vec{F}_i = \left|\overline{F}_{th}\right|\vec{t}_c - \left|\overline{F}_{cut}\right|\vec{V} + \left|\overline{F}_{cut}\right|\left(\vec{V} \times \vec{t}_c\right) \tag{2.12}$$

The vectors are all in the milling tool coordinate, and the calculation methods will be introduced in section 2.5.2. Each elemental cutting force $\vec{F}_i$ represents only the force on one individual ECT, which is a portion of the whole cutting edge. Therefore, the summation of the cutting forces on all the ECTs will give the total force on the cutter $\vec{F}$.

$$\vec{F} = \sum_{i=1}^{n} \vec{F}_i \tag{2.13}$$

2.5.2 Cutter Geometry Input and Parameters Calculation

The cutter geometry must be defined first as the input in the cutting force model. The necessary information includes the coordinate of the points on the cutting edges, and the corresponding rake and clearance angles at those points. In this study, the cutter geometry information is obtained directly from the tool CAD model, which is designed by Uni-Graphic(UG) software. The coordinate system of the CAD model, which is the same as the milling tool coordinate system, is defined as: x coordinate is the feed direction, z is the tool axis direction, and y is perpendicular to both x and z . All the calculations of point coordinate and vectors are defined according to this coordinate system.

UG software has a function which can divide a selected curve into numerous equal-length segments. The coordinate of those points which divid those segments can be read and recorded, as shown in Figure 2.2. The more points being extracted from the CAD model, the more precisely the model describes the cutter geometry. In the model, it is assumed that the nearby two points form an ECT, and the middle point on the ECT is assumed to be the point where all forces acted on.

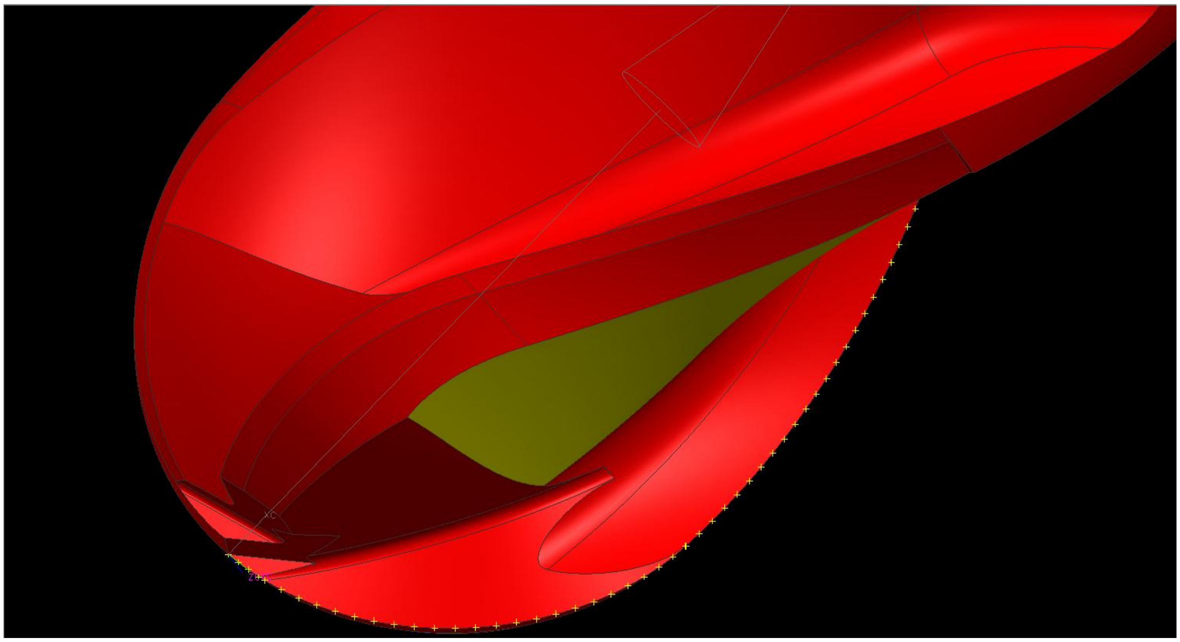

Figure 2.2: Data point extraction from CAD model

Some important vectors need to be calculated first based on the oblique cutting model, as shown in Figure 2.1. The cutting edge vector $\vec{L}$ is the position difference between the two points that form the ECT. The cutting velocity $\vec{V}$ includes not only the rotational motion of the tool but also the linear feed motion. The rotational speed is the cross product of the spindle speed and the radius of the rotating point, which is approximated by the radius of the middle point in the cutting edge.

$$\vec{V}_{rotate} = \omega\hat{k} \times \left(x_0\hat{i} + y_o\hat{j}\right) \tag{2.14}$$

$$\vec{V}_{feed} = f\hat{i} \tag{2.15}$$

$$\vec{V} = \vec{V}_{rotate} + \vec{V}_{feed} \tag{2.16}$$

The uncut chip thickness vector is normal to the machined surface. This means it will be perpendicular to both the cutting velocity vector $\vec{V}$ and the cutting edge vector $\vec{L}$. Therefore, it can be calculated by equation (2.17).

$$\vec{t}_c = \vec{V} \times \vec{L} \tag{2.17}$$

The rake and clearance angles cannot be directly extracted from the CAD model; however, a useful function can be utilized. The function has the capability to extract the normal vector from a selected point on a surface, which means, the normal vectors of the rake surface $\vec{S}_{rn}$ and the normal vector of the clearance surface $\vec{S}_{rn}$ on a point on the cutting edge can be obtained.

The rake angle is defined by the angle between the vector parallel to the rake surface and the vector normal to the machined surface, which is $\vec{t}_c$. The vector parallel to the rake surface $\vec{S}_{rp}$ is perpendicular to both the cutting edge $\vec{L}$ and the normal vector of the rake surface $\vec{S}_{rn}$.

$$\vec{S}_{rp} = \vec{L} \times \vec{S}_{rn} \tag{2.18}$$

Therefore the rake angle can be obtained.

$$\alpha_n = \cos\left(\frac{\vec{t}_c \cdot \vec{S}_{rp}}{\left|\vec{t}_c\right|\left|\vec{S}_{rp}\right|}\right) \tag{2.19}$$

Similarly, the vector parallel to the clearance surface ($\vec{S}_{cp}$) can be obtained by the cross product between the cutting edge $\vec{L}$ and the normal vector of the clearance surface $\vec{S}_{cn}$.

$$\vec{S}_{cp} = \vec{L} \times \vec{S}_{cn} \tag{2.20}$$

The clearance angle θ is the angle between the vector parallel to the clearance surface and the cutting velocity direction.

$$\theta = \cos\left(\frac{-\vec{V} \cdot \vec{S}_{cp}}{|\vec{V}||\vec{S}_{cp}|} \right) \tag{2.21}$$

2.5.3 Universal Chip Thickness Calculation

In this study, a method is proposed to calculate the uncut chip thickness for arbitrary cutter geometry. In the literature and previous researches, it is calculated approximately according to a sinusoidal function related to the cutting feed direction and magnitude (DeVor et al., 1982, Yang and Park, 1991, Yűcesan and Altintas, 1996). This approximation is good enough for a “real ball shape” mill. However, it cannot reliably estimate the uncut chip thickness with arbitrary shape of mills, which are becoming more popular in industry now.

The chip is the part of the workpiece being removed when the cutter moves from one position to the second position, as shown in Figure 2.3.

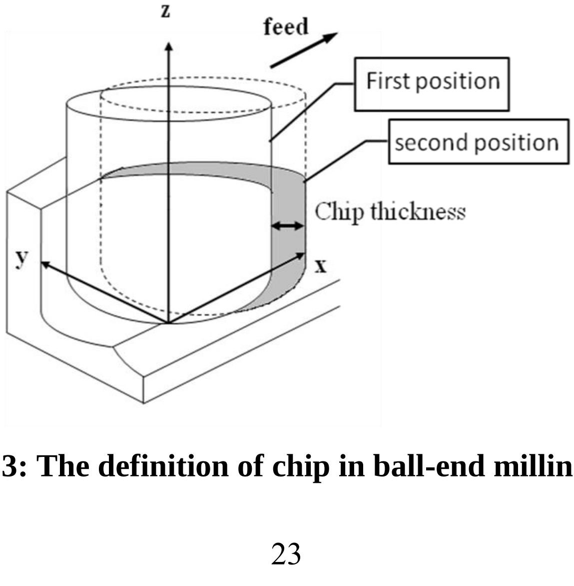

Figure 2.3: The definition of chip in ball-end milling process

In most machining processes, feed or feed rate is the parameter which defines the tool movement. The uncut chip thickness is the thickness of the chip in the direction of $\vec{t}_c$ from the oblique cutting model as shown in Figure 2.1. This vector starts from the middle point of each ECT, and encounters with the boundary the tool previously cut. The distance between the starting point and the intersecting point is determined to be the chip load. The start point is the midpoint of the ECT with three components (x_0, y_0, z_0). The encountered point is the solution between a line (the uncut chip thickness vector) and a surface (the cut boundary). The cut boundary is formed by the ECTs, thus this methodology can be applied to arbitrary tools.

The uncut chip thickness vector can be represented with three components (t_{cx}, t_{cy}, t_{cz}). The line equation in three-dimension with known direction (t_{cx}, t_{cy}, t_{cz}) and passing through point (x_0, y_0, z_0) is shown in equation (2.22).

$$\frac{(x-x_0)}{t_{cx}} = \frac{(y-y_0)}{t_{cy}} = \frac{(z-z_0)}{t_{cz}} \tag{2.22}$$

Once the line equation that represents the uncut chip thickness direction is obtained, the next step is to build the surface equation which describes the boundary the tool cuts. The cutting edge of the tool is divided into ECTs and each ECT has been viewed as a linear segment in the model. Instead of the perfect "tool shape," the cutting edge of the tool now is viewed as a connection of numerous linear pieces. Each piece moves in its cutting direction and forms its cut boundary. The total tool boundary is the connection of the boundary formed by individual segments.

In the milling process, the tool rotates about the spindle axis and moves linearly in the feed direction at the same time. The tool repeats the same movement in each revolution and thus one revolution can be treated as one cutting cycle. Therefore, for each revolution, the chip is defined aas the material in between where the ball-end mill is and the boundary the tool cut before one full revolution. If each ECT rotates about the cutter axis for a whole revolution, it will form the cutter boundary envelope in the shape of a truncated cone. Thus, the whole cutting tool boundary is formed by a series of connecting truncated cones, as shown in Figure 2.4.

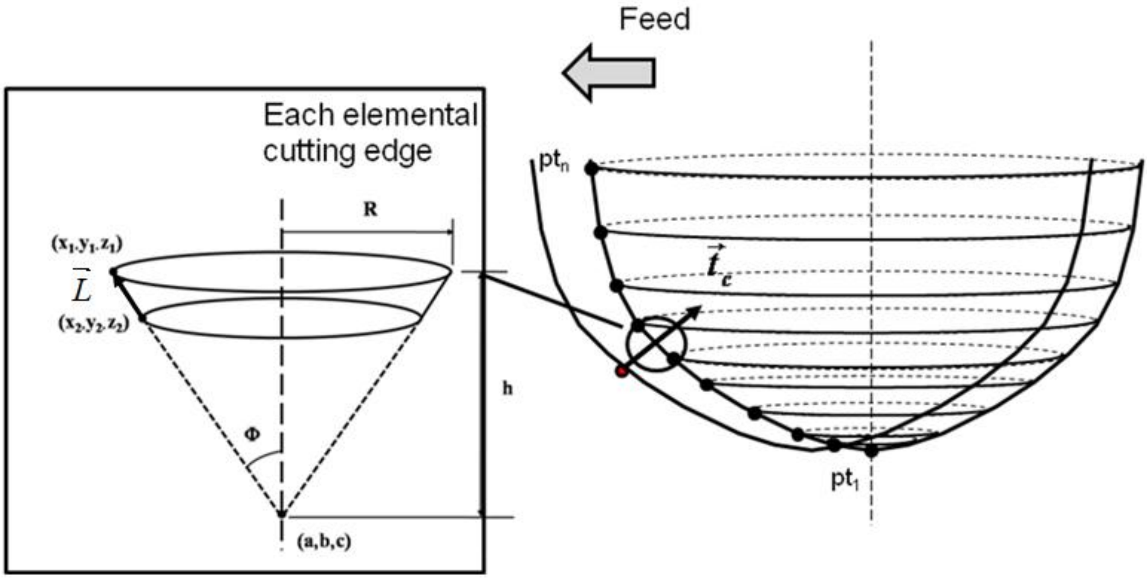

Figure 2.4: Ball-end mill boundary formed by series of truncated cones

From Figure 2.4, the parameters for each truncated cone can be obtained from the cutting edge vector $\vec{L}$, and the coordinate of the end points of the ECT, (x_1, y_1, z_1) and (x_2, y_2, z_2). The parameters of truncated cone, including the angle of the cone ϕ, the larger radius of the truncated cone R, the height of the truncated cone h, and the location of the cone tip (a,b,c), can be calculated by the following equations.

$$\sin\phi = \frac{\vec{L}\cdot\vec{Z}}{|\vec{L}||\vec{Z}|} \tag{2.23}$$

$$R = \sqrt{\left(x_1^{\ 2} + y_1^{\ 2}\right)} \tag{2.24}$$

$$h = \frac{R}{\tan\phi} \tag{2.25}$$

$$(a,b,c) = \left(-\frac{f}{N_{teeth}}, 0, z_1 - h\right) \tag{2.26}$$

$\vec{Z} = (0,0,1)$ is the vector that represents the cone axis. The equation describing the surface of the truncated cone is defined in equation (2.27).

$$((z-c)\tan\phi)^2 = (x-a)^2 + (y-b)^2, \quad z_2 < z-c < z_1 \tag{2.27}$$

The solution of the uncut chip thickness direction line, equation (2.22), and the connecting truncated cone boundary, equation (2.27), is the intersection point, presented as (x_0', y_0', z_0'). Thus, the uncut chip thickness is calculated as

$$t_c = \sqrt{(x_0'-x_0)^2 + (y_0'-y_0)^2 + (z_0'-z_0)^2} \tag{2.28}$$

All the parameters and the methods to obtain them are introduced in section 2.5.2 and 2.5.3. After calculating all the parameters, substitute them into the force calculation in 2.5.1, then the total force on the sharp ball-end mill can be estimated.

2.6 Application of Uncut Chip Thickness Calculation in Face Turning Process

The developed mechanistic force model is expected to be applicable for arbitrary cutter geometry. In this section, the model is applied to the face turning process with the use of a round insert with fixed rake and clearance angles, as shown in Figure 2.5(a). The engagement region of the inserts is defined by the axial depth of cut and feed rate of the turning process.

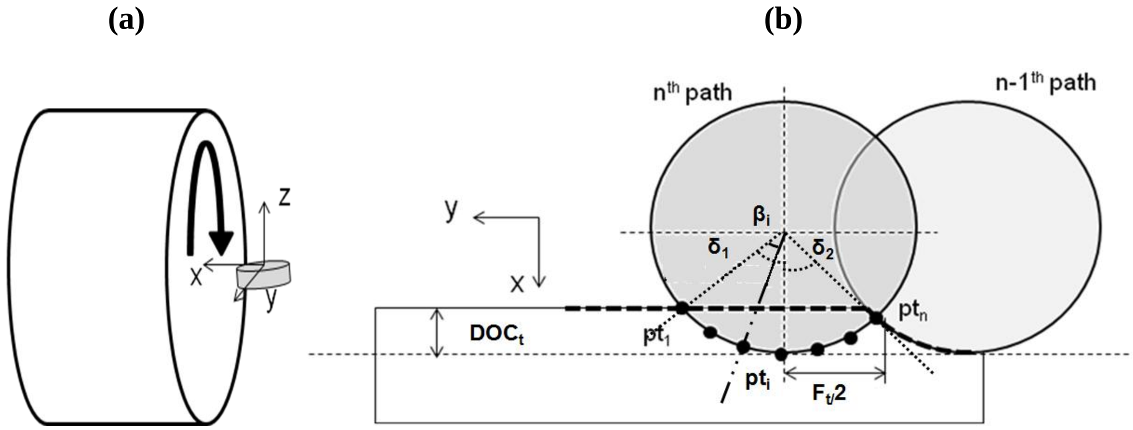

Figure 2.5: (a) Face turning using round insert (b) Illustration of the engagement region and points on the cutting edge

According to Figure 2.5, the engagement angles are calculated by equations (2.29) and (2.30).

$$\delta_1 = \cos^{-1}\left(\frac{R_t - DOC_t \sin\alpha_t}{R_t}\right) \tag{2.29}$$

$$\delta_2 = \sin^{-1}\left(\frac{f_t/2}{R_{tool}}\right) \tag{2.30}$$

Same as in milling process, the total cutting edge is divided into a number of ECTs, treating each element as independently involved in oblique cutting. The coordinates of the points of each ECT are obtained from the geometry of the round insert.

$$pt_i(x, y, z) = (R_t \cos\beta_i \cos|\alpha_t|, R_t \sin\beta_i, R_t \cos\beta_i \sin|\alpha_t|) \tag{2.31}$$

All parameters can be calculated from the coordinate of points as explained in section 2.5.2. However, the boundary the tool previously cut in the turning process is different from that in milling. In the face turning process, the tool is moving in the feed direction, which is the y direction in Figure 2.5(a), and the workpiece is rotating about x axis at the same time. The cutting motion of the tool mainly comes from the rotation of the workpiece. In this case, the boundary should be the surface of the workpiece. However, from Figure 2.6(a), it is shown that the tool leaves a cut boundary before it moves a distance of feed in the y direction. So in the face turning process, the boundary is formed by the combination of the original workpiece surface (the straight part of dash line) and previous path of the inserts (the circular part of the dash line).

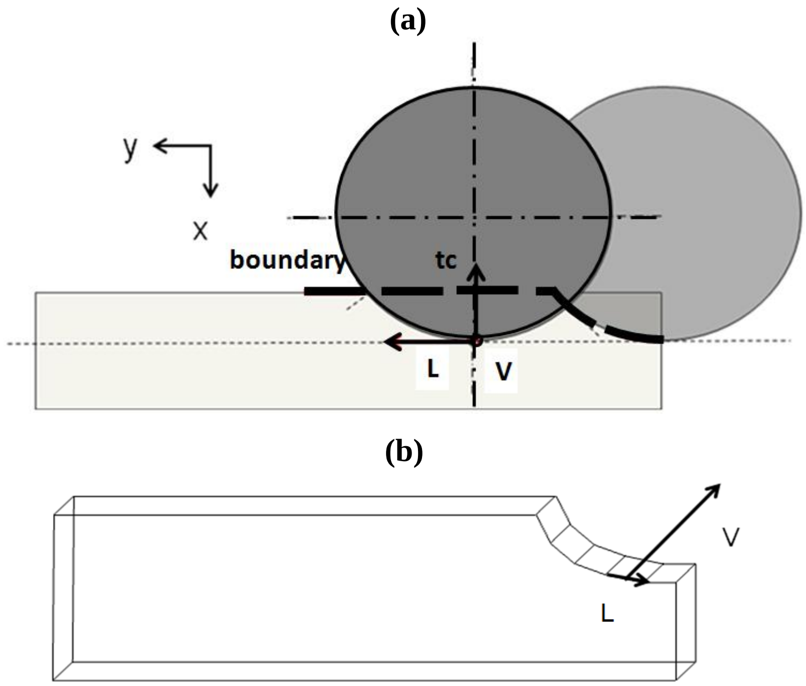

Figure 2.6: (a) Illustration of cutter boundary (b) The formation of cutter boundary

The original workpiece surface is easily described with a normal vector $(1,0,0)$ and a point which is on that surface (pt_1 in Figure 2.5(b)). The previous path of the insert can be viewed as each ECT swipes along the cutting velocity direction and forms a flat surface. The boundary formed by previous cut path can be viewed as the combination of all the swiping surfaces by the ECT. The swiping surfaces can be seen more clearly in Figure 2.6 (b).

The swiping surface has normal vector $\vec{N}$, which can be obtained from cutting edge vector $\vec{L}$ and cutting velocity vector $\vec{V}$.

$$\vec{N} = \vec{L} \times \vec{V} \tag{2.32}$$

The three components of the normal vector are $\vec{N} = (N_1, N_2, N_3)$. The middle point of the ECT (x_0, y_0, z_0) is on the swiping surface. The equation of a flat surface with normal vector, and a point on it can be written as:

$$N_1 x + N_2 y + N_3 z = N_1 x_0 + N_2 y_0 + N_3 z_0 . \tag{2.33}$$

The uncut chip thickness direction line can be obtained from equation (2.22). By solving equations (2.22) and (2.33), the intersection point can be found. Finally, the uncut chip thickness can be calculated with the use of equation (2.28).

2.7 Cutting Force Model of Worn Tools

In the sharp tool, the forces mainly come from the chip formation at the cutting edge and the tool-chip contact on the rake surface. However, after the tool starts to wear during the machining process, the flank surface of the tool begins to contact with the machined surface due to the appearance of flank wear. The contact between the flank wear area and the machined surface results in extra friction and normal forces on the flank wear region of the tool. Therefore, the total cutting force in the machining process keeps increasing with the growing tool wear, which is positively correlated to the machining time.

First, the cutting edge is divided into numerous ECT in the mechanistic force model of the worn tool. Each ECT is considered as an individual oblique cutting unit. The normal and friction forces on the flank wear surface on each ECT are calculated based on

Smithey et al.'s work (2000, 2001). They assumed a stress distribution on the tool flank by using slip-line theory around the cutting edge, as shown in Figure 2.7.

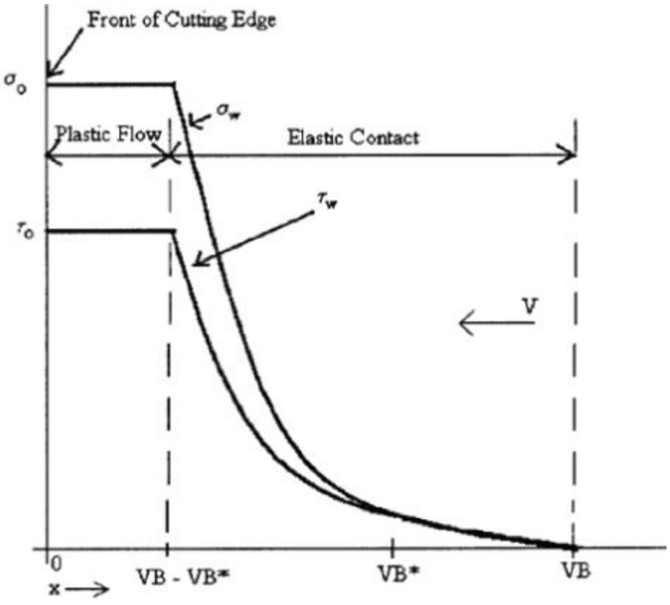

Figure 2.7 Flank stress distribution (Smithy et al., 2000)

σ_0 and τ_0 are the normal and shear stresses at the tool tip, which can be calculated using slip-line field (Smithey, 2000). σ_w is represented as a second order polynomial function related to flank wear *VB* and σ_0. Normal stress σ_w multiplied friction coefficient μ would be the shear stress τ_w. The friction coefficient μ between the workpiece and the tool is the same as the one between the rake surface and the chip since they are the same materials and lubrication in the cutting process. Thus, it is calculated by the friction and normal forces obtained from the sharp tool.

$$\mu = \frac{F_f}{F_n} \tag{2.34}$$

$VB*$ is the critical wearland where plastic flow is initiated. The critical wearland is obtained from the experimental observation following the study of Smithey et al. (2000).

The forces on the flank wear surface are then obtained by integrating the stresses over the flank wear width. The main equations of the normal force and the friction force on the flank wear area (F_{tw} and F_{cw}) are listed as the following.

$$F_{tw} = L\int_{0}^{VB} \sigma_0 \frac{VB - x^2}{VB} dx \quad , \tag{2.35}$$

$$F_{fw} = L \int_{0}^{VB(1-\sqrt{\frac{\tau_0}{\sigma_0}})} \tau_0 dx + L \int_{VB(1-\sqrt{\frac{\tau_0}{\sigma_0}})}^{VB} \mu\sigma_0 \frac{VB - x^2}{VB} dx , \quad \text{if } VB < VB*, \tag{2.36}$$

$$\text{and } F_{tw} = L \int_{0}^{VB-VB*} \sigma_0 dx + L \int_{VB-VB*}^{VB} \sigma_0 \left(\frac{VB - x^2}{VB*} \right)^2 dx , \tag{2.37}$$

$$F_{fw} = L \int_{0}^{VB(1-\sqrt{\frac{\tau_0}{\sigma_0}})} \tau_0 dx + L \int_{VB(1-\sqrt{\frac{\tau_0}{\sigma_0}})}^{VB} \mu\sigma_0 \left(\frac{VB - x^2}{VB*} \right)^2 dx , \quad \text{if } VB > VB*. \tag{2.38}$$

The normal force on the flank wear area F_{tw}, integrated by the normal stress, acts in the same direction of the thrust force, which is in the chip thickness direction. The cutting force on the flank wear area F_{cw}, integrated by the shear stress, acts in the same direction of the cutting force, which is in the cutting velocity direction. Therefore, the total force on the worn tool of each ECT can be shown as a vector form in equation (2.39).

$$d\vec{F}_w = \left|\bar{F}_{th} + \bar{F}_{tw}\right|\vec{t}_c - \left|\bar{F}_{cut} + \bar{F}_{cw}\right|\vec{V} + \left|\bar{F}_{lat}\right|\left(\vec{V} \times \vec{t}_c\right) \tag{2.39}$$

Finally, the total force of the worn tool is the summation of all elemental cutting forces.

2.8 Experimental Validation

2.8.1 Force Validation for Sharp Tool

2.8.1.1 Slot Milling with Ball-end Mill

A series of validation experiments were conducted to verify the constructed cutting force model. The validation tests were conducted on a FADAL (1998 VNC 3016L) three-axis CNC machining center. The workpiece was mounted on a dynamometer (Kistler 9257A), which was used to measure the cutting force. The voltage signal from the charge amplifier was fed to an analog to digital converter card, and recorded in the computer. The voltage signals were then multiplied to the appropriate scale factor for each channel to obtain the experimental force data. A sampling rate of 3600 Hz was used in the data collection in order to collect enough data points of the forces in high spindle speed tests.

In the validation experiments, the ball-end mill had four teeth. The cutter geometry data, including the point coordinate, rake surface vector and flank surface vector were all directly extracted from the CAD model of the used tool. One special design of the tool was that only two of the flutes went all the way to the ball-end mill tip, the long flutes, and the other two flutes only went to a certain distance from the tip, the short flutes. The tool material was tungsten carbide with 10% cobalt, and a small amount of VC and Cr_3C_2 as grain growth inhibitors. The workpiece material was Ti-5Al-2Sn-2Zr-4Cr-Mo alloy, also called Ti17 in industry. Two sets of validation experiments have been conducted.

The experimental parameters are shown in Table 2.1. For each test condition, three experiments have been done to verify the repeatability under the same cutting condition.

Table 2.1: Validation experimental conditions

Test condition number	Spindle speed (rpm)	Feed (m/min)	Axial depth of cut (mm)
1	583	0.114	1
2	3500	0.64	2.54

The experimental results and modeling results are shown in Figure 2.8. For all the forces, the solid lines represent the experimental results, and the dashed lines are the modeling results. Comparing the modeling results with the experimental results in Figure 2.8, we can see that the constructed force model can predict F_x and F_y well. In the first test, the depth of cut is very small and only a small portion of the short flutes engage in cutting. However, in the second test, the larger depth of cut makes the two short flutes engage in cutting more. The small peaks in between the maximum peak and valley of the forces indicate the engagement of short flutes. The good agreement of the position of the small peaks suggests that the model can capture the existence of the short flutes very well.

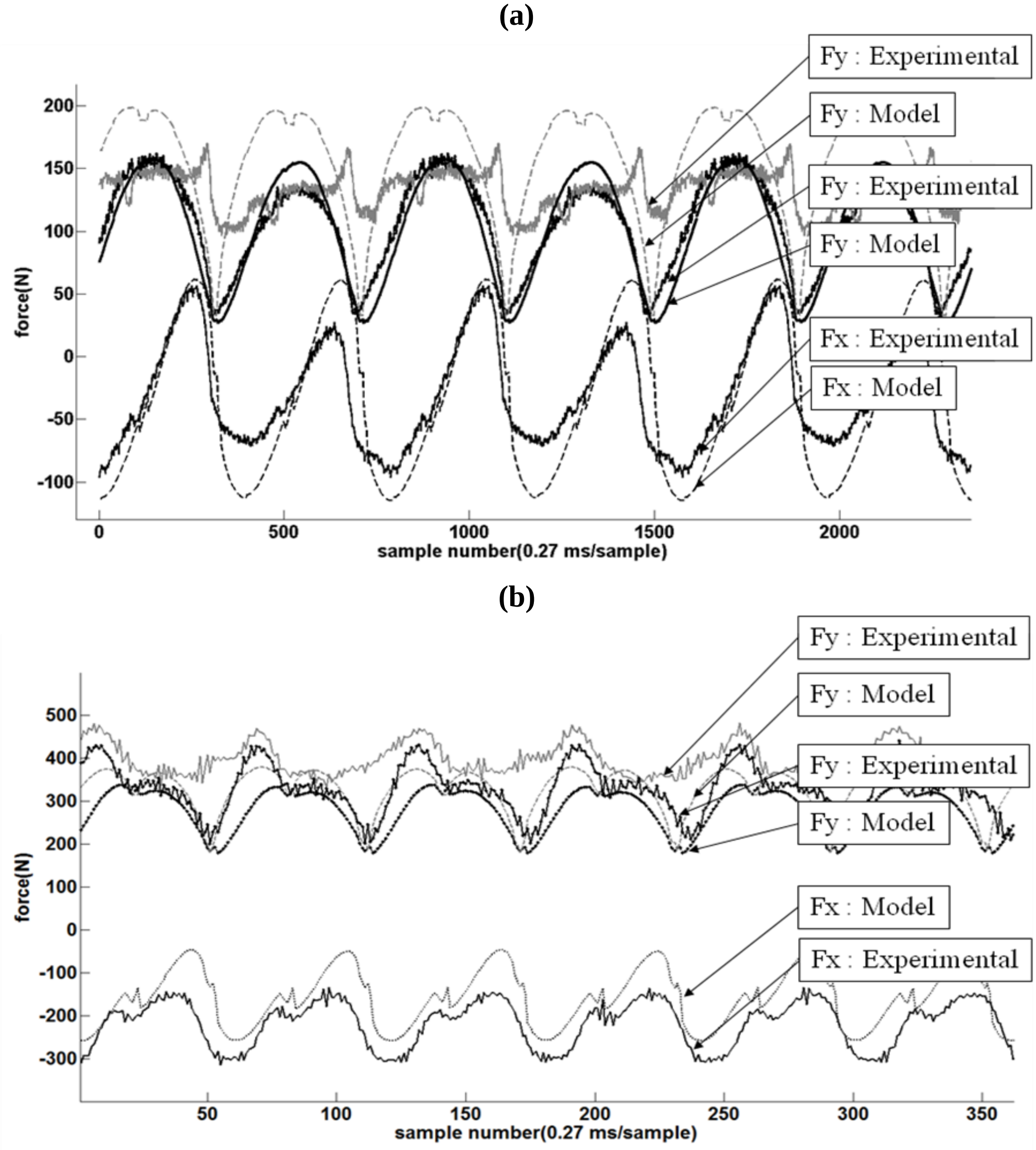

Figure 2.8: Force validation in slot milling (a) 1st test (b) 2nd test

As for F_z, it is clearly seen that the average value of the force is similar between the modeling results and the experimental results. However, the results do not show as good agreement as x and y forces. The experimental results have higher fluctuation magnitude than modeling results, and the position of peak values don't match up with modeling results. There are two possible reasons that result in the difference between experimental and simulation results. First, the CAD model does not represent the real tool well at the cutter tip area. Thus, using the CAD model for the simulation may result in some errors when predicting F_z. Second, the force model does not consider the tool deflection, run-out, or vibration, which may cause the fluctuations in F_z. However, under the assumptions of ideal cutting conditions, the validation experiments still show that the constructed mechanistic force model can predict the forces well.

In previous studies for milling process, the force model used constant rake and clearance angle along the whole flute and sinusoidal function to approximate chip load (DeVor et al., 1982, Yang and Park, 1991, Yűcesan and Altintas, 1996). In order to show the improvement of the proposed model, the modeling results and the forces using the constant angles and sinusoidal function chip load under the cutting condition of the 2nd test are plotted in Figure 2.9. The same tool geometry and same mechanistic force equations were used but the CAD model extracted rake angles were replaced with a constant rake angle. Also, the uncut chip thickness is calculated based on the sinusoidal function related to the cutting feed direction and magnitude.

$$t_c = f \sin\varphi \sin\kappa . \tag{2.40}$$

f is the feed per tooth, φ is the radial angle, and κ is the axial immersion angle. It is clearly seen in Figure 2.9 that the proposed model shows better result than the literature method. The minimum F_x, F_y and F_z in one tool revolution from both the proposed model and the literature method have similar value. However, the maximum value of the forces in the proposed model show significantly better agreement with the experimental result. Overall, the proposed model has an average of 19.6% error while the literature method has about 27.2% error comparing to the experimental forces. Therefore, the proposed model has improved result with the use of more accurate rake angle and uncut chip thickness calculation method.

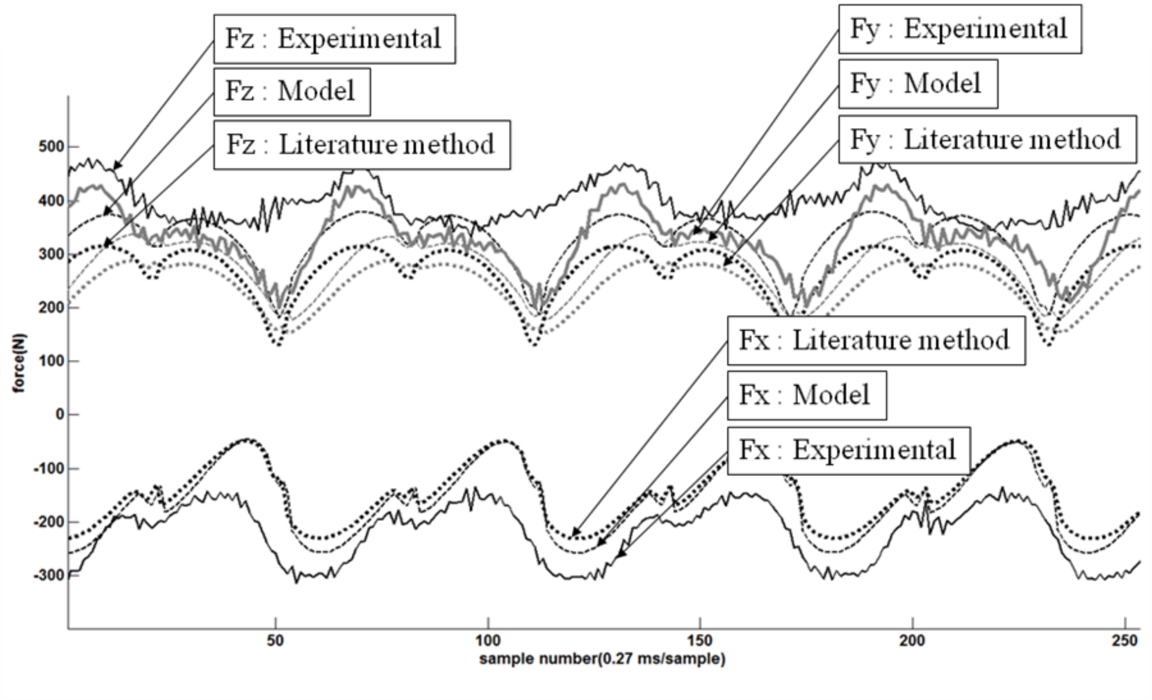

Figure 2.9: Comparison with the literature method using constant angles and sinusoidal function chip load

2.8.1.2 Face Turning with Round Inserts

A series of additional validation experiments have been conducted to verify the constructed cutting force model for arbitrary cutter geometry on a Lodge & Shipley lathe. The data collection setup, as well as the workpiece material, was the same as the milling validation experiments. Round tungsten carbide inserts manufactured by Kendex (RNG43K68) were used in turning. Although the main material of the round inserts were tungsten carbide, the same as the milling tool, the cobalt percentage of the turning inserts was only 6%, lower than that of the milling tool. This is because the turning inserts required higher hardness while the milling tools need higher toughness for interrupted cutting. The force model coefficients were calibrated using 10% cobalt tungsten carbide tool because the study focuses on milling process. This might cause some discrepancy between the turning experimental results and the modeling results.

Eight sets of validation experiments have been conducted, each repeated twice. The experimental parameters are shown in Table 2.2, based on the suggested turning condition for this tool-workpiece combination in industry.

Table 2.2: Validation experimental conditions for turning

Test condition number	Feed rate (mm/rev)	Cutting Speed (SFM)	Depth of cut (mm)
1	0.127	250	0.127
2	0.127	350	0.127
3	0.381	350	0.127
4	0.381	250	0.127
5	0.381	250	0.381
6	0.381	350	0.381
7	0.127	350	0.381
8	0.127	250	0.381

The experimental results and modeling results are shown in Figure 2.10. The tests with different feed rate but same cutting speed and depth of cut are put together for comparison. The solid lines are the experimental results and the dash lines are the modeling results. The triangular markers represent F_x, the thrust force, and the square markers represent F_z, the cutting force. The corresponding coordinates are shown in Figure 2.5(a).

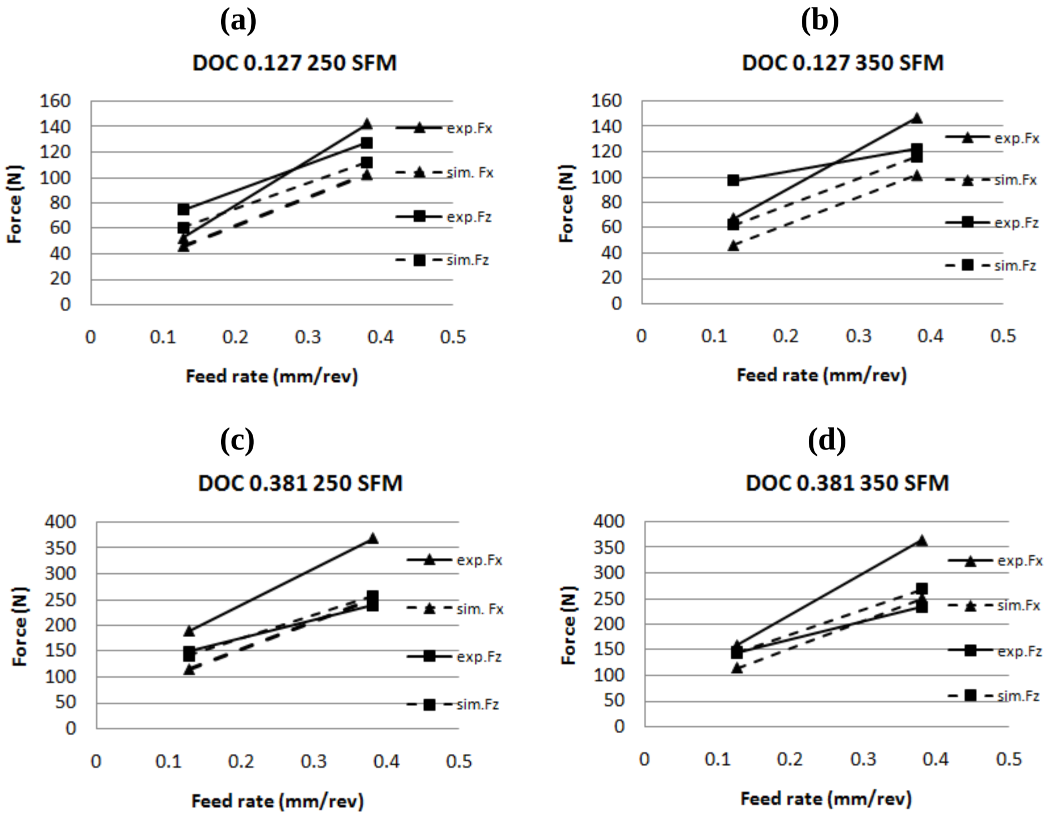
(a) (b) (c) (d)

Figure 2.10: Turning force validation (a) 1st and 4th test (b) 2nd and 3rd test (c) 5th and 8th test (d) 6th and 7th test

We see from Figure 2.10 that the modeling results agree with experimental results very well. Generally, the model can precisely predict F_z, while it has some errors in predicting F_x. The errors might be caused by the un-modeled effects such as vibration. Also, the uncut chip thickness in the turning tests is larger than that in milling. For tests number 5 to 8 (with larger depth of cut), the uncut chip thickness value is out of the range of the force coefficient calibration tests. This is very likely to cause inaccuracy of the modeling results. Also, the turning inserts material is slightly different from the tool material used in the force coefficient calibration tests, which might also cause the discrepancy between experimental and the modeling results.

2.8.2 Force Validation for Worn Tool

The validation experiments for worn tool were conducted with the same setup as the tests for sharp tool. To validate the forces of the worn tool, a new tool was used to repeat cutting full slots of 14.2 cm in length. The forces during the whole cutting process were recorded, and the flank wear was measured as input to the model after every 10 slots of cut. Two different cutting conditions were tested and the results are discussed as follows.

The first experiment was done under the cutting condition with 3000 rpm spindle speed, 1.27 m/min feed rate and 1.27 mm depth of cut. Figure 2.11 shows the cutting forces of experimental and modeling results after the tool has 0.07, 0.1 and 0.13mm flank wear. The general trend of F_x and F_y can be captured very well by the model. The F_x has very good agreement between the experimental and modeling results, in which the maximum force increases from 300 Newton to 400 Newton. F_y has about 100 Newton difference between the experimental and modeling results. However, the increasing range of the forces and the overlapping of peaks and valley position suggest that the model works well. Since F_z in the sharp tool does not show convincing agreement, it is expected that there is more discrepancy in F_z than F_x and F_y. However, except for Figure 2.11(a) in which the experimental F_z is significantly smaller than the modeling results, all the other figures show good agreement of the average forces that increases from 400 Newton to 600 Newton after the tool has 0.13mm flank wear.

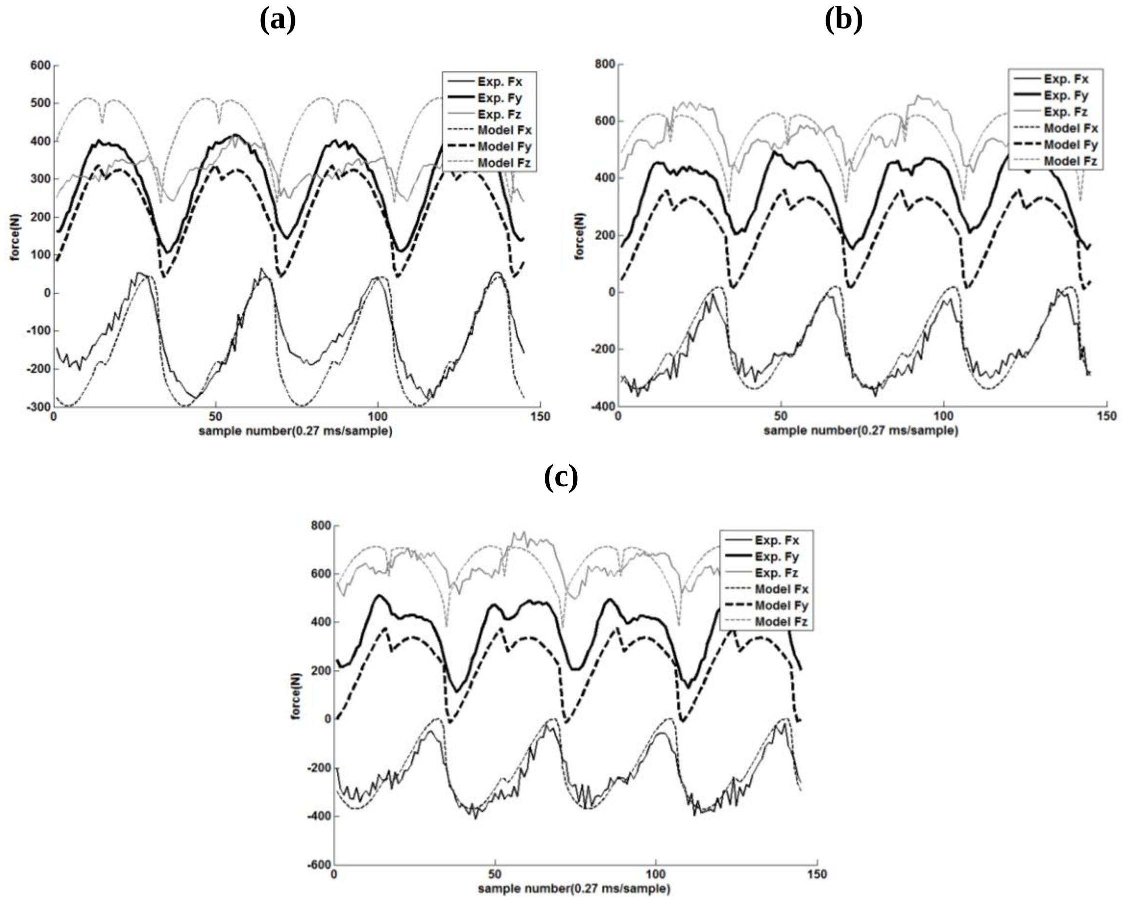

Figure 2.11: The forces when the tool has (a) 0.07mm (b) 0.1mm (c) 0.13mm flank wear spindle speed 3000 rpm, feed rate 1.25 m/min, depth of cut 1.52 mm

Figure 2.12 shows the results of cutting condition with spindle speed 3500 rpm, feed rate 0.64 m/min and depth of cut 2.54 mm. Conclusions similar to Figure 2.11 can be drawn. A little more discrepancy can be observed from Figure 2.12. This might be due to the larger depth of cut, which is very likely to cause tool vibration and tool run-out. In general, the modeling results agree with the experimental results very well.

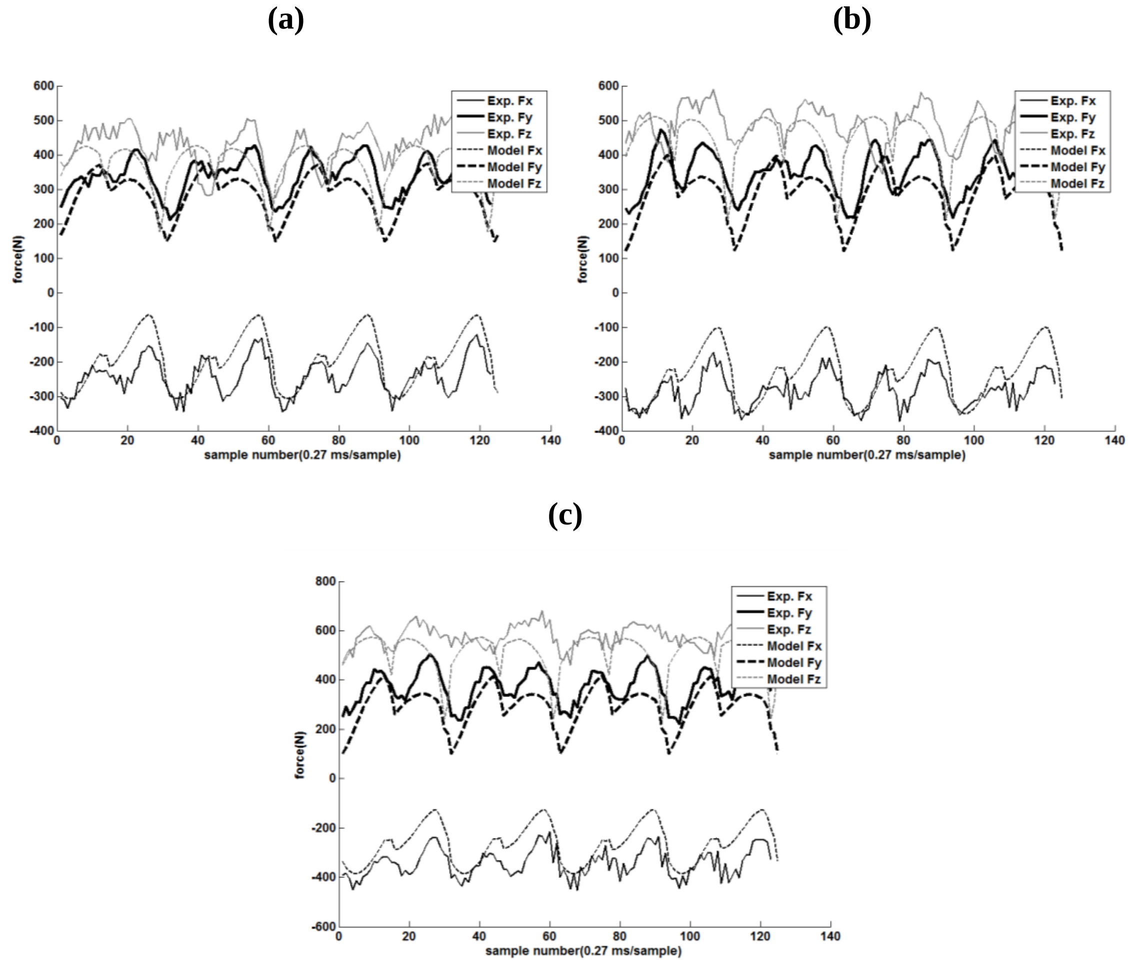

Figure 2.12: The forces when the tool has (a) 0.08mm (b) 0.13 mm (c) 0.18 mm flank wear spindle speed 3500 rpm, feed rate 0.64 m/min, depth of cut 2.54 mm

2.9 Conclusions

In this study, a cutting force model for arbitrary cutter geometry of sharp tool is proposed first. The model considers the varying rake and clearance angles along the flute area curve, and uses the universal chip thickness calculation method to extend the existing mechanistic force model for arbitrary cutter geometry. The model has been validated in both milling and turning processes. Moreover, the modeling result is compared with the literature method and shows convincing improvement. In the second part of the study, the forces due to flank wear are added to the forces of sharp tool for estimating those of the worn tool. The cyclic forces of the worn tool have been validated by ball-end milling experiments. Both the increasing magnitude and the changing shape of the waves of the forces under different wear levels show good agreement between the experimental and modeling results. In conclusion, an integrated model which can estimate the cutting forces of both new and worn tool of arbitrary cutter geometry in the machining processes is proposed and validated in this study.

CHAPTER 3

ESTIMATION OF MILLING TOOL TEMPERATURE

3.1 Nomenclature

b	width of cut
c_c	specific heat capacity of coolant
c_t	specific heat capacity of tool material
c_w	specific heat capacity of workpiece material
D	nozzle diameter
F_{cw}	component of force in cutting direction on flank surface due to tool wear
F_f	friction force on the rake surface on ECT
F_s	component of force parallel to shear plane on ECT
h_f	heat transfer coefficient on flank surface
h_r	heat transfer coefficient on rake surface
J	mechanical equivalent of heat
k_c	heat conductivity of coolant
k_t	heat conductivity of tool material
k_w	heat conductivity of workpiece material

L_f	Length of flank surface
L_{nozzle}	Distance of nozzle head from the tip of milling tool
l_c	tool-chip contact length
Nu_f	Nusselt number of the heat convection on flank surface
Nu_r	Nusselt number of the heat convection on rake surface
$\Pr_c$	Prandtle number of coolant
q''_{ff}	rate of heat generation by friction per unit area on the tool-workpiece contact surface
q''_{flank}	rate of heat flows into tool from flank surface per unit area
q''_{rake}	rate of heat flows into tool from rake surface per unit area
q''_{rf}	rate of heat generation by friction per unit area on the tool-chip contact surface
Re_f	Reynold number of the heat convection on flank surface
Re_r	Reynold number of the heat convection on rake surface
R_1	fraction of heat generated on shear plane that is conducted to chip
R_{fw}	fraction of heat generated due to friction on flank surface that is conducted to workpiece
T_c	coolant temperature
ΔT_s	average temperature rise on shear plane
t	time
t_c	uncut chip thickness

U_j	speed of coolant flow
V	cutting velocity
VB	flank wear width
V_{chip}	chip velocity
V_s	relative velocity between chip and workpiece on shear plane
γ	strain of chip
η_{nozzle}	angle between the nozzle axis and the tool axis
θ_0	room temperature
κ_t	thermal diffusivity of tool material
μ_c	viscosity of coolant
ρ_t	density of tool material
ρ_c	density of coolant

3.2 Introduction

Cutting temperature is an important parameter in metal cutting processes, especially when machining titanium alloys. Titanium alloys are well-known for their high strength; therefore, high energy is needed to shear the material during the chip formation process. Thus, a large amount of heat is generated. Moreover, titanium alloys have very low thermal conductivity. Unlike in other machining cases where a major portion of the generated heat dissipates with the chip, a significant amount of heat flows into the tool in machining titanium. The high temperature in the tool not only degrades the tool strength but also activates wear mechanisms. For WC-Co tools, temperature is especially a big factor which influences tool performance because Co is sensitive to rising temperature and the mechanical behavior of WC-Co is highly controlled by the properties of the cobalt binder (Mani and Gonseth, 1993, Acchar et.al, 1999).

In addition to the material degradation caused by high temperature, in the milling process, the temperature change during the cut and uncut cycle is another important issue. In the half revolution where the milling tool is engaged in cutting, the temperature rises due to the heat generation. In the non-cut half revolution, the milling tool is exposed to either air or coolant under room temperature. The high temperature difference between the tool and environment forces heat convection at the surface of the tool and results in a sudden cooling process in the tool. The temperature rising and decreasing result in excessive thermal stress in the tool and are responsible for the damages due to cyclic loading.

In this chapter, the modeling of milling tool temperature is discussed. A brief literature review shows the state-of-the-art of the temperature modeling technique and the remaining problems when applying to milling process. Based upon the existing model, some new ideas for improving temperature modeling have been proposed. Finally, a temperature measurement technique has been designed for validation of the proposed model.

3.3 Literature Review

3.3.1 Milling Temperature Models

High temperature during machining degrades the tool strength and activates wear mechanisms, thus influencing tool life dramatically. Early researches investigated the heat generation zones in machining processes. The generated heat is conducted to the chip, workpiece and tool, so the fraction of heat flowing to each of them also became another important topic. Analytical models of the temperature distribution in the tool, workpiece and chip have been developed based on various assumptions. Several literatures reviewed all these studies and summarized the assumptions and limitations of each model (Da Silva and Wallbbank, 1999, Komanduri and Hou, 2000, Adukhshim, et al., 2006). Most of these models assumed a steady-state cutting condition, which means that these models can only be applied to cutting processes with constant heat flux.

Milling is a discontinuous machining process and the milling tool experiences both loading-unloading and heating-cooling cycles during cutting. Therefore, in addition to the elevated cutting temperature, the heating and cooling cycles in the milling processes cause severe thermal stresses in the tool. Moreover, the chip load is not constant during milling process. This results in altering forces and consequently, changing heat flux. Also, the varying chip load suggests that the heat conduction area is changing because most heat flows into the tool through the tool-chip contact area. The tool-chip contact area is closely related to the chip load in machining process.

Most studies modeled milling processes as an intermittent or interrupted cutting process. In early years, researchers modeled the cutting temperature by assuming cyclic heat flux or cyclic temperature at the tool-chip interface, such as an exponential rise and fall in the interface temperature (Okushim and Hoshi, 1963), a combination of cosine and exponential functions to define the interface temperature (Bhatia et al., 1980), a rectangular pulse heat flux (Wu and Mayer, 1979), and a periodic harmonic heat flux (Chakraverti et al., 1982). The lack of adequate temperature measurements limited the ability of early authors to validate their modeling results. Stephenson and Ali (1992) developed a temperature model for interrupted cutting by considering the cutter as a semi-infinite rectangle with one corner heated by a time-varying heat flux. They performed turning tests on a slotted tube to simulate the interrupted cutting process. Although experimental results showed that the model underestimated the temperature, especially in short heating cycles, their technique to measure temperature was used for validation in later publications. Radulescu and Kapoor (1994) developed an analytical model to predict tool temperature by solving energy balance in a heat transfer problem at the tool-chip interface. They analyzed the problem in a face milling process with inserts but validated the model with the experimental results in Stephenson and Ali's study (1992), which is interrupted turning process. Lazoglu and Altintas (2002) modeled the milling temperature by discretizing the chip thickness in the time frame during one tool revolution, and used a finite difference method to predict the steady-state tool and chip temperature at each time. Time constants are also determined based on thermal properties and boundary conditions, and used along the steady-state temperature to estimate the transient temperature of the tools. This modeling technique put the time-dependent heat flux into considerations by using the discretized chip load to calculate time constants.

3.3.2 Coolant Effects

Applying coolant or not in the machining process is always a worthy discussion. Coolant not only reduces the cutting temperature during the process, but also provides lubrication between the tool and workpiece and reduces the cutting forces. It also flushes the chips away and helps chip evacuation during the machining processes. However, the toxicity of the cutting fluid degrades the quality of the environment, sometimes even affects the quality of the product. Some researchers also suggested that using coolant in interrupted cutting will result in temperature drop and the occurrence of thermal stress. In the titanium machining process, coolant is strongly recommended to reduce the high cutting forces and temperature for longer tool life (Ezugwu and Wang, 1997).

Most studies used experimental approach to investigate how the coolant affects the tool performance, such as testing different coolant application methods (Sun et al., 2006, Wu et al., 2006, Sharma, et.al, 2009), and different coolant supply parameters (Kovacevic et al. 1995, Nandy and Paul, 2006). Although a better tool performance comes from reduced cutting force and temperature when applying coolant, very limited studies use experimental approach to directly relate the coolant effect to temperature due to inadequate measurement technique.

Very few cutting temperature models considered the effect of coolant. Dowson and Malkin (1984) modeled the temperature in orthogonal cutting, and considered the boundary of the tool as convection boundaries instead of adiabatics to capture cooling effects at the tool surfaces that do not contact the chip. However, they used arbitrary convection coefficients. Childs et al. (1988) discussed about the heat-transfer coefficients, and applied a constant coefficient in all different cutting cases. Berliner and Krainov (1991) developed a pure analytical model for the temperature calculation in metal cutting process including the effect of cooling. However, their model did not include practical consideration and the results were not validated. Li (1996) further determined the heat-transfer coefficients by analyzing the effects of the jet-flow rate of cooling. All these studies applied finite elements method to determine the temperature distribution in the cutting region.

3.4 Limitations of the Existing Models

From the literature review, there is a lack of proper modeling technique for the milling tool temperature. Most of the temperature models in milling process have been approximated by the interrupted turning process. However, milling process is not only interrupted cutting. The varying chip load, cutting forces and the tool-chip contact area are the main factors that make the modeling of milling process difficult. All these factors are not fully covered when approximating with interrupted turning. The previous modeling techniques did consider the varying heat input by applying cyclic heat flux, but no study discussed the varying heat input area.

Moreover, the coolant effects have not been covered in previous researches. The heat loss due to cooling is not only based on the coolant application method but also related to the temperature of the exposure surface. Also, due to the varying chip-tool contact length, partial of the tool exposes to the coolant and experiences heat loss before leaving the cutting cycle. The milling tool is under an unsteady heat transfer situation during the whole tool revolution, and the temperature change in the tool results in thermal stress which causes damages in the tool. In this study, the heat flux is calculated directly from the forces. The heat input area, the coolant effects, and the extra heat generated from the tool wear are all considered in this proposed model.

3.5 Modeling of Tool Temperature

First, the concept of dividing the ball-end mill flutes into numerous wedge-shaped elemental cutting tools (ECT) is applied in the modeling of tool temperature as well as cutting forces, as shown in Figure 3.1. This concept has been accepted in cutting temperature modeling of the ball-end milling process (Shatla and Altan, 2000). Each ECT performs a metal cutting operation, so the cutting forces and heat generation for each ECT can be obtained individually. From its cutting forces and generated heat, the temperature of each ECT is calculated.

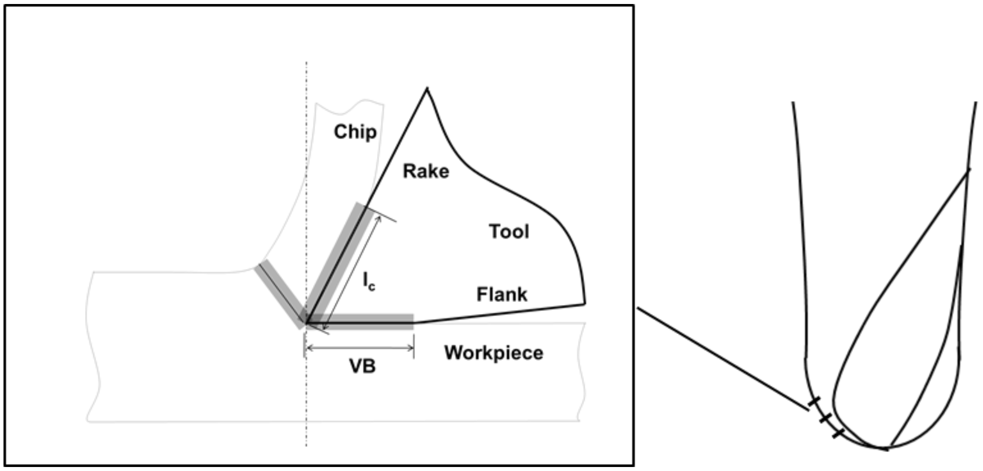

Figure 3.1: Elmental cutting edge on the flutes of ball-end mill

3.5.1 Analysis of Heat Flow into the Tool from the Rake Surface

In metal cutting, the energy consumed by each ECT includes two main componenets. The first is the shear energy along the shear plane resulted from the deformation associated with chip formation. The second is the friction energy along the tool rake face as a result of the frictional resistance between the chip and tool (Da Silva and Wallbbank, 1999, Komanduri and Hou, 2000, Adukhshim, et al., 2006). These components are illustrated as the dark area in Figure 3.1. Partial heat generated from the tool-chip friction flows to the tool from the chip-tool contact surface. At the same time, shear energy causes an increase in the chip temperature, which affects the heat conduction from the tool-chip contact zone. The heat flow into the tool is given from Bono and Ni's study (2006).

$$q''_{rake} = \frac{\Delta T_s + q''_{rf} L_{chip}}{L_{tool} + L_{chip}} \tag{3.1}$$

The heat generated by the frictional force on the rake surface can be obtained from the energy generation equation.

$$q''_{rf} = F_f V_{chip} \tag{3.2}$$

The frictional force F_f is obtained from the developed force model in section 2.3.1. V_{chip} can be related to the cutting velocity by using Merchant's shear model (Merchant, 1944). The heat partition factors L_{chip} and L_{tool} are calculated mainly based on the material properties and the cutting parameters (Bono and Ni, 2006).

$$L_{chip} = 0.754\sqrt{\frac{l_c}{V_{chip} k_w \rho_w c_w}} \tag{3.3}$$

$$L_{tool} = 2\sqrt{\frac{t_c}{\pi k_t \rho_t c_t}} \tag{3.4}$$

The average temperature rise on the shear plane ΔT_s is based on Loewon and Shaw's (1954) cutting tool temperature model in orthogonal cutting and the main equation is listed in equation (3.5).

$$\Delta T_s = \frac{R_1 F_s V_s}{J c_w \rho_w V b t_c} + \theta_o \tag{3.5}$$

All the machining process related parameters can be obtained from the force model in section 2.5 and the Merchant's shear model (1944). R_1 is the fraction of the heat that flows to the chip from shear plane and is given as:

$$R_1 = \frac{1}{1 + 1.328\sqrt{\frac{k_w \gamma}{V t_c}}} . \tag{3.6}$$

3.5.2 Analysis of Heat Flow into the Tool Due to Flank Wear

When the tool is sharp, it is generally assumed that there is no contact between the flank and the machined surface because of the clearance angle. However, when flank wear occurs, friction between the tool and workpiece generates heat.

$$q''_{ff} = F_{cw} V \tag{3.7}$$

F_{cw} is obtained from the force model of worn tools as explained in section 2.7. The effect of the shear plane energy is limited on the flank surface. Therefore, the way to determine the fraction of heat flowing to the tool is different from that on the rake surface.

The fraction (R_{fw}) of the friction energy to the workpiece is calculated according to the model developed by Berliner and Krainov (1991).

$$R_{fw} = \left\{1 + \frac{\pi VB}{2t_c P_e \ln(2b/VB)}\right\} \tag{3.8}$$

The Peclet number P_e is determined by equation (3.9).

$$P_e = \frac{V(VB)}{\kappa_t} \tag{3.9}$$

The heat flow to the tool from the flank can be obtained simply by the fraction of the total generated heat.

$$q''_{flank} = (1 - R_{fw})q''_{ff} \tag{3.10}$$

3.5.3 Analysis of the Effect of Coolant

In most machining processes, coolant is applied to reduce cutting temperature. However, due to the complexity in modeling and the difficulty in experimental validation, most studies only considered dry cutting. Coolant has been applied by an overhead nozzle in this study. The coolant is assumed to reach all the exposed surfaces of the tool during cutting. At the exposed surface, the coolant removes heat from the tool; therefore, convection is the main heat-transfer mechanism.

The heat transfer equation for convection is given in any heat transfer book such as Holman (1992).

$$q = hA(T_s - T_c) \tag{3.11}$$

T_s is the exposed surface temperature and A is the area of the exposed surface in the convection problem. The analysis of heat-transfer coefficient for both rake and flank surfaces of each ECT follows the study of Li (1996). In this study, the rake cooling is considered as an overhead jet nozzle aim on the tool tip, as shown in Figure 3.2.

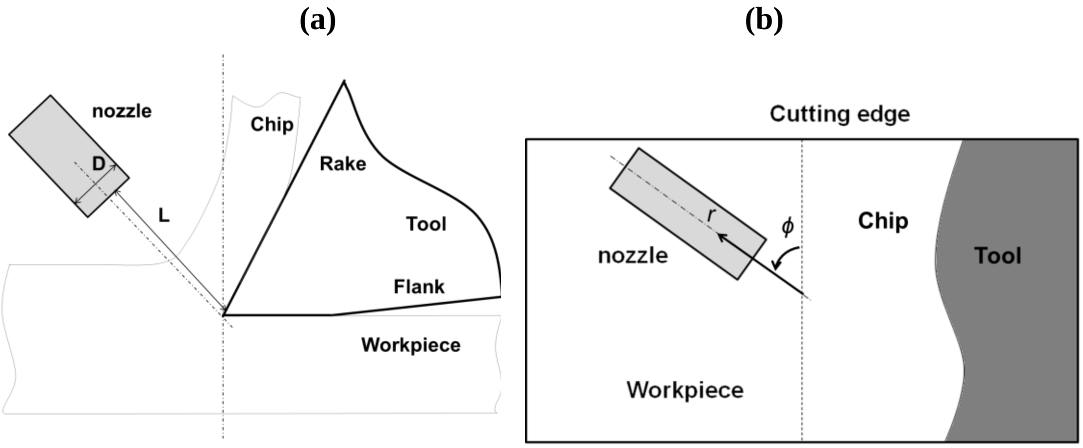

Figure 3.2: Illustration of coolant applied by jet nozzle (a) nozzle position (b) the view perpendicular to coolant axis (Li, 1996)

In Li's work, the local Nusselt number was obtained from another study (Goldstein and Franchett, 1988) using experimental approach to build the equation, as shown in equation (3.12).

$$Nu_r = 1.22 A \mathrm{Pr}_c^{1/3} \mathrm{Re}_r^{0.7} \exp\left[-(B + C\cos\phi)\left(r/D\right)\right]^m \tag{3.12}$$

r and ϕ are the coordinates of the surface which has its origin at the nozzle aim point (Figure 3.2(b)), and the coefficients A, B, C and m are related to the nozzle position and angle. For the milling process, the nozzle head is set to be at distance L_{nozzle} with an angle η_{nozzle} between the nozzle axis and tool axis. The axis of the nozzle can be represented as a vector form as the following equation.

$$\vec{N}_{nozzle} = \left(L_{nozzle}\sin\eta_{nozzle}, 0, L_{nozzle}\cos\eta_{nozzle}\right) \tag{3.13}$$

For each ECT on the milling tool, the coordinates r and ϕ are dependent on the midpoint (x_0, y_0, z_0) and the cutting edge vector $\vec{L}$.

$$r(x_0, y_0, z_0) = \sqrt{\left(L_{nozzle}\sin(\eta_{nozzle}) - x_0\right)^2 + y_0{}^2 + \left(L_{nozzle}\cos(\eta_{nozzle}) - z_0\right)^2} \tag{3.14}$$

$$\phi(\vec{L}) = \cos^{-1}\left(\frac{\vec{N}_{nozzle} \bullet \vec{L}}{\left|\vec{N}_{nozzle}\right|\left|\vec{L}\right|}\right) \tag{3.15}$$

The corresponding coefficients A, B, C and m according to the coordinates r and ϕ can be found in the table listed in Li's study (1996). The Nusselt number Nu_{rake}, Reynold number Re_{rake} and Prandtle number $\mathrm{Pr}_{coolant}$ can be obtained from a heat transfer book (Holman, 1992).

$$Nu_r = \frac{h_r D}{k_c} \tag{3.16}$$

$$\mathrm{Re}_r = \frac{\rho_c U_j D}{\mu_c} \tag{3.17}$$

$$\mathrm{Pr}_c = \frac{c_c \mu_c}{k_c} \tag{3.18}$$

By substituting equations (3.12), (3.17) and (3.18) into equation (3.16), the heat transfer coefficient can be obtained.

The flank cooling is assumed that the coolant flows in between two parallel surfaces, the flank surface and the workpiece. This assumption is reasonable because the clearance angle is always very small; in most cases it is smaller than 5 degrees. Based on this, the Nusselt number and Reynold number are calculated from the equations of heat transfer between parallel plates.

$$Nu_{flank} = \frac{h_{flank} L_{flank}}{k_{coolant}} = 0.664 \Pr_{coolant}{}^{1/3} \operatorname{Re}_{flank}{}^{1/2} \tag{3.19}$$

$$\operatorname{Re}_{flank} = \frac{\rho_{coolant} U_j L_{flank}}{\mu_{coolant}} \tag{3.20}$$

Similarly, substituting equations (3.18) and (3.20) to equation (3.19), the heat transfer coefficient on the flank surface can be obtained. With the known heat transfer coefficient, the heat loss on rake and flank surfaces can be calculated from the heat transfer equation (3.11).

3.5.4 Heat Conduction in the Tool

There are two main difficulties associated with the temperature model for the milling process: the complexity of the cutter geometry and the time-dependent chip load. The first difficulty is addressed by discretizing the mill cutting edge into numerous ECTs, assuming each ECT is involved in an independent orthogonal milling process. However, for each ECT, the chip load varies due to the rotation of the cutter. The varying chip load not only results in varying heat generation, moreover, it makes the chip-tool contact area change with time. Hence, the area of the heat input on the tool rake surface is not constant, and neither is the exposed area. In this study, the rake surface is discretized into several elements, where each element experiences a uniform time-dependent heat flux.

The heat flux is positive if there is heat flux coming into that element and negative if that element is exposed to the coolant.

Figure 3.3 illustrates the cutting process of a single ECT and shows how the rake and flank surfaces are discretized, as well as the heat flux on the surfaces. The heat flux is assumed to be uniform for each element on the ECT surface.

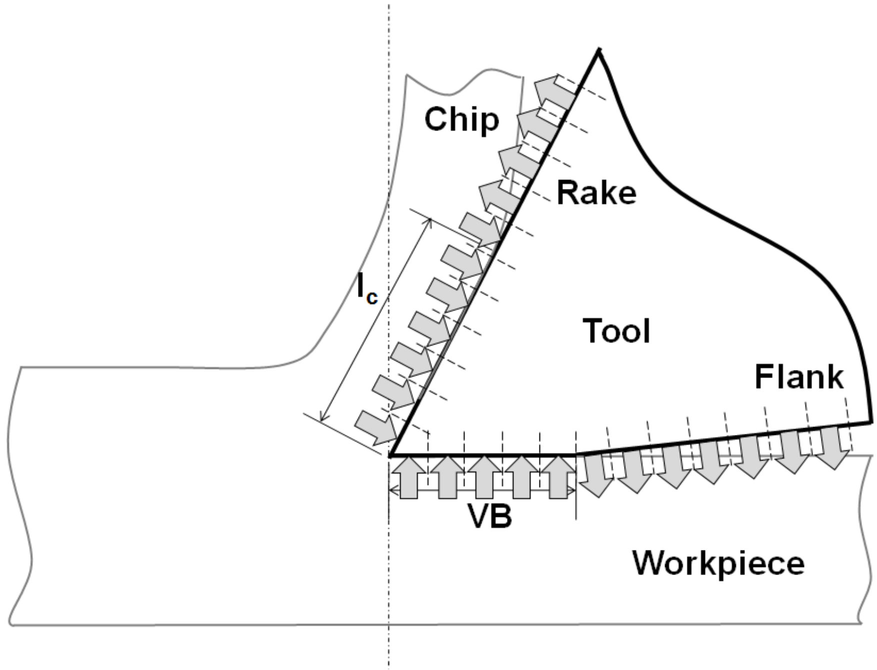

Figure 3.3: Discretization and heat flux on the tool rake and flank surfaces of each ECT

Each ECT is assumed as a semi-infinite plane with heat flowing in from the surface. First, the model starts from using the solution of temperature rise with a constant point heat source. The temperature rise at (u,v) in the semi-infinite plane with a constant point heat source q at $(x,0)$ flowing from time 0 to time t is given by (Holman, 1992):

$$\Delta T = \frac{2q}{k_t A}\left[\frac{\sqrt{\kappa_t t/\pi}}{\sqrt{(u-x)^2+v^2}}\exp\left(-\frac{(u-x)^2+v^2}{4\kappa_t t}\right)-\frac{1}{2}\left(1-erf\left(\frac{\sqrt{(u-x)^2+v^2}}{2\sqrt{\kappa_t t}}\right)\right)\right] \tag{3.21}$$

Since the heat flux from each element on the tool surface is assumed to be uniform, the point heat source can be integrated between the end points of the element. The temperature rise at point (u,v) with constant heat source between end point $A(a,0)$ and point $B(b,0)$, as shown in Figure 3.4, is written as equation (3.22).

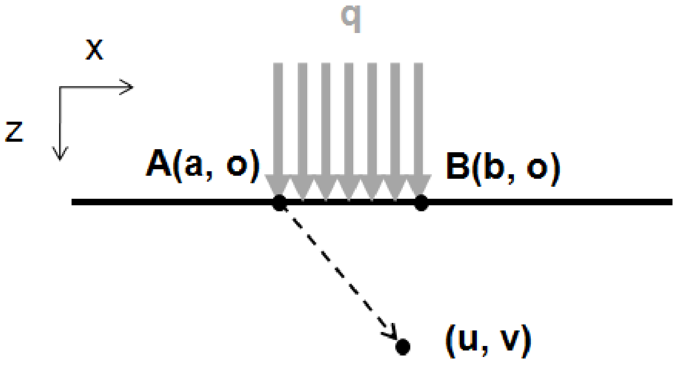

Figure 3.4: Uniform heat flux between two points on the surface of a semi-infinite plane

$$\Delta T = \int_a^b \frac{2q_0}{k_t A}\left[\frac{\sqrt{\kappa_t t/\pi}}{\sqrt{(u-x)^2+v^2}}\exp\left(-\frac{(u-x)^2+v^2}{4\kappa_t t}\right)-\frac{1}{2}\left(1-erf\left(\frac{\sqrt{(u-x)^2+v^2}}{2\sqrt{\kappa_t t}}\right)\right)\right]dx \tag{3.22}$$

However, in milling, the heat flux of each element is time-dependent but not constant. Thus a method to superimpose several different constant “heat flux differences” is proposed to calculate the total temperature rise due to varying heat fluxes. Figure 3.5 shows an arbitrary time-dependent heat flux, and how this time-dependent heat flux can be decomposed into several constant heat fluxes acting at different times.

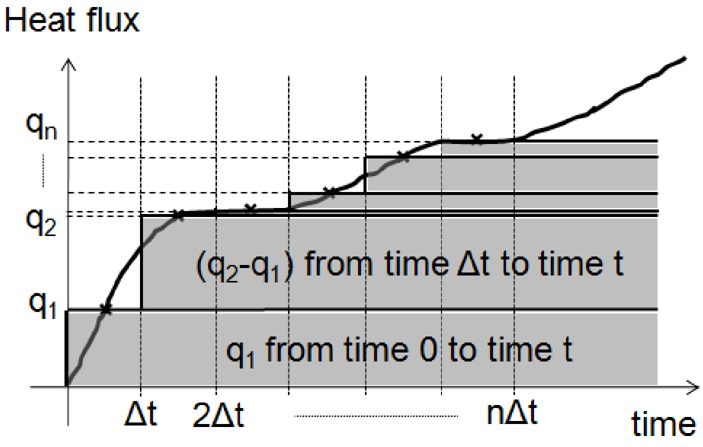

Figure 3.5: A time dependent heat flux and the superposition of constant heat flux

At each time interval Δt, the average heat flux is first determined. In Δt time, there is only one constant heat flux q_1. In $2\Delta t$ time, there are two different constant heat fluxes adding with each other: q_1 flowing in for $2\Delta t$ time and $(q_2 - q_1)$ flowing in for only Δt time. Similarly, in $3\Delta t$ time, there are q_1 flowing in for $3\Delta t$ time, $(q_2 - q_1)$ flowing in for $2\Delta t$ time and $(q_3 - q_2)$ flowing in for Δt time, etc. The total temperature rise from the time-dependent heat flux is the superposition of all constant heat fluxes.

$$\Delta T = \sum_{i=1}^{m} \frac{2(q_i - q_{i-1})}{k_t A} \int_a^b \left[\frac{\sqrt{\kappa_t (i\Delta t)/\pi}}{\sqrt{(u-x)^2+v^2}} \exp\left(-\frac{(u-x)^2+v^2}{4\kappa_t (i\Delta t)}\right) - \frac{1}{2}\left(1-erf\left(\frac{\sqrt{(u-x)^2+v^2}}{2\sqrt{\kappa_t (i\Delta t)}}\right)\right) dx \right] \qquad (3.23)$$

m is the number of time intervals in one tool revolution. The heat flux from one element on the rake surface may be negative when the ECT first engages in cutting, positive when the chip load becomes larger, and then negative when the ECT is near the end-of-cut. Finally, any point in the ECT experiences heat flux from all elements on both the rake and flank surfaces. By summing the ΔT from the time-dependent heat flux in each element, the temperature rise in the ECT during the milling process can be obtained.

Figure 3.6 shows the flow chart of the temperature calculation in the tool. From the mechanistic force model, the heat generation and the heat input area can be calculated. When the tool first starts cutting, heat starts generating and conducting into the rake and flank surfaces at the tool-chip and tool-workpiece contact surfaces. At this time, the tool surfaces which are exposed to the coolant are assumed to remain at room temperature and there is no heat loss to the coolant. The temperature on the rake and flank surfaces at the very beginning of cut can be calculated from the heat generation data from the force model.

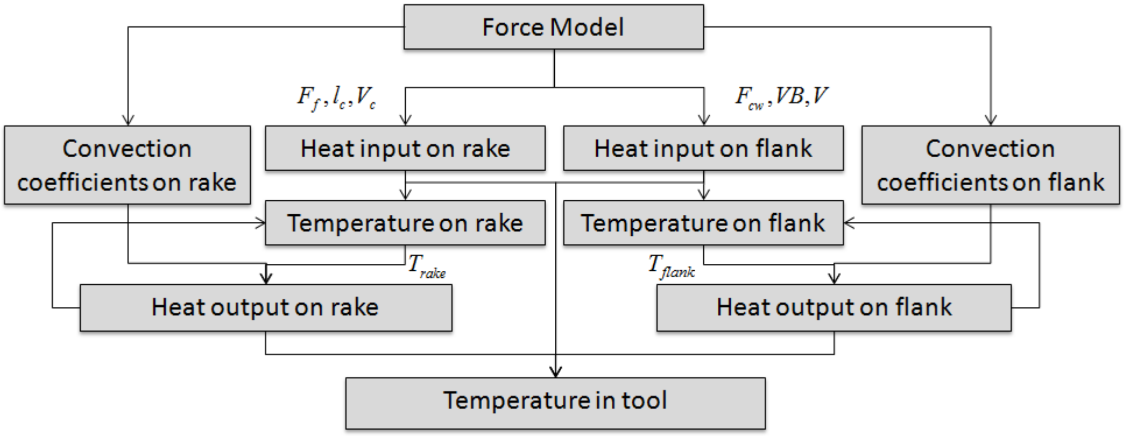

Figure 3.6: Flow chart of temperature calculation in the tool

Now the temperatures on the rake and flank surfaces have been obtained. From the temperature difference between the surfaces and coolant, the heat loss from the exposure surfaces is able to be calculated. Any point in the tool now experiences heat flows in from tool-chip contact area, heat loss on the rake surface, heat flows in from the tool-workpiece contact area, and heat loss on the flank surface. The temperature rise at that point is the summation of the temperature difference due to all the heat sources and heat sinks. The temperatures on the rake and flank surfaces are updated considering the heat loss, too.

3.6 Modeling Results and Discussion

In the proposed temperature model, the forces must be known as inputs. The forces are calculated based on the force model in Chapter 2.

Figure 3.7 shows the estimated temperature for one ECT during half of one rotation of the ball-end mill. The modeled cutting condition is 500 rpm and 0.23 m/min feed rate, and the modeled ECT is at 1.27 mm height on the ball-end mill cutting edge. The x axis is the tool rotation angle and the ECT starts cutting at 0°. The ECT is at room temperature before cutting. The temperatures at five different points on the tool rake surface are plotted, the first at a distance 0.005 mm away from the ECT tip and the next at 0.01 mm away from the ECT tip. From Figure 3.7, it is clearly seen that the maximum temperature does not occur at the point nearest the ECT tip, but at a point 0.015 mm away from the tip. This result agrees with the findings in other literatures that the maximum temperature is not located right at the tool tip but at the middle of the tool-chip contact area (Da Silva and Wallbbank, 1999, Komanduri and Hou, 2000, Adukhshim, et al., 2006). The final drop is because the tool-chip contact length becomes small at the end of cut, thus these points experience more heat loss due to coolant than heat input due to cutting.

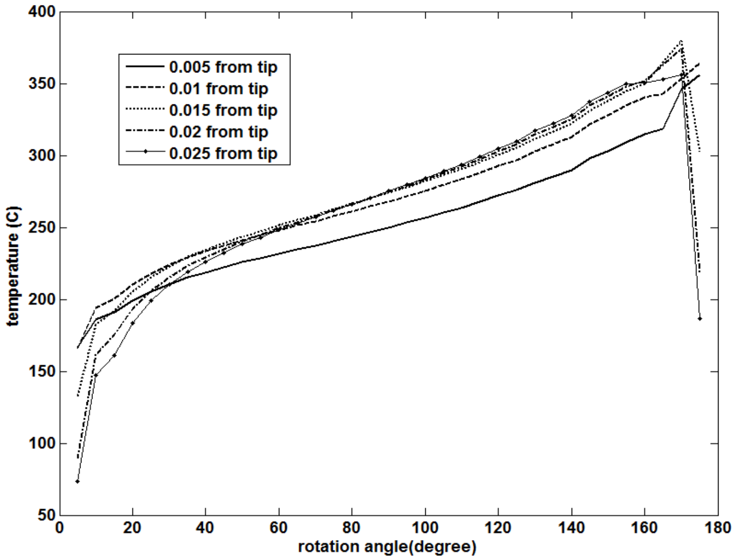

Figure 3.7: Modeling result of 500rpm, 0.23m/min feed rate, at 1.27 mm height ECT

How to define the elements on the surfaces is one big issue because it will affect the heat input and output area. In the model, the maximum tool-chip contact length l_c during one revolution is considered as one unit because this is the maximum distance that has heat flow in. The rest of the rake surface will only experience cooling. However, the calculation time is too long if the whole rake surface is considered, and actually, the cooling effect on the elements far away from the ECT tip is limited. Figure 3.8 shows the modeling results when considering $1\max l_c$, $2\max l_c$ and $3\max l_c$ on the rake surface. It is seen that there is only slightly difference in the modeling results between $1\max l_c$ and $2\max l_c$. As for $2\max l_c$ and $3\max l_c$, the temperature difference is within 0.1%. That is because the cooling convection depends on the interface temperature; when the element is away from the heat flowing zone, the temperature is not high and thus the cooling effect is not significant. Finally, $2\max l_c$ has been chosen to be the total heat flux boundary on the rake surface.

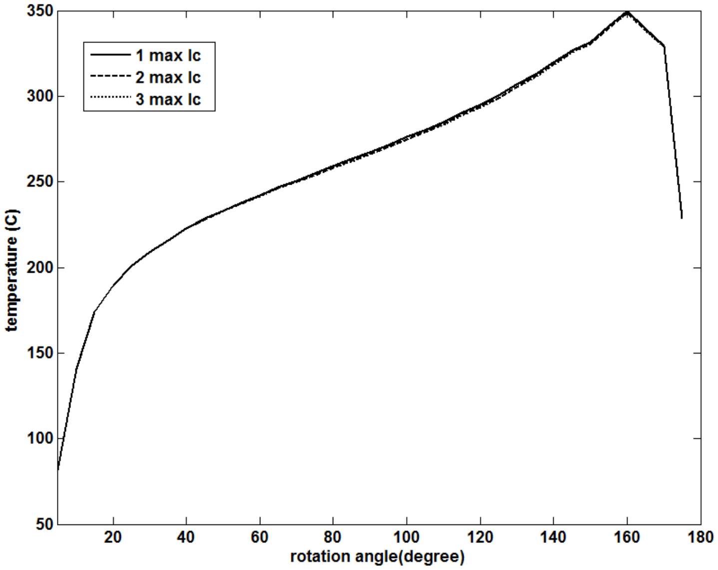

Figure 3.8: Comparison of different interested total length on rake surface

Another issue is about the number of elements to be divided in the tool-chip contact area. The more number of elements, the higher resolution the model has and the more accurate result can be obtained. On the other hand, longer calculation time is required. Figure 3.9 shows the modeling results when assuming different number of elements on the rake surface. The first data shows the modeling result of total 20 elements on the rake surface, which means 10 elements are within the maximum tool-chip contact length and 10 elements experience cooling all the time. When the element number reduce to 10 elements, the modeling temperature becomes higher, which might be due to the over-estimated heat flowing area. However, when increasing the element number to 30 and 40, the modeling results start to converge. Therefore, 30 total elements is divided on the rake surface in this study. Similar process has been taken on the determination of the number of elements on the flank surface. The length of $2VB$, which is divided into 6 elements, reaches good result because the tool-workpiece contact length is not changing during the tool revolution.

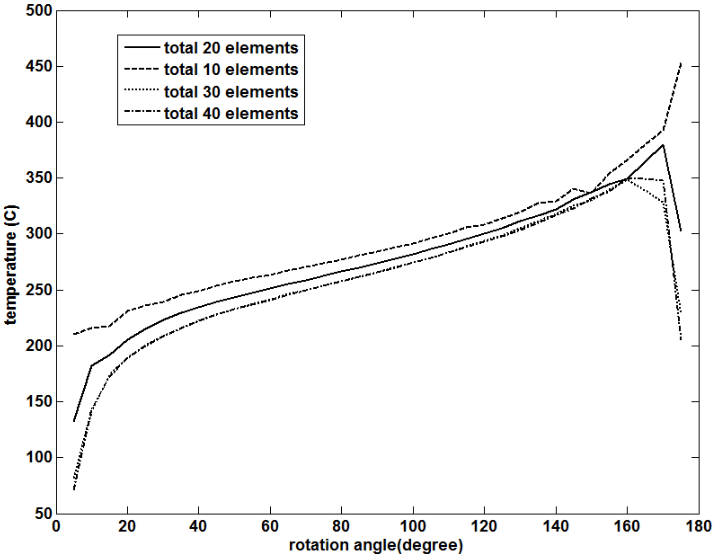

Figure 3.9: Comparison of different number of elements on the rake surface

Figure 3.10 compares the estimated temperature of different ECTs on the ball-end mill. Different ECTs have different heights and cutting edge radii. The higher ECTs have larger radii and therefore higher cutting speed. Also, higher ECTs experience larger chip loads and cutting forces. Hence, higher ECTs have higher estimated temperatures than

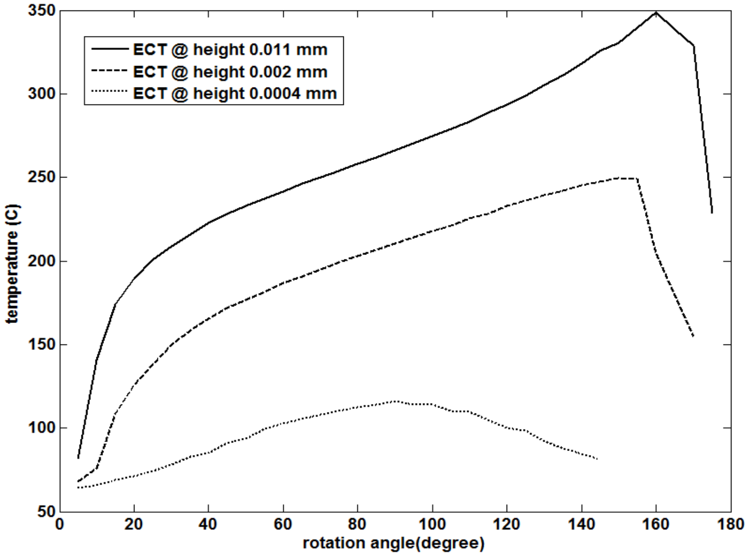

Figure 3.10: Comparison of different ECT on the cutting edge

the lower ECT as shown in Figure 3.10.

The effect of tool wear on the estimated tool temperature is shown in Figure 3.11. From Figure 3.11, the estimated temperature increases by 10°C when $VB = 0.3$ mm, a common tool failure criterion. This might be due to the conservative simulated cutting condition. The additional heat generation due to flank wear comes from the friction between the flank wear area and workpiece. However, the cutting velocity is low and thus the heat generated due to friction is much less than the heat generated due to cutting. Therefore, the estimated tool temperature is not significantly affected by tool wear.

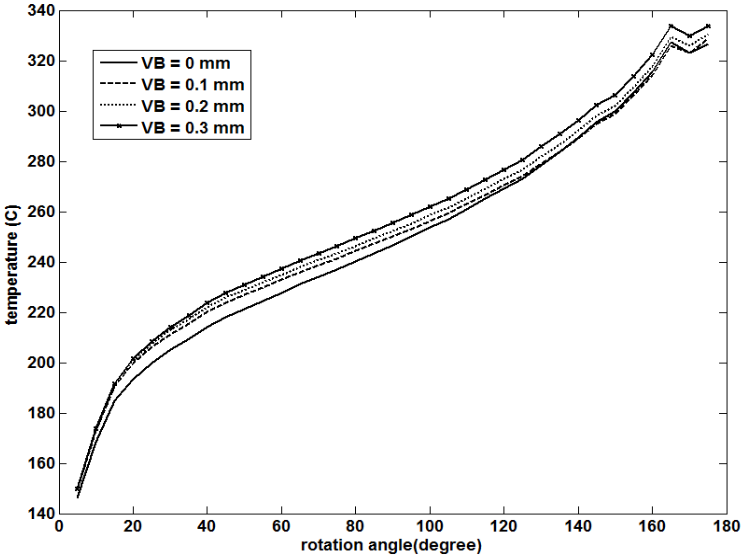

Figure 3.11: Comparison of different flank wear VB

Finally, the estimated transient temperature of one full tool revolution is plotted in Figure 3.12. In the milling process, each ECT only engages with the workpiece during half of one complete rotation of the tool. The ECT cools down during the rest of the tool rotation. The temperature rise and fall during the entire rotation causes thermal stress, and is one reason for tool failure. The cooling portion of the tool rotation is calculated by considering cooling effects on the rake and flank surfaces without any heat flux input. The modeling result shows a reasonable temperature change during the whole revolution of the milling tool.

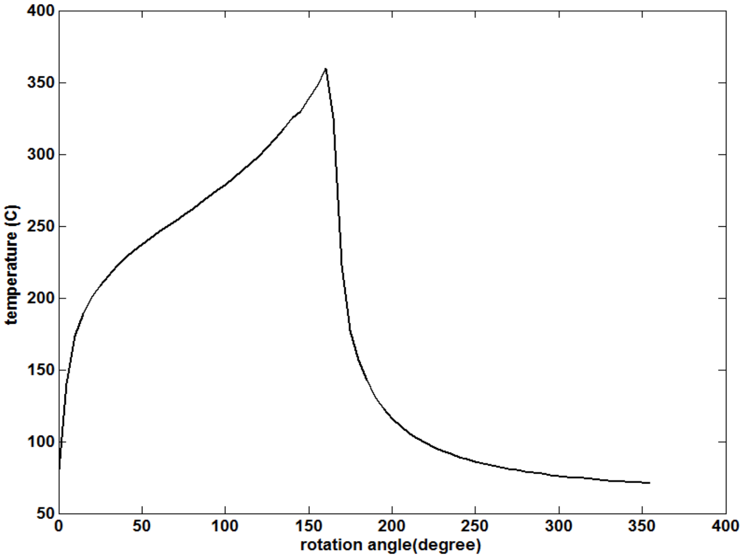

Figure 3.12: The transient temperature of a ECT in a full revolution

3.7 Temperature Measurement and Validation

3.7.1 Experimental Setup

Most researches assumed intermittent or interrupted cutting to approximate the milling process (Olushim and Hoshi, 1963, Wu and Mayer, 1979, Bhatia et al., 1980, Chakraverti et al. 1982, Stephenson and Al, 1992). Thus, they used intermittent cutting processes to validate their modeling results. In milling, temperature measurement is very difficult. Thermocouples cannot be embedded in the rotating tool at the cutting location. An infrared camera is often used to measure cutting temperature; however, with the use of the coolant, the camera view is blocked and cannot aim at the cutting zone. The drill-foil thermocouple method proposed by Bono and Ni (2002) for measuring drilling temperature is applied in this study. This method is not affected by the coolant supply and the interrupted cutting. However, the feed direction in milling is different from that in drilling. Therefore, the foil layer in the workpiece was embedded in the feed direction as shown in Figure 3.13. In this setup, every time the cutter contacts with the foil layer, a hot thermoelectric junction was formed. With the tool and workpiece connecting to a cold reference junction, a series of voltage peaks that are proportional to the junction temperature were measured. A 0.13 mm thick copper foil was embedded and 0.26 mm thick plastics were used to insulate the copper foil from the workpiece. The copper foil was embedded at different distance from the tool center to validate the temperature of different ECTs on the cutting edge. From the modeling results, the tool temperature increases during cutting. Therefore, tests with the copper foil embedded at the beginning-of-cut half, which is before the maximum chip load position, and at the end-of-cut-half, which is after the maximum chip load position, were both conducted.

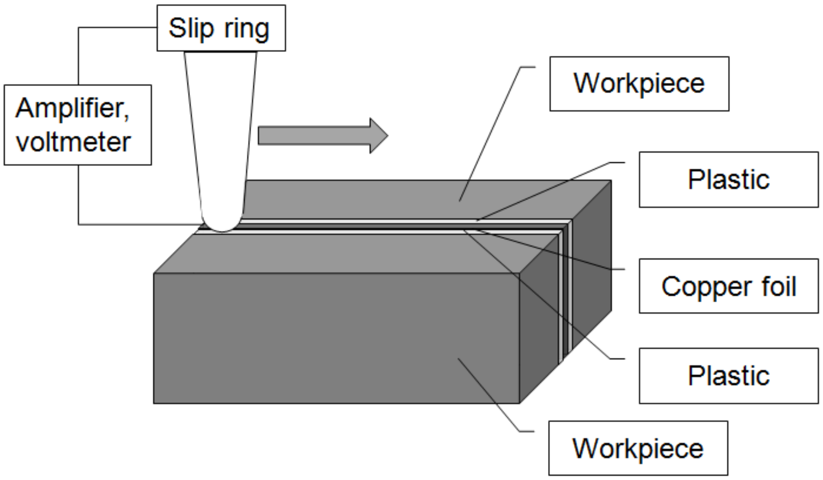

Figure 3.13: Basic elements of the tool-foil thermocouple system

The ball-end mill used in the validation experiments was the same as in section 2.8.1.1. The cutter geometry was extracted from the CAD model of the tool. The workpiece material was Ti 17 as well. The coolant was 5% CIMTECH 310 mixed with 95% water. The spindle speed was 500 rpm, the feed rate was 0.23 m/min and the depth of cut was 1.27 mm, and the sampling rate was 1000 Hz.

3.7.2 Calibration Test for WC-Co and Copper

Before the cutting, the thermoelectric temperature measurement system needed to be calibrated to determine the relationship between the thermoelectric emf and the temperature. The emf and temperature relationship depends on the materials. In this study, the electric flows through a circuit connecting between the tool (WC-Co) and the embedded foil layer (copper). Therefore, a calibration test needs to be conducted using these two materials. The calibration test was based on the process detailed in Stephenson's work (1991), and the setup is shown in Figure 3.14.

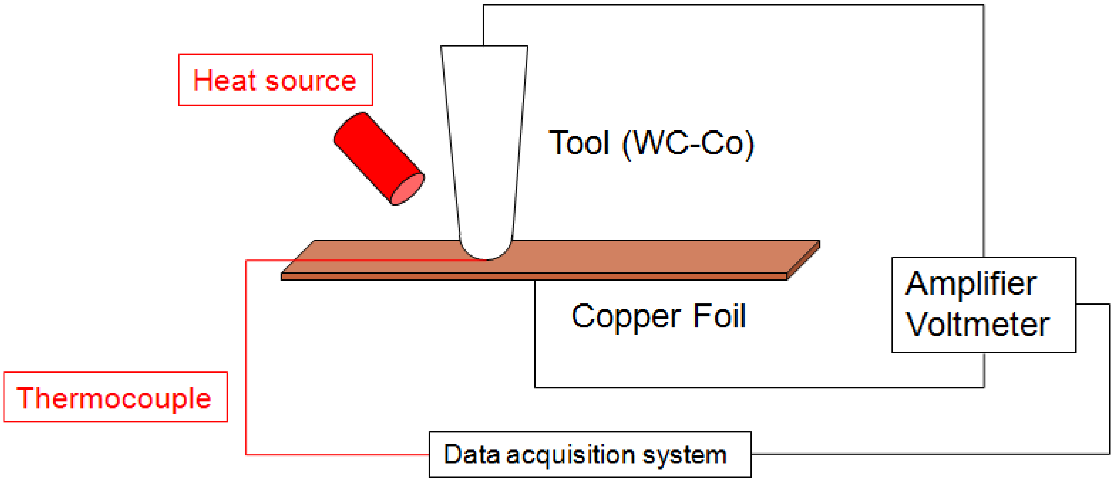

Figure 3.14: The setup of calibration test

There was a complete circuit connecting the tool and workpiece with the voltmeter. A thermocouple was attached to the tool-workpiece contact zone. Both signals were recorded by the data acquisition system developed by National Instrument. A propane torch aimed and heated at the tool-copper junction point. Due to the temperature difference of hot and cold junction in the circuit, the voltage changed when the temperature of the heating point increased. At the same time, the thermocouple measured the temperature at the hot junction. The temperature collecting by thermocouple and the corresponding voltage signal are shown in Figure 3.15.

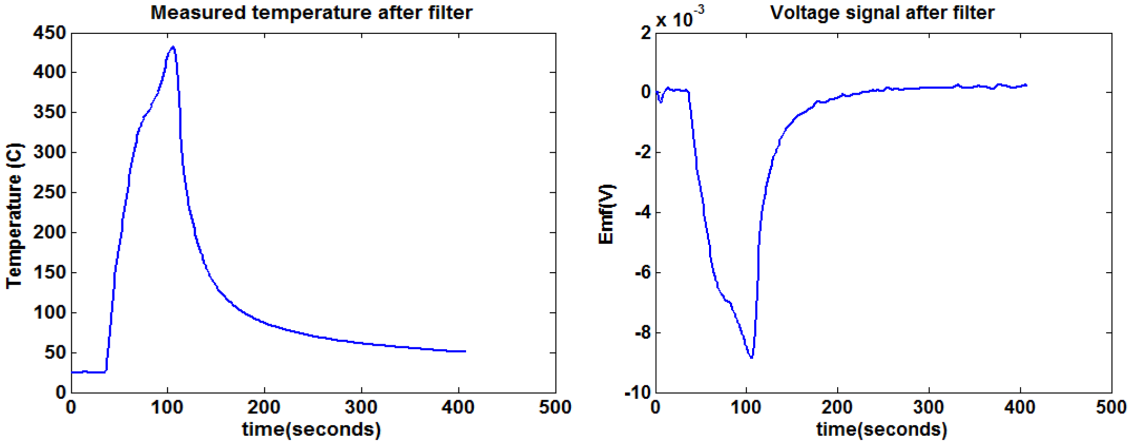

Figure 3.15: The measured temperature and corresponding voltage signal in calibration test

Figure 3.16 shows the thermoelectric calibration results. Five sets of calibration tests were conducted and showed consistent results. The fitted line is almost linear. Therefore, it is acceptable to use extrapolation when the measured emf is out of the calibration range.

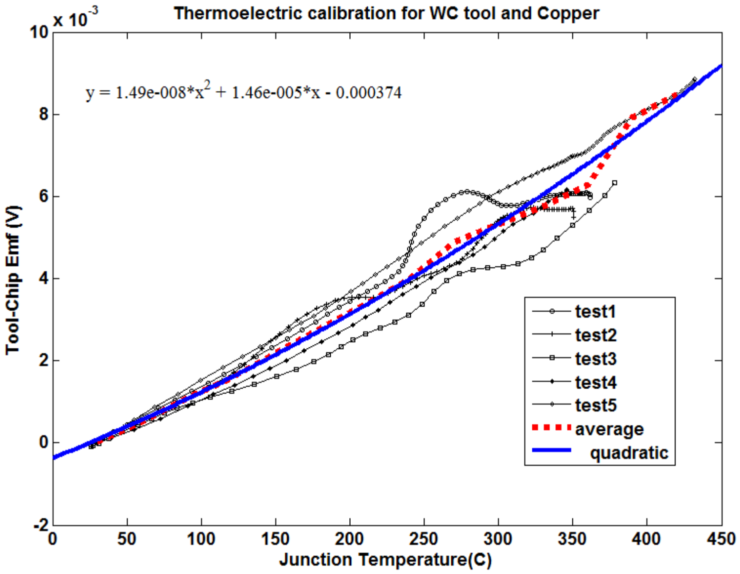

Figure 3.16: Thermoelectric calibration for the copper and WC combination

3.7.3 Experimental Results

Figure 3.17shows the voltage signal when the copper foil is embedded at a distance of 0.05 mm from the tool center, after the maximum chip load position. Peaks occur when the tool contacts the copper; the small peaks are the emf from the short flutes while the larger peaks are from the long flutes. The average emf of all the large peaks is

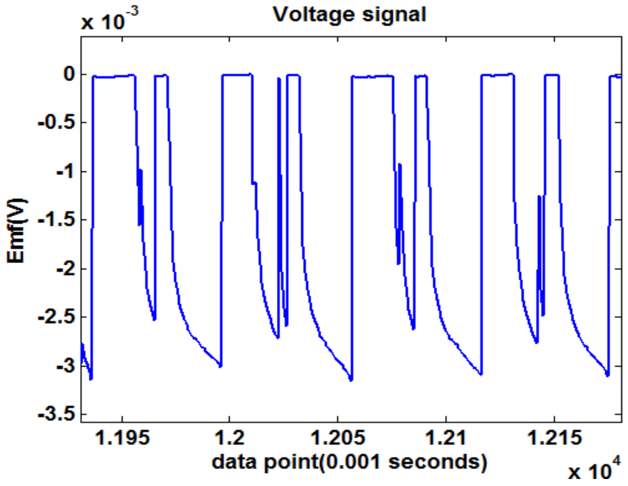

Figure 3.17: Experimental results for copper 3.3 mm from tool center

calculated and the corresponding temperature can be obtained from the thermoelectric calibration tests.

The measured temperature is compared with the estimated temperature to validate the modeling result. Figure 3.18 compares the measured and estimated temperature for different ECTs at the end-of-cut half. The end-of-cut temperature of the ECT in the model is used for validation. The error bar for the experimental data is the standard deviation of experimental results, and the error bar of the modeling data is the standard deviation of the calculated temperature within tool-chip contact area. As the ECT radius increases, the cutting velocity and the chip load increase, which lead to higher generated energy and tool temperature. From Figure 3.18, it is shown that the experimental results match the modeling results well.

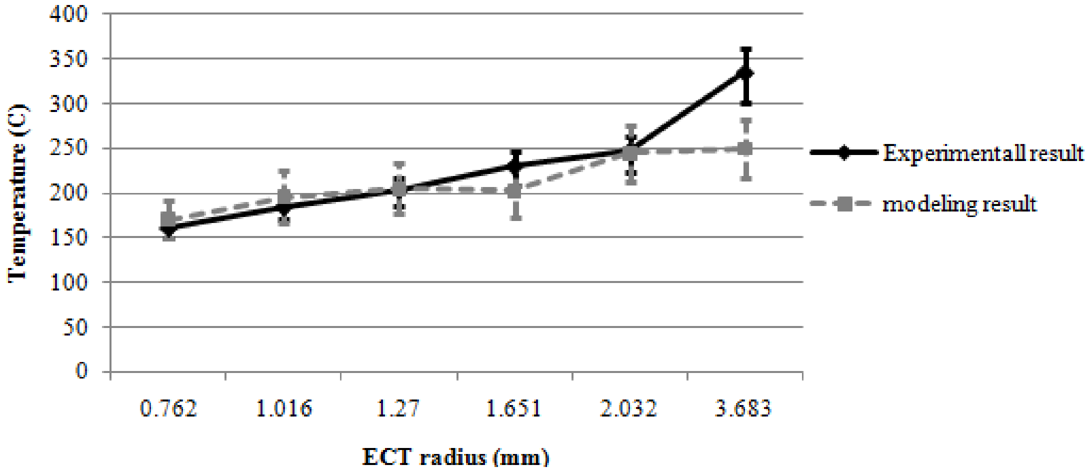

Figure 3.18: Validation results for different ECT at the end-of-cut half

Figure 3.19 shows the validation results for different ECTs at the beginning-of-cut half. It is clearly seen from Figure 3.19 that the estimated and measured results agree well. Moreover, by comparing Figure 3.19 with Figure 3.17, the estimated and measured temperatures are much lower in Figure 3.19 than in Figure 3.17. This shows the transient temperature of the milling process can be captured from the model.

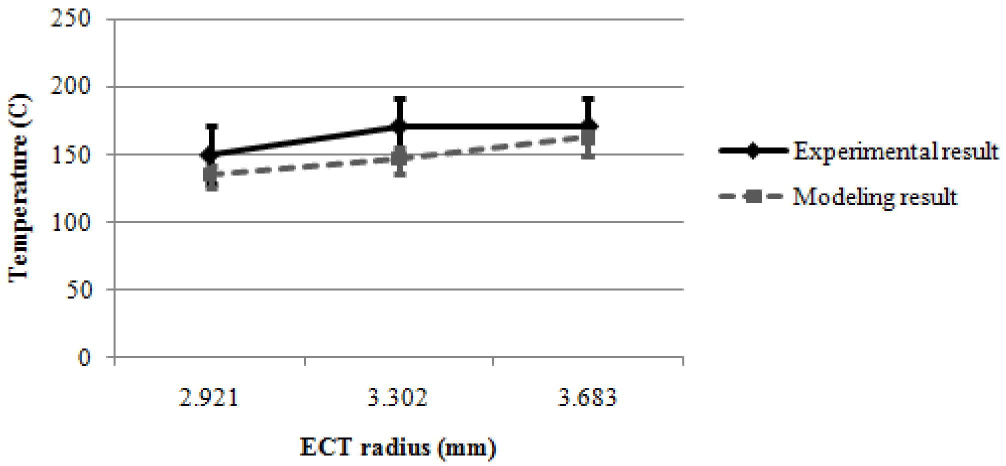

Figure 3.19: Validation results for different ECT at the beginning-of-cut half

The cutting temperature with the use of worn tool has also been validated. Since the flank wear is not uniformly distributed along the entire cutting edge, the width of the flank wear at different ECT is measured and then used in the model. Figure 3.20 shows the good agreement between the estimated and measured temperature. Comparing Figure 3.20 with Figure 3.17, both experimental and modeling results show that the flank wear does not significantly affect cutting temperature under this cutting condition.

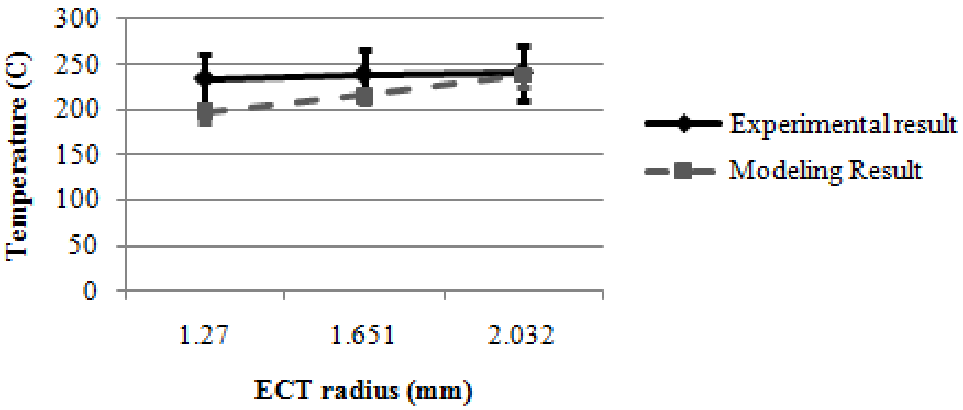

Figure 3.20: Validation results for different ECT with flank wear

Finally, three different cutting conditions with sharp tool have been tested to validate the model. The cutting conditions are listed in Table 3.1.

Table 3.1: Validation experimental conditions

Test condition number	Spindle speed (rpm)	Feed (m/min)	Axial depth of cut (mm)
1	500	0.23	1.27
2	1000	0.46	1.27
3	1500	0.69	1.27

The experimental and modeling results are shown in Figure 3.21. It is clearly seen that near the tool tip, the cutting temperature is similar for all three tests. However, as the ECT radius increases, the higher spindle speed case has significantly higher cutting temperature. This is because the spindle speed is the main cutting parameter which affects the cutting velocity. For the larger radius ECTs, the effect of the higher cutting velocity on the generated heat and resultant cutting temperature is more significant. Both experimental and modeling results show the trend and they agree with each other very well.

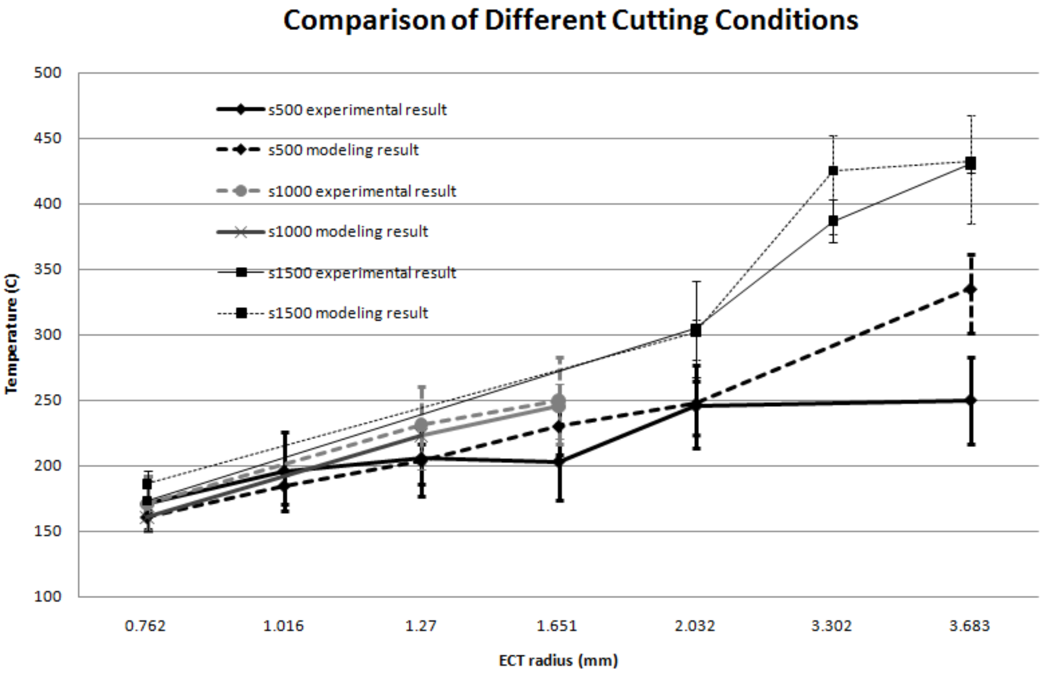

Figure 3.21: Validation results for different cutting condition

3.8 Conclusions

This study proposes a temperature estimation model for milling process and considers both coolant effects and tool wear. The transient temperature during the cutting cycle is calculated based on the time-dependent heat generation and the varying tool-chip contact area. Moreover, a tool-foil thermocouple method is used to measure the cutting temperature during the milling instead of the traditional embedded thermo-couple method. This measuring technique is able to reach the real cutting zone with simple and easy experimental setup. Finally, the good agreement between the experimental and modeling results validates the proposed model with the use of sharp and worn tools in different cutting conditions.

CHAPTER 4

INTEGRATED MODEL FOR TOOL WEAR ESTIMATION AND TOOL LIFE PREDICTION

4.1 Nomenclature

d_w	the depth of flank wear
F	normal load in Archard's wear equation
F_{cut}	cutting force of ECT
F_{cw}	component of force in cutting direction on flank surface due to wear
F_f	frictional force on rake surface of ECT
F_{th}	thrust force of ECT
F_{tw}	component of force in thrust direction on flank surface due to wear
f	ratio between the shear strength of worn surface to the shear flow stress
H	temperature dependent hardness
K	wear coefficient
k	shear flow stress
L	width of cutting edge of ECT
R_{ECT}	radius of ECT
S	sliding distance

S_{rev}	cutting length of ECT in one revolution
t_c	uncut chip thickness
t_c'	cut chip thickness
V	cutting velocity
VB_e	flank wear of ECT
W_{ad}	worn volume by adhesion
α_n	normal rake angle of ECT
θ	clearance angle of ECT
η_c	chip flow angle of ECT
σ_0	tool tip normal stress of ECT
γ	shear strain

4.2 Introduction

For the machining process, tool wear is the most direct phenomena which can determine whether the tool is failed or not. When machining using worn tools, the forces increase and result in the instability of machining process. Moreover, using worn tool may lead to dimensional error of the machined product due to the change of cutter geometry. Also, the increasing contact area between the tool and workpiece on the flank surface will cause ploughing or rubbing effects on the machined surface and degrade the roughness of the surface.

In industry, understanding the tool wear situation on the manufacturing line is very important. Several on-line detection techniques have been utilized to monitor tool failure during the machining process. One of the commonly used methods is to monitor the force signal during the process. When the tool starts to wear, extra force is generated due to the contact between the tool flank surface and workpiece. With setting threshold of the forces, the tool can be changed before excessive tool wear occurs and damages the workpiece.

In this study, the concept of increasing forces due to tool wear is extended to a wear progression estimation model. By considering the relationship between the tool wear and the forces due to tool wear, a model is proposed to predict how the tool wear and forces grow along with cutting time. Validation experiments are performed starting with a new tool used for slot cutting. The force data is collected and the tool wear is measured periodically to be compared with the modeling results.

4.3 Literature Review

4.3.1 Tool Wear Model

The modeling of tool flank wear has been long studied. It is generally believed that wear is complicated; several different wear mechanisms might be involved in one process (Meng and Ludema, 1995, Kato, 2002). Among all different wear mechanisms, abrasion, adhesion and diffusion are considered as the dominant mechanisms which lead to flank wear. Some researchers believed that all three mechanisms contribute to the progression of flank wear. They assumed that the wear mechanisms are independent, and they combined different individual wear mechanism models into one tool flank wear model. Luo et al. (2005) simply combined abrasion/ adhesion model from Archard (1953) and diffusion model from Usui and Shirakashi (1984) by adding the two different wear models together for the prediction of flank wear of carbide tool inserts. Huang and Liang (2004) modeled the flank wear in orthogonal cutting by adding the flank wear from abrasive wear model (Rabinowicz et al., 1961), adhesion model (Usui et al, 1978), and diffusion model (Kannatey-Asibu, 1985). Similar approach has been taken by Li and Liang (2005, 2007). Their model has been validated under both dry and flood coolant machining processes.

There are two main concerns of these models. First, a lot of experiments needed to be conducted in order to fit the wear coefficients of each wear mechanism. The coefficients of each wear mechanism needed to be determined from series of calibration tests with individual experimental setup. Second, they assumed that all the wear mechanisms are independent, but the wear mechanisms are closely related. This might explain the considerable discrepancy between the modeling and experimental results in both Li and Liang (2004) and Huang and Liang's work (2007).

Literature suggested that straight WC-Co has very high abrasion resistance thus adhesion and diffusion wear dominates (Upadhyaya, 1998, Pirso et al. 2006). Diffusion wear is mainly caused by the high cutting temperature, especially when the temperature is higher than 1000°C (Arsecularantne, 2006). However, the temperature is relatively low in milling because it is discontinuous cutting process and the cutting edges are able to cool down during the non-cutting half of rotation. Also, the effect of diffusion mechanism is more significant on crater wear than flank wear because the temperature on rake surface is significantly higher than that on flank surface (Stephenson and Agapior, 1997). Thus, adhesion wear is considered as the dominant wear mechanism on flank surface in this study.

Adhesion wear, is categorized as mechanical wear, which is caused from the contact between two or three material surfaces. Thus, contact mechanics based equations were the basis of the modeling of mechanical wear. Archard (1953) proposed an interpretation equation on the phenomena occurring at nominally flat surfaces in sliding contact. In his equation, the wear volume was proportional to sliding distance, contact forces and inversely proportional to hardness of the material with a coefficient K. The coefficient K is dependent on the distribution of the area contact between the surfaces. Later, several researchers extended the tool wear models based on Archard's wear equation by making different assumptions for the wear coefficient K. Shaw and Dirke (1956) extended it to adhesion wear by assuming the wear coefficient as the probability of producing a wear particle when encountered one asperity. Later, Usui and Shirakashi (1984) rewrote their models by introducing the normal stress at the contact surface. Furthermore, they assumed that the material strength and diffusion were both affected by the temperature and came out with a diffusion wear model which is similar to Trigger and Chao's work (1956). Zhao (2002) et al. applied Usui and Shirakashi's model for predicting flank wear in the case of orthogonal cutting process with internal cooling and got good results.

From the literature review, Archard's wear equation has been the basis of tool wear model for over fifty years. Based on different initial assumptions, Archard's equation has been derived for different wear mechanisms, which were summarized in Hutching's study (1992). However, most of these works were for oblique cutting process and the applications focused on turning process. Few studies worked on the prediction of tool wear in milling process; regression models based on experimental results were the main approach (Ong and Manna, 2003, Hughes et al., 2006, Ezugwu et al., 2007). In this dissertation, the wear model for milling process is developed based on Archard's equation with the assumption that adhesion wear is the main dominant mechanism.

4.3.2 Milling Tool Life Model

Tool life is always an important indicator when analyzing the tool performance. It affects the efficiency very much: every time the tool fails, the machining process needs to be stopped and the tool changing time lowers the productivity of the manufacturing process. It also affects the product quality dramatically: if machining with worn tool, the surface roughness of the product is poor and the error of the machined products might be extremely large. Therefore, tool life estimation has become an important goal especially in the machining system of a product line.

Tool life is very sensitive to several factors, such as the tool material, the machine stability, the cutting condition and the cutter geometry. Therefore, in early years, researchers used experimental approach to understand the distribution of tool life and used the distribution models for predicting tool life (Wager et al., 1971, DeVor et al., 1977, Hitomi et al., 1979). Taylor's life equation was one of the first empirical models which related the cutting velocity with tool life. The extended Taylor equation, which was expressed in terms of cutting speed, feed and depth of cut, included the most important cutting parameters with empirical constants obtained from experiments (Cook, 1973). Several studies applied either the Taylor equation or the extended Taylor equation in the milling process to model the tool life or to do cutting process optimization

(Tolouei-rad and Bidhendi, 1997, Amaitik et al., 2006, Ginting and Nouari, 2007, Pan et al, 2009).

Although Taylor tool life equation is widely used in the modeling of tool life, it actually was developed for continuous cutting process. Therefore, using Taylor's equation to estimate the milling tool life is not an appropriate approach. Experimental approach has become the main method for modeling milling tool life. In these studies, series of experiments were conducted and different techniques were applied for the model. One commonly method was using the regression analysis, such as second order equation (Sikdar et al., 1992), linear mixed effects model (Chakraborty et al., 2008) and response surface methodology (Alauddin et al., 1997). Because of the improvement of computational system, numerical method such as abductive network (Tsai et al., 2005, Lin et al., 2006) and artificial neural network (Palanisamy et al., 2008) were used. It is concluded that tool life modeling is still concentrated on the experiment-based approach. Series of experiments were required to fit the prediction equations.

4.4 Model Construction

First, the flutes of the mill are divided into numerous wedge-shaped elemental cutting tools (ECT), treating each element as though it undergoes oblique cutting independently. Each ECT experiences individual cutting condition and thus has individual flank wear. This concept has been widely accepted for the modeling of milling process.

4.4.1 Flank Wear Model

From the literature review, it is generally accepted that Archard's wear equation is the foundation model for the prediction of tool wear volume. The Archard's wear equation is shown in equation (4.1) (1953).

$$W_{ad} = \frac{KFS}{3H} \tag{4.1}$$

For each ECT, the thrust force is not constant due to the varying chip load. The average elemental thrust force in the half cutting revolution in milling process is applied as the normal load F in the equation (4.1). The cutting length S is the multiple of the distance the ECT travels during the cutting half revolution.

$$S = nS_{rev} = n\pi R_{ECT} \tag{4.2}$$

H is the hardness of the worn material, which is the tool material WC-Co. In this study, the material softening due to cutting temperature is considered. The temperature dependent hardness is applied according to the experimental result conducted by Milman et al. (1997). The cutting temperature of each ECT is calculated from the model proposed in Chapter 3. The average hardness corresponding to the transient temperature is applied to equation (4.1).

The wear coefficient K is one important parameter in Archard's wear equation, which is mostly obtained mechanistically from calibration tests for different tool and workpiece combination. Challen and Oxley (1979, 1986) proposed an analytical model for the estimation of Archard's wear coefficient. They considered the original definition of the wear coefficient, the probability that the wear particle forms when one asperity contact with a flat surface, and proposed a fatigue mechanism to estimate this "probability." They analyzed the slip-line field of the material being pushed up by asperity and used the strain of the material to solve the number of loading cycles to produce a wear particle. Sliding friction is used to calculate the magnitude of the resulting plastic strain increments which progressively deform the surface. The calculated incremental strains are used to estimate wear rates, and are expressed in terms of Archard's wear coefficient. The wear coefficient K is calculated by the following equation.

$$K = \frac{9 \times 3^{1/3} r\mu}{C^D \Delta\gamma_p{}^{1-D}} \tag{4.3}$$

The wear coefficient K is derived from the deformation energy, shear strain and a low cycle fatigue equation. With given constants C and D, K can be determined from this equation. r, μ and $\Delta\gamma_p$ can all be obtained from the slip-line field analysis as shown in Figure 4.1. $\Delta\gamma_p$ is calculated from the relative velocity between the asperity and the surface. $r\mu$ is obtained from the angle between the surface and the asperity, and the ratio between the shear strength of worn surface to the shear flow stress, k, which can be obtained from the cutting theory book (Stephenson and Agapior, 1997).

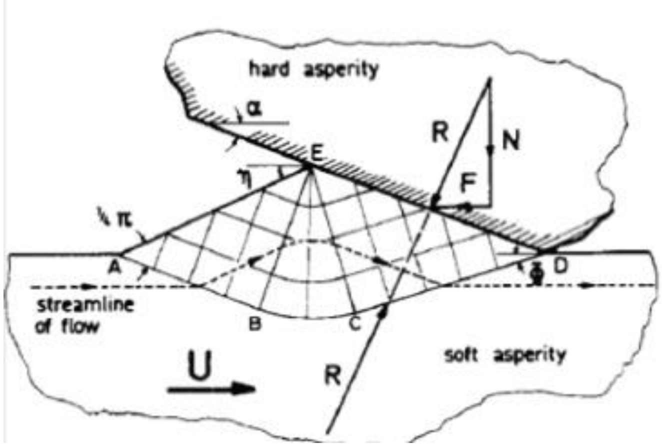

Figure 4.1: Slip-line field of the sliding friction between worn surface and wear asperity (Challen et al., 1986)

$$k = \left(\frac{F_{cut}}{t_c \times L} - \frac{F_f}{t_c' \times L} \right) \bigg/ \gamma \tag{4.4}$$

The cutting parameters of each ECT are obtained from the mechanistic force model proposed in Chapter 2. Then the worn volume W_{ad} can be calculated with Archard's wear equation.

Figure 4.2 shows the geometry of tool tip with flank wear. The dark portion is the

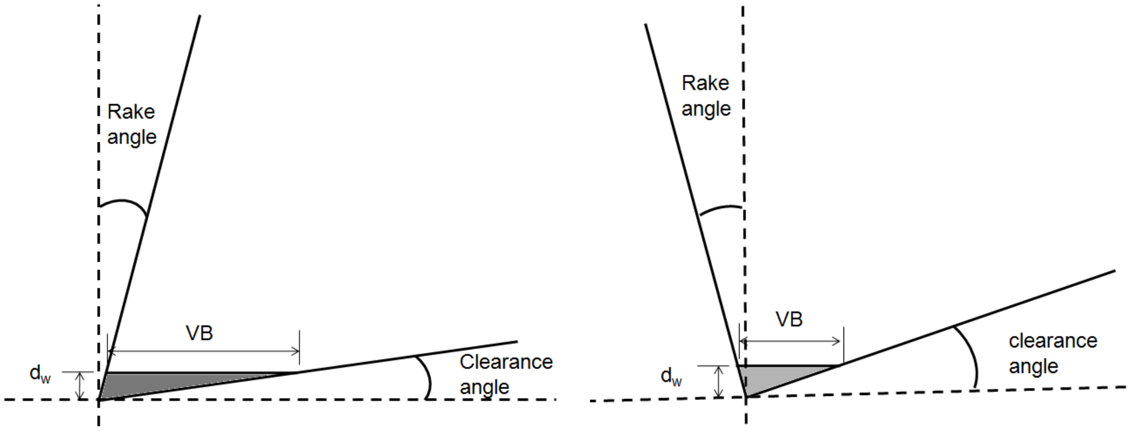
(a) **(b)**

Figure 4.2: Tool geometry of flank wear of sharp tool (a) positive rake angle (b) negative rake angle

worn volume W_{ad}, with width of the cutting edge. The geometry relationship can be derived from Figure 4.2. The average flank wear VB_e and depth of worn volume d_w can be solved by two equations, (4.5) and (4.6).

$$W_{ad} = \frac{VB_e \times d_w}{2} \times L \tag{4.5}$$

$$d_w = \left(VB_e \pm d_w \tan\alpha_n\right) \times \tan\theta \tag{4.6}$$

The addition and subtraction in equation (4.6) is determined by whether the rake angle is positive or negative. If there is flank wear existed on the tool, the tool geometry and the flank wear is shown in Figure 4.3. It is clearly seen that for both positive and negative rake angle cases, the dark portion is in a shape of trapezoid. Therefore the average flank wear VB_e and depth of worn volume d_w for both cases can be solved by equations (4.7) and (4.8).

$$W_{ad} = \left[VB_0 \times x \pm \frac{d_w{}^2 \tan\alpha_n}{2} + \frac{d_w{}^2}{2\tan\theta} \right] \times L \tag{4.7}$$

$$VB_e = VB_0 \pm d_w \tan\alpha_n + \frac{d_w}{\tan\theta} \tag{4.8}$$

Similarly to the sharp tool case, in the case of positive rake angle, it is subtraction in equations (4.7) and (4.8); vice versa.

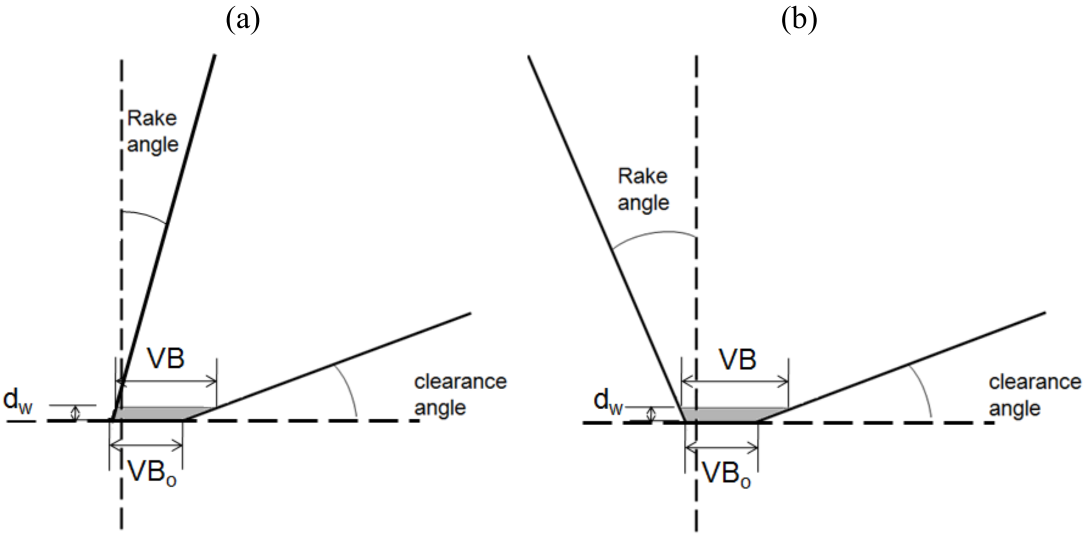

Figure 4.3: Tool geometry of flank wear of worn tool (a) positive rake angle (b) negative rake angle

4.4.2 Iteration Process

From Archard's wear model, the tool wear is strongly related to the forces. However, at the same time, the occurrence of flank wear makes the contact area between the tool and workpiece increase and results in increasing force during cutting process (Smithy et al., 2000, 2001). In this study, an iterative methodology between the flank wear and worn tool forces for the prediction of tool wear has been proposed. The study integrates the existing tool wear model and the force model of worn tools, and further applies these models in the milling process. With the use of the developed model, the tool wear progression along with cutting time can be estimated without any on-line measurement.

The flow chart of the iteration of flank wear calculation is shown in Figure 4.4. The tool is assumed to start from a new, sharp condition, and the cutting parameters and the forces of sharp tool are calculated based on Chapter 2. With the parameters as inputs, the wear coefficient and tool flank wear after cutting a certain time period can be calculated from equations in section 4.4.1.

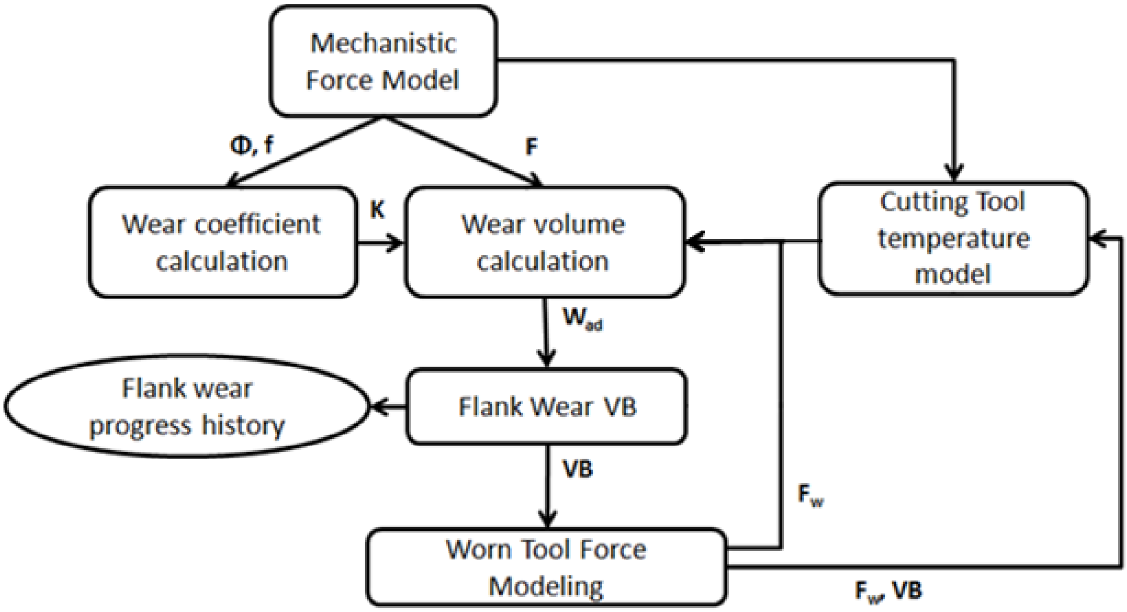

Figure 4.4: Flank wear model flow chart

After knowing the flank wear, the cutting forces of worn tool are obtained from the works in section 2.7. In short, the total forces of worn ECT can be calculated by adding the forces of sharp tool with the forces on the flank wear area.

$$d\vec{F}_w = \left|\overline{F}_{th} + \overline{F}_{tw}\right|\vec{t}_c - \left|\overline{F}_{cut} + \overline{F}_{cw}\right|\vec{V} + \left|\overline{F}_{lat}\right|\left(\vec{V} \times \vec{t}_c\right) \tag{4.9}$$

Now there is an updated thrust force on the tool which affects the wear volume calculation. So the updated thrust force is used in the Archard’s wear equations and the worn volume under that thrust force after another time period can be calculated. At the same time, the temperature model is applied for cutting tool with flank wear and thus the temperature-dependent hardness can be updated as well. Now the tool is no longer sharp, so instead of equations (4.5) and (4.6), equations (4.7) and (4.8) are used to solve the flank wear. This iteration between the flank wear and the forces of worn tool keeps going until cutting reaches the end.

Each elemental cutting tool has its own tool flank wear value VB_e. By connecting the flank wear of each ECT, the distribution of the flank wear on the cutting tool could be analyzed. Also, the maximum flank wear of all the ECTs can be used as the indication of tool life.

4.5 Validation Experiments for Tool Wear

4.5.1 Face Turning with Round Inserts

Face turning experiments were conducted for the validation of tool wear modeling. Although the face turning process has simple cutter geometry, it has different cutting conditions along the cutting edge. The measurement of tool wear on the turning insert is easier and more accurate than that on the milling tools. Therefore face turning process is used for the validation for the tool wear distribution along the cutting edge.

The experimental setup is the same as the one in the cutting force validation experiments in turning in section 2.8.1.2. Four different cutting conditions have been conducted, as shown in Table 4.1. From the table, it can be seen that the simulation results agree with experimental results. However, the simulation results under-predicted the tool wear. The discrepancy might be due to difference between the tool material used for force calibration (WC-10%Co) and the material of the turning inserts (WC-6%Co). In the force validation experiments in section 2.8.1.2, the forces are underestimated. Thus, it is reasonable that the tool wear is also underestimated in the modeling results due to the smaller forces.

Table 4.1: The experimental and modeling results under different cutting conditions

Cutting Condition			Experimental	Model
Feed Rate (m/min)	SFM	DOC (mm)	Flank Wear(mm)	Flank Wear(mm)
0.127	250	0.127	0.047	0.0406
0.127	350	0.127	0.066	0.0424
0.381	250	0.381	0.23	0.2266
0.127	350	0.381	0.11	0.1069

The distribution of the flank wear on the inserts was observed and compared with the modeling results in Figure 4.5. It is clearly seen that the modeling distribution actually matched up with the experimental results quite well. The predicted maximum flank wear position corresponded to the experimental observation picture. Also, the slightly increasing portion and dramatically decreasing portion were captured in the modeling results.

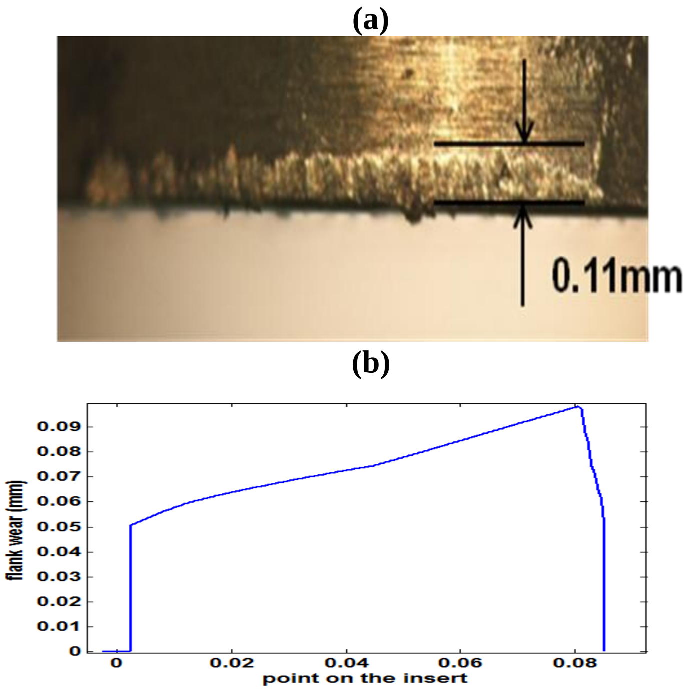

Figure 4.5 Comparison of the flank wear distribution (a) observation from experiment and (b) modeling results

4.5.2 Slot Milling with Ball-end Mill

A series of validation experiments were also done to verify the tool wear progression and the corresponding forces with tool wear. The tests were conducted as the same experimental setup in section 2.8.1.1. Two different cutting conditions have been tested and the parameters are shown in Table 4.2. For each test condition, three experiments were done to verify the repeatability under the same cutting condition.

Table 4.2: Validation experimental conditions

Test condition number	Spindle speed (rpm)	Feed (m/min)	Axial depth of cut (mm)
1	3000	1.27	1.27
2	3500	0.64	2.54

A new tool was used to repeat cutting full slots of 14.2 cm in length. The forces during the whole cutting process were recorded, and compared with the modeling results as several time intervals. The flank wear was measured with the use of PG-1000 at each time interval.

Figure 4.6 shows the experimental and modeling results of both flank wear and cutting forces in a total 303 seconds of cutting time of the first test. The average flank wear of the four flutes reaches 0.1728 mm in experiments after cutting 303 seconds; while the modeling flank wear is about 0.18 mm for all the flutes. The discrepancy between the flutes might be due to the assumption of no tool run-out and deflection in the model. However, the average flank wear of the four flutes match up with the modeling results very well. Figure 4.6 (b) to (f) show the cyclic cutting forces of experimental and modeling results of the first test at each point right before the flank wear is measured, which is approximately after cutting 60, 120, 180, 240 and 300 seconds. The model estimates the increasing forces very well.

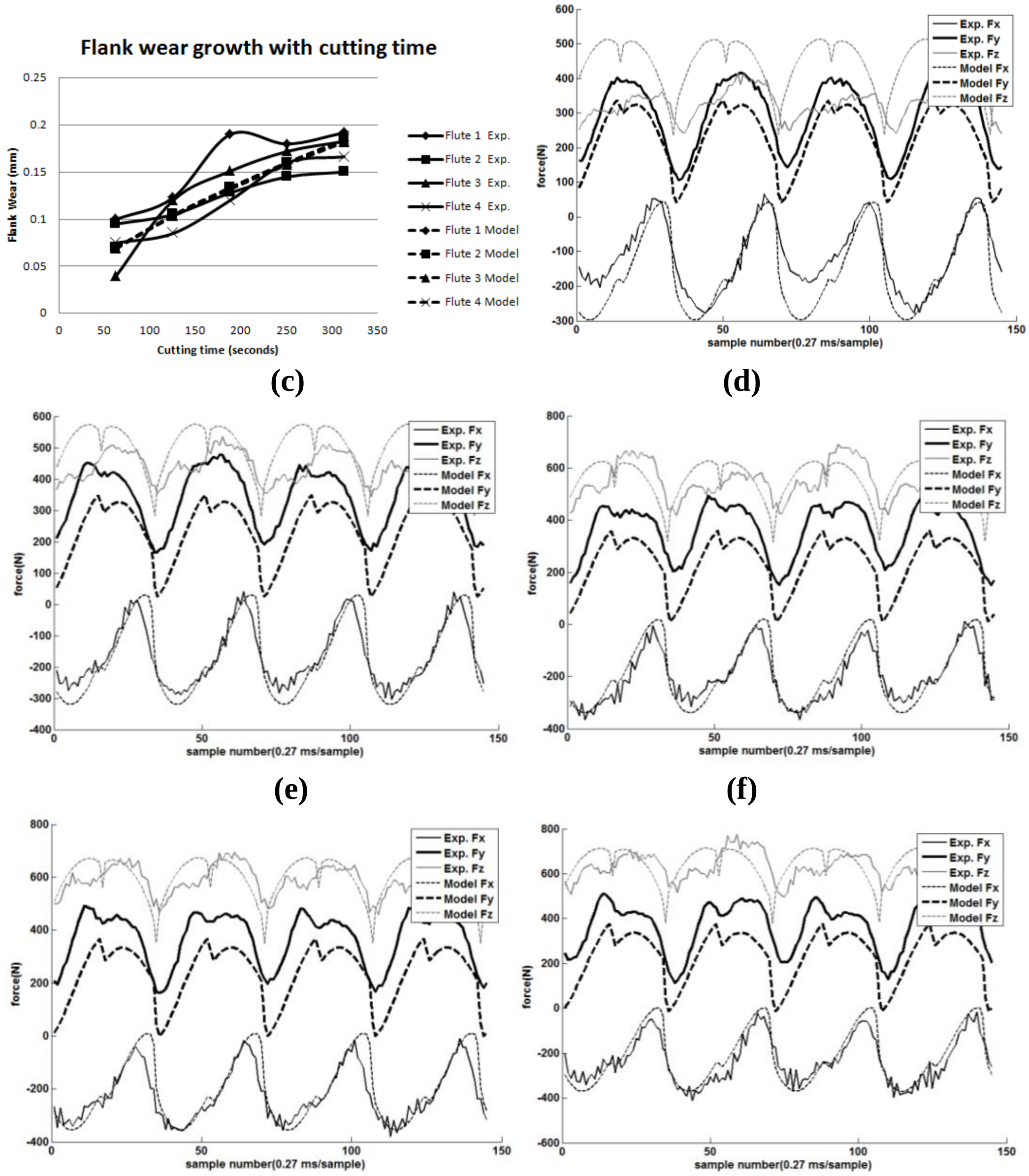
(a) (b) (c) (d) (e) (f)

Figure 4.6: Experimental and modeling result of the 1st test (a) flank wear (b) cutting force after 60 seconds (c) 120 seconds (d) 180 seconds (e) 240 seconds (f) 300 seconds

Figure 4.7(a) shows the flank wear from both experiment and model in 487 seconds of cutting time of the second test. The modeling result after cutting 487 seconds is 0.102 mm as the average of four flutes and the average flank wear in the experiment is 0.129 mm. The model slightly underestimates the flank wear. This might be due to the tool run-out. The run-out makes two flutes wear faster than the other two, which can be observed that the tool wear of the four flutes separate into two separate groups. Tool run-out also leads to larger forces, and even more tool wear during the cutting process. Figure 4.7(b) to (f) show the cyclic forces of the second test at every 97 seconds of cut. Conclusions similar to Figure 4.6 can be drawn. A little more discrepancy can be observed in this cutting test due to the instability problems caused by the larger depth of cut. In general, the modeling results match up with the experimental results very well.

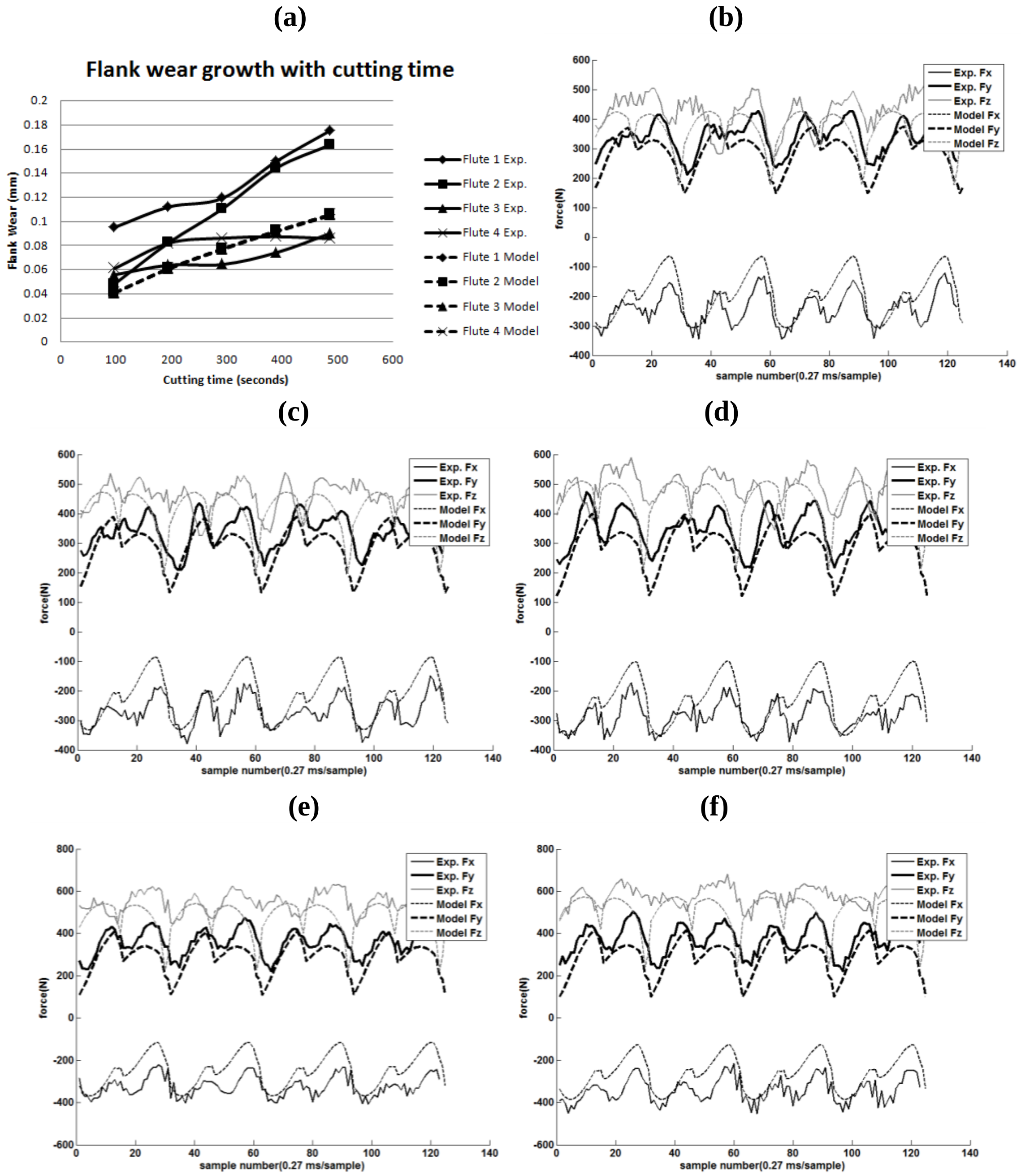

Figure 4.7: Experimental and modeling result of the 2nd test (a) flank wear (b) cutting force after 97 seconds (c) 194 seconds (d) 291 seconds (e) 388 seconds (f) 485 seconds

4.6 Estimation of Tool Life

Flank wear is a commonly used indicator for determining tool life. Based on the required quality of the product, the criterion of flank wear is set. When the tool flank wear reaches the criterion, the tool is determined to be failed and needs to be replaced by a new tool to finish the machining works. In this study, the tool wear progression along with the cutting time is estimated. Therefore, with a given flank wear criterion, the model is able to estimate the total cutting time before the tool reaches failure criterion. A series of tool failure experiments have been conducted to compare with the modeling result. The experimental setup is the same as the one in section 2.8.1.1. The cutting conditions are listed in Table 4.3.

Table 4.3: The cutting conditions of tool failure experiments

Test condition number	Spindle speed (rpm)	Feed (m/min)	Axial depth of cut (mm)
1	3500	2.54	2.54
2	3500	1.27	2.54
3	3500	0.64	2.54
4	3500	2.54	2.03
5	3500	2.54	1.27

For all the tests, the tool starts cutting from a new sharp condition, and keeps cutting full slots of 14.2 cm in length. The tool wear on all four flutes is measured every ten slots of cut. If any one of the flutes has flank wear larger than the criterion, the tool is determined as failed. The tool wear criterion in this study is set to be 0.3mm, which is suggested from industry practice. In the model, the calculation iteration is every 10 seconds and the iteration stops whenever the tool wear reaches 0.3mm.

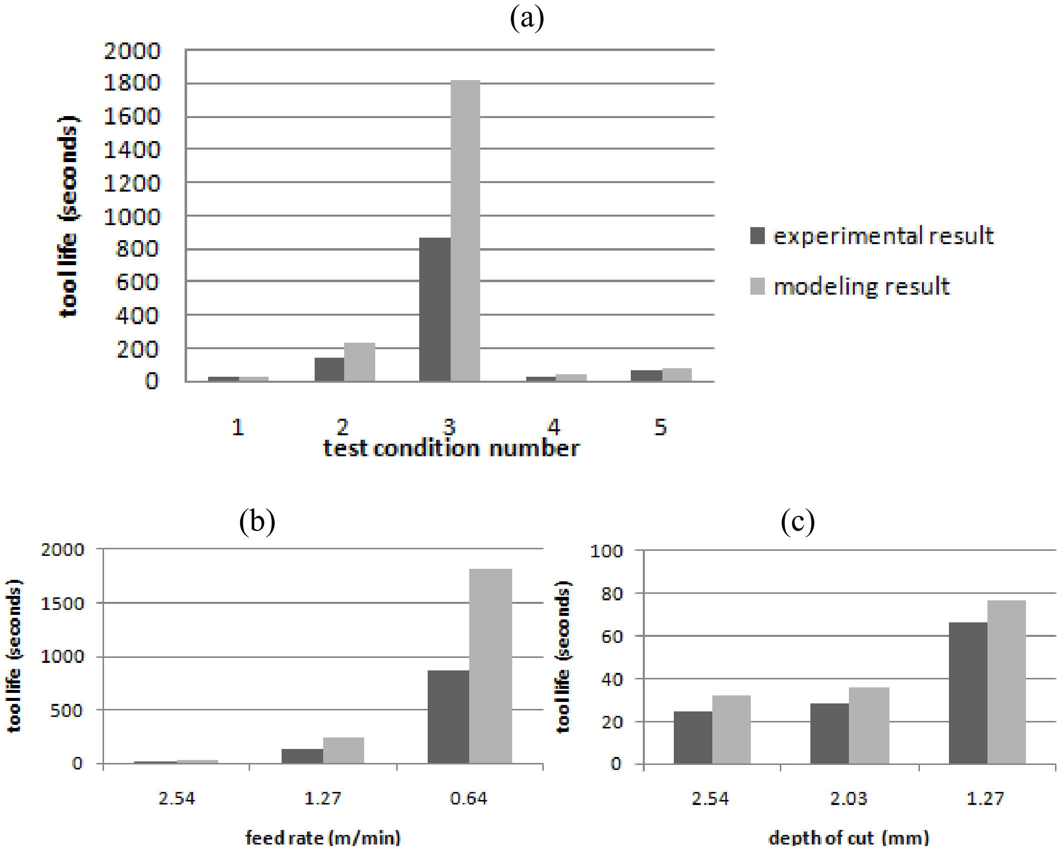

Figure 4.8 Experimental and modeling result of the tool life validation (a) all cutting condition (b) spindle speed 3500 rpm, depth of cut 2.54 mm with different feed rate (c) spindle speed 3500 rpm, feed rate 2.54 m/min with different feed rate

Figure 4.8 shows the comparison of tool life from experimental and modeling results. In Figure 4.8 (a), all the different cutting conditions have been compared and it is clearly seen that the modeling result overestimated in most cases slightly; while only case number three has huge discrepancy. The discrepancy between the experimental and modeling results might be due to several reasons. First of all, from the tool wear validation tests in section 4.5.2, the model slightly underestimates the experimental wear progression. Thus the tool life will be overestimated with the cumulative error. Second, from the observation of tool wear progression in section 4.5.2, the flank wear progression on four flutes is not consistent. Tool run-out causes the discrepancy of the four flutes while the modeling result shows the same amount of wear on all of them. For the tool life experiments, whenever one of the four flutes reaches the flank wear criterion, the tool is determined to be failed. Thus, it is very likely that the experimental tool life is shorter than the modeling result. The effect of tool run-out on uneven wear in four flutes is obvious in Figure 4.7(a), which has the same cutting condition as case number three in the tool life validation experiments. The fastest worn flute in Figure 4.7 (a) already has 0.17mm wear while the modeling wear is only 0.11 mm. If we simply assume a linear wear increasing along with time from Figure 4.7 (a), the fastest worn flute will reach flank wear criterion after cutting 869 seconds and the modeled flank wear will reach the criterion after cutting 1766 seconds. The number is very closed to the discrepancy of case number three in the tool life validation experiments. Thus, it is reasonable to conclude that if considering the tool run-out effect in the model, or after eliminating the run-out in the experimental setup, this model is able to estimate tool life very well.

Moreover, the comparison between different feed rate and depth of cut is shown in Figure 4.8 (b) and (c). In Figure 4.8 (b), tests 1, 2 and 3, which have same spindle speed and depth of cut but varying feed rate, are plotted. The higher feed rate results in larger cutting force on the tool and thus leads to shorter tool life. In Figure 4.8 (c), the tests with same spindle speed and feed rate but varying depth of cut are compared. For the larger depth of cut, the tool experiences larger total cutting force as well. Also, with the larger depth of cut, the tool also experiences higher cutting speed and cutting temperature. Therefore, the tool life of test 5 should be slightly longer than test 1 and test 4. By comparing Figure 4.8 (b) and (c), it is clearly seen that the tool life is influenced by the feed rate more significantly than the depth of cut. It agrees with common machining application that the feed rate is always the most important parameters to be adjusted.

4.7 Summary

In this study, an iterative methodology between the wear and the forces for the estimation of tool wear is proposed The study integrates the existing tool wear model and the force model of worn tools, and further applies these models in the milling process. The cutting forces during the milling processes result in tool wear, and at the same time, the tool wear increases the cutting forces. Therefore, by continuing the iteration between the flank wear and the forces of the worn tool, flank wear can be estimated without on-line measurement. The material softening is also included by applying temperature dependent hardness. Validation experiments have been conducted. A sharp tool was used to cut full slots until it is worn, and the forces were recorded during the cutting processes. Tool flank wear was also measured every time interval. The good agreement between the experimental and modeling results for both the tool wear and the forces of worn tool suggests that the model works well to estimate the flank wear. Finally, the model is used for predicting tool life with given flank wear criterion. Several cutting conditions have been tested experimentally and compared with the modeling result. The model shows geed agreement with different cutting conditions and thus can be a good insight of evaluating tool performance for higher machining efficiency.

CHAPTER 5

AN ANALYTICAL MODEL FOR STRESS DISTRIBUTION CALCULATION

5.1 Nomenclature

E	Young's modulus of the tool material
F_n	normal force on rake surface of ECT
l_c	tool-chip contact length
m	total number of elements on flank surface
n	total number of elements on rake surface
p_0	stress at the tool tip on rake surface
p^F	prescribed normal stress on flank surface
p^R	prescribed normal stress on rake surface
p'^F	real normal loads on rake surface
p'^R	real shear loads on rake surface
q^F	prescribed shear stress on flank surface
q^R	prescribed shear stress on rake surface
q'^F	real shear loads on flank surface
q'^R	real shear loads on rake surface

T_0	room temperature
α	thermal expansion coefficient of tool material
θ	angle between the rake and flank coordinate
μ	friction coefficient between the tool and chip
ν	Poisson's ratio of tool material
σ^F	resultant normal load on flank surface from real loads on rake
σ^R	resultant normal load on rake surface from real loads on flank
σ_{therm}^F	thermal stress in the normal direction flank surface
σ_{therm}^R	thermal stress in the normal direction on rake surface
τ^F	resultant shear load on flank surface from real loads on rake
τ^R	resultant shear load on rake surface from real loads on flank
τ_{therm}^F	thermal stress in the shear direction on flank surface
τ_{therm}^R	thermal stress in the shear direction on rake surface

5.2 Introduction

The gradually increasing tool wear is considered as the main mechanism which leads to tool failure. However, sometimes tool fails unexpectedly during the machining process. One of the most common reasons that lead to unexpected tool failure is edge chipping, which has been observed frequently in the milling of titanium alloys (Ginting and Nouari, 2002, A.K.M. Nurul Amin et al., 2007). Edge chipping happens due to the excessive stress in the tool, and the excessive stress is expected in the milling of titanium alloys.

The stress in the tool has two main components: the mechanical stress resulting from the cutting force, and the thermal stress resulting from the cutting temperature. In the milling of titanium alloys, the cutting force is large due to the high strength of the material; at the same time, the cutting temperature is also high due to the low thermal conductivity of the material. Moreover, the load-unload and heat-cooling cycle in the milling process result in not only the excessive stress but also fatigue damage in the tool.

In this chapter, based on the previous modeling technique of cutting force and temperature, the stress in the tool has been calculated and analyzed. Mechanical stress and thermal stress are combined using boundary element method. The stress distribution in the milling tool is examined with a brittle fracture analysis to evaluate the tool design. Stress concentration points in a tool design have been identified and edge chipping at those points in the real cutting tests has been observed.

5.3 Literature Review

The stress of the tool has been observed and studied for a long time. Since the stress loading is directly applied on the surfaces of the tool, early studies focused on understanding the contact conditions on the tool-chip interface. Like all the studies related to machining, people started to investigate the stresses from experimental approach. A variety of experimental techniques have been applied for analysis of the tool stress distribution along the tool-chip contact zone. Photoelastic tools were used for observing the stress distribution (Usui and Takerama, 1960, Bagchi and Wright, 1987). However, divergent results were observed and it was believed that when using this approach, the results varied based on the cutting conditions and the workpiece materials

(Arsecularatne, 1996). Split-tool dynamometer method was used to obtain the stress distribution with more aggressive cutting conditions and different tool materials, comparing to the photoelastic method. The split-tool method used a composite tool divided into two parts, and measured the forces on each of the part then calculated the stresses from the force data (Kato et al., 1972, Barrow et al., 1982, Buryta et al., 1994). Figure 5.1 shows the divergent results from experimental approach. From the figure, it can be concluded in general that the normal stress is exponentially decreased from the tool tip to the tool-chip contact length. The shear strength has a stick-slip zone which separates about half of the contact length.

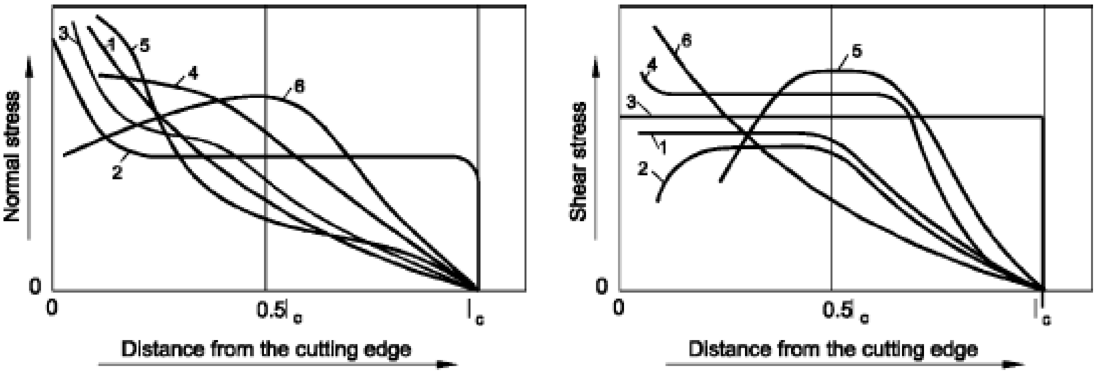

Figure 5.1 Stress distributions in literature (Atakhov and Outeiro, 2005)

Later, researchers combined the knowledge of cutting forces and the stress distribution on the rake face to analyze the stress inside of the tool. In early years, analytical method for analyzing the tool stress was studied. Archibald (1956) analyzed the stress in the tool by assuming a linearly decreasing normal stress and a corresponding shear stress on the rake face of the tool. A polar coordinate system and the series solution approach were used to solve the stress problem. Chandrasekaran and Nagarajan (1980) started from the stress inside an elastic edge under a single concentration load at the apex, and applied the time-dependent loading condition in the milling process. At the same time, researchers started to address on the importance of thermal stress, especially in intermittent cutting such as milling. Several temperature models and the thermal stress calculations on the cutting tools have been analyzed together using analytical method (Bhatia et al., 1980, Uehara, 1981, Chakraverti et al., 1984).

Finite element method became the dominant technique for analyzing the machining problem after the computational system improves dramatically from 1990 (Chandrasekaran, 1991, Zhou et al., 1994, Monaghan and MacGinley, 1999, Astakhov and Outeiro, 2005). However, finite element method is extremely sensitive to the parameters chosen in the model, such as mesh size, and it requires precise material properties to obtain good results. Moreover, the model needs to be reconstructed whenever the geometry is changed, which means, for each ECT on the milling tool, it requires a new FEM model for analysis. Thus, a more time efficient and robust model is necessary for analyzing the stress on the complicated milling tool.

5.4 Stress Calculation in the Tool

The whole cutting edge of the milling tool has been discretized into several ECTs as well in the stress calculation. During the milling process, the total loads the ECT experienced is the elemental cutting forces. On the rake surface, there are the friction force F_f and the normal force F_n; while on the flank surface, there are also the friction force F_{cw} and the normal force F_{tw}, as modeled in Chapter 2. This total loads are actually contributed by the thermal stress and the "real" mechanical stress loaded on the boundary. Boundary element method is used to determine the "real" mechanical stress on both the rake and flank surfaces. Finally, the stress in the tool is the summation of the thermal and mechanical stresses from the "real" loads at the tool surfaces.

5.4.1 Model Development Approaches

First, elastic half-space case with line loading was assumed for the mechanical loading on the tool surface. A state of plane strain is produced in the half-space due to line loading. However, the wedge-shaped ECT made the assumption of half-space unrealistic. In order to apply the calculation of line loading in elastic-half space on the wedge-shaped tool, it is assumed that on the other side of the wedge, there is another boundary which experiences the resultant stress and has its own loading condition at the surface.

The problem can be decomposed into two loading problems, one on the rake surface and the other on the flank surface. If some normal and shear stresses are applied on the rake surface, there will be resultant normal and shear stresses on the flank surface; vice versa. Therefore on each surface, there will be some real applied stresses, the resultant stresses from the loading on the other surface, and the thermal stress due to temperature rise. The summation of them will equal to the prescribed stress distribution on the surfaces as shown in Figure 5.1. Now the stress distribution becomes the boundary conditions and the real applied loads are the unknowns. Boundary element method (BEM) is used to solve the real applied loads on both rake and flank surfaces.

With the use of BEM, the surfaces need to be discretized into numerous elements. It is assumed that each element is under uniform normal and shear stresses. The stresses on the mid-point of the element will be used as the uniform load on the element. Figure 5.2 shows the stress distribution on the rake surface, p_i^R and τ_i^R, and the real loads p'^R_i, q'^R_i. It also shows how coordinate rotates when transforming the resultant stress from rake surface to the flank coordinates. The subscript i means the piecewise stress at the i^{th} element on rake surface. The superscripts R and F show that the stresses are in either the rake or flank coordinate.

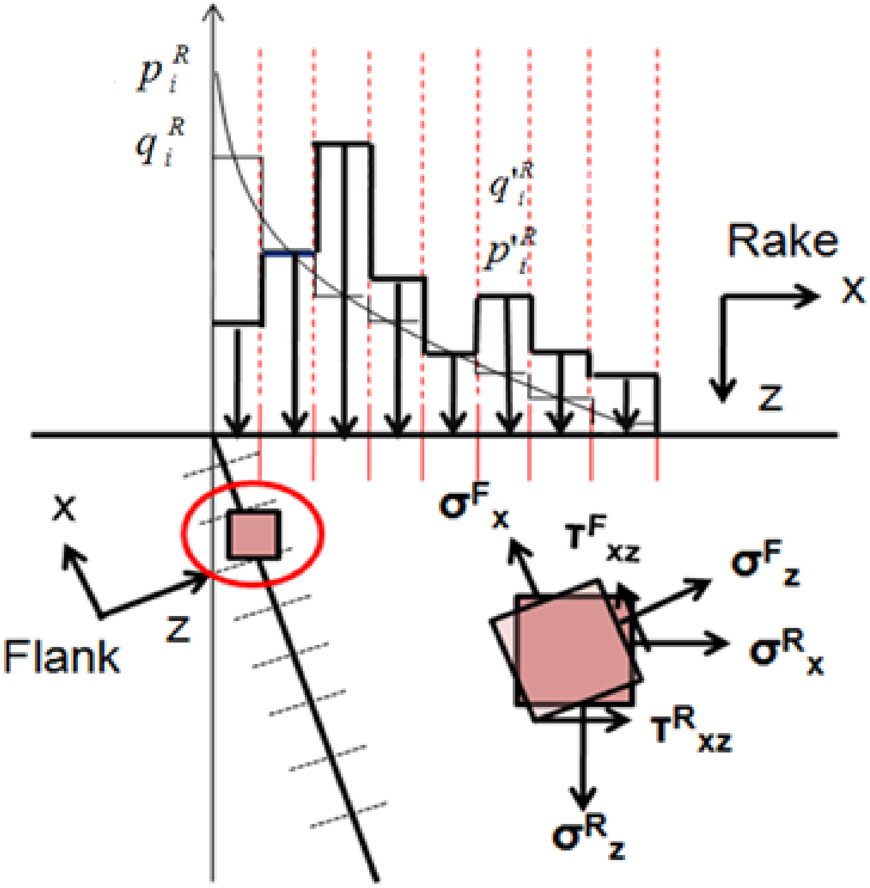

Figure 5.2 Rake surface loading and coordinate transformation

From Johnson's book (1987), the stresses of arbitrary point in the half-space body under uniform pressure p and tangential traction q are listed from equation (5.1) to (5.3). The coordinate of the half-space body and the stress loading are shown in Figure 5.3.

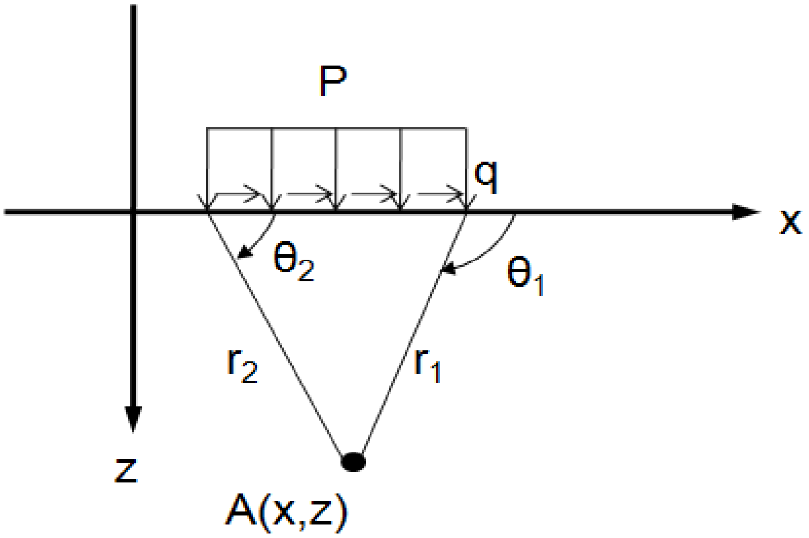

Figure 5.3 Half-space body with uniform normal and tangential stress (Johnson, 1987)

$$\sigma_x = -\frac{p}{2\pi}\{2(\theta_1-\theta_2)+(\sin 2\theta_1 - \sin 2\theta_2)\} - \frac{q}{2\pi}\left\{4\ln\left({r_1}/{r_2}\right)-(\cos 2\theta_1 - \cos 2\theta_2)\right\} \tag{5.1}$$

$$\sigma_z = -\frac{p}{2\pi}\{2(\theta_1-\theta_2)-(\sin 2\theta_1 - \sin 2\theta_2)\} + \frac{q}{2\pi}(\cos 2\theta_1 - \cos 2\theta_2) \tag{5.2}$$

$$\tau_{xz} = \frac{p}{2\pi}(\cos 2\theta_1 - \cos 2\theta_2) - \frac{q}{2\pi}\{2(\theta_1-\theta_2)+(\sin 2\theta_1 - \sin 2\theta_2)\} \tag{5.3}$$

Using coordinate transformation, the resultant stresses on the flank surface can be calculated.

$$\sigma_x^F = \frac{\sigma_x^R + \sigma_z^R}{2} + \frac{\sigma_x^R - \sigma_z^R}{2} \cos 2\theta + \tau_{xz}^R \sin 2\theta \tag{5.4}$$

$$\sigma_z^F = \frac{\sigma_x^R + \sigma_z^R}{2} + \frac{\sigma_x^R - \sigma_z^R}{2} \cos 2\theta - \tau_{xz}^R \sin 2\theta \tag{5.5}$$

$$\tau_{xz}^F = \frac{\sigma_x^R - \sigma_z^R}{2} \sin 2\theta + \tau_{xz}^R \cos 2\theta \tag{5.6}$$

For each element on the flank surface, it will experience stresses resulted from all elemental loads on the rake surfaces. Therefore, the resultant stress on one element on the flank surface is the summation of the resultant stresses from all elemental loading on rake.

$$\sigma_{x\ j}^F = \sum_{i=1}^{n} \left(A_{ji} p'^R_i + B_{ji} q'^R_i \right) \tag{5.7}$$

$$\tau_{xz\,j}^F = \sum_{i=1}^{n} \left(C_{ji} p'^R_j + D_{ji} q'^R_j \right) \tag{5.8}$$

$A_{ji}, B_{ji}, C_{ji}, D_{ji}$ are the coefficients after substituting equations (5.4),(5.5),(5.6) into equations (5.1) and (5.3). The total stresses on one of the element on the flank surface include the resultant stresses from rake, the real load on flank, and the thermal stress.

$$p_j^F = \sum_{i=1}^{n} \left(A_{ji} p'^R_i + B_{ji} q'^R_i \right) + p'^F_j + \sigma_{therm}^F \tag{5.9}$$

$$q_j^F = \sum_{i=1}^{n} \left(A_{ji} p'^R_i + B_{ji} q'^R_i \right) + q'^F_j + \tau_{therm}^F \tag{5.10}$$

The same derivation process can be performed on the rake surface, as shown in equations (5.11) and (5.12).

$$p_i^R = \sum_{j=1}^{m}\left(E_{ij}\, p'^{F}_{j} + F_{ij}\, q'^{F}_{j}\right) + p'^{R}_{i} + \sigma^{R}_{therm} \tag{5.11}$$

$$q_i^R = \sum_{j=1}^{m}\left(G_{ij}\, p'^{F}_{j} + H_{ij}\, q'^{F}_{j}\right) + q'^{R}_{i} + \tau^{R}_{therm}\tau \tag{5.12}$$

From equations (5.9) to (5.12), there are $2(n+m)$ equations and $2(n+m)$ unknowns. Thus the real loads $p'^{R}_{i}, q'^{R}_{i}, p'^{F}_{j}, q'^{F}_{j}$ can be solved from all the linear equations.

After knowing the real loads on the rake and flank surfaces, the mechanical stress results from the real load at any point in the tool can be calculated from equations (5.1) to (5.3). The thermal stress calculation will be explained in section 5.4.3. The total stress at any point in the tool is the summation of both mechanical and thermal stresses. The total stress matrix is a three-dimensional Cauchy stress tensor. The three principal stresses of each ECT can be calculated. The maximum of these three principal stresses, which is a tensile stress, is considered as the main indicator to evaluate the tool because the WC-Co is a brittle material which has lower tensile strength.

5.4.2 Stress Distribution on the Tool Boundary

The loads on the boundary are calculated from the forces, which can be determined from the mechanistic force model. It is generally accepted that the normal stress exponentially decreases from the tip and becomes zero at the tool-chip contact length l_c, and the shear stress has a stick-slip zone. The stress on the flank surface is based on the model introduced in section 2.7. The total stress loads for both rake and flank surfaces are illustrated in Figure 5.4.

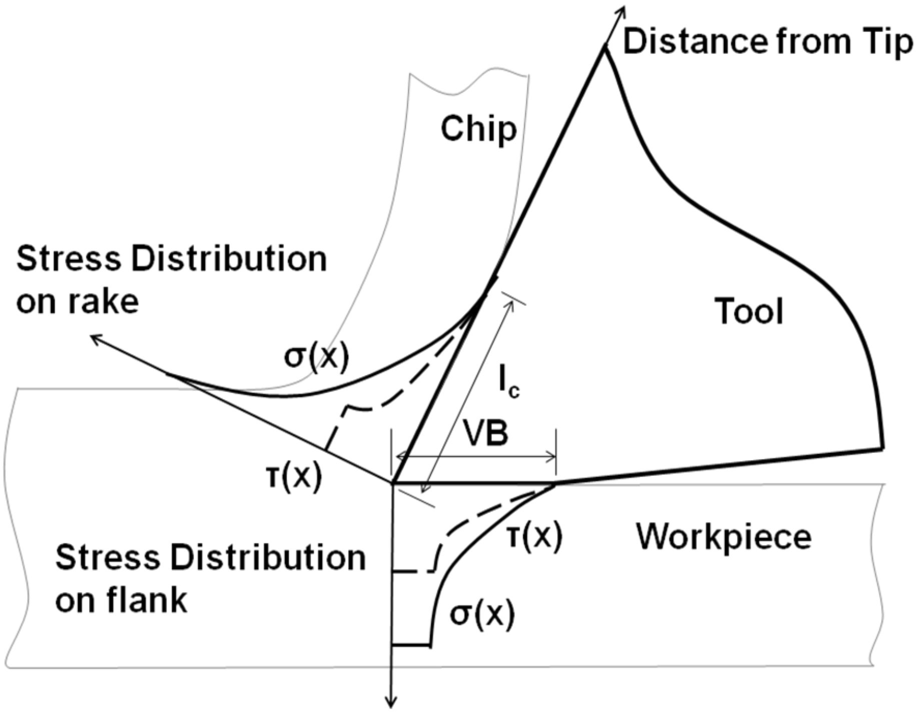

Figure 5.4 Stress distribution on the tool surfaces

Accordingly, the normal and shear stress distribution on the rake surface can be modeled from the following equations.

$$p^R(x) = p_o^R\left(1 - \frac{x}{l_c}\right)^2 \tag{5.13}$$

$$q^R(x) = q_0^R, \quad \text{if } x < \frac{l_c}{2}, \tag{5.14}$$

$$\text{and } q^R(x) = \mu p^R(x), \quad \text{if } x > \frac{l_c}{2}. \tag{5.15}$$

x is the distance from the tool tip, and μ is the friction coefficient. The normal stress is resulted from the normal force acting on the rake surface.

$$F_n = \int_0^{l_c} p_0^R \left(1 - \frac{x}{l_c}\right)^2 dx \tag{5.16}$$

Since F_n is known, max stress p_0^R can be obtained. The shear stress is resulted from the friction force acting on the rake surface. The stress q_0^R can be obtained by equation (5.17) as well.

$$F_f = l_c q_0^R + \int_0^{l_c} p_0^R \left(1 - \frac{x}{l_c}\right)^2 dx \tag{5.17}$$

When the tool is sharp, it is assumed the tool is not contacting with the workpiece surface on the flank surface. So the prescribed normal and shear stresses at the flank surface is zero. When the tool is worn, the normal and shear stresses on the tool flank surface is based on the study of Smithy et al.(2000, 2001), and the equations are listed as equation (2.35) to (2.38).

5.4.3 Calculation of Thermal Stress

The temperature change during the cutting process causes the tool to expand or contract. The expansion and contraction are constrained by the chip and the workpiece thus the thermal stress is created. Therefore, the thermal stress is not caused simply by the temperature change of the material itself but due to the contact with nearby environment.

In this study, the thermal stress calculation is different when the point is on the boundary or inside of the tool. It is assumed that the tool is not deformed so the points on the boundaries are fully constrained in the normal direction. Thus the stresses in the normal direction on rake and flank surfaces are calculated from equation (5.18).

$$\sigma_i = \frac{E\alpha}{(1-\nu)}(T_i - T_0) \tag{5.18}$$

The stress in the shear direction on the boundaries is from the friction between the tool and the chip or workpiece caused by expansion.

$$\tau_i = \mu\sigma_i \tag{5.19}$$

The normal and shear stresses on the boundary are used for the real load calculation in section 5.4.2.

For the points inside the tool, the stress is assumed always in the normal direction, so there is no shear stress. The stress inside of the tool is caused by the contractions or expansions from the nearby points. Thus, the temperature difference between the nearby points result in the stress at the interested point.

The stresses in either the x direction or z direction, as the coordinate shown in Figure 5.2, are calculated based on the nearby points' temperature.

$$\tau_i = \frac{E\alpha}{(1-\nu)}\left[(T_{i+1} - T_i) - (T_i - T_{i-1})\right] \tag{5.20}$$

For x stress, T_{i-1} and T_{i+1} are the temperatures at the points nearby in the x direction; similarly, for z stress, the temperatures are at the points nearby in the z direction.

5.5 Modeling Results

The model is calculated based on the cutter geometry same as the previous chapters. The cutting force data is from Chapter 2, and the cutting temperature is from Chapter 3. The cutting condition of spindle speed 3500 rpm, feed rate 2.54 m/min, the depth of cut 2.54 mm is used in the following modeling results. The stress in the milling process is varying all the time. There is cyclic stress loading in the tool revolution, and the tool stress is also different when the tool has different flank wear. The following modeling results show the cyclic stress and stress distribution in both sharp tool and worn tool with 0.3 mm flank wear.

5.5.1 Stress of Sharp tool

Figure 5.5 plots the stress distribution in the ECT when it starts engaging in cutting and when it is at the end-of-cut in one cutting cycle. At the beginning-of-cut, the tool-chip contact length is short, and the cutting temperature is still low. The maximum stress locates on the rake surface at 0.01 mm distance from the ECT tip. After the cutting cycle, the tool experiences a variant tool-chip contact length with changing stress and heat flux. The complicated heating and loading cycles result in two local maximum stress points on the rake surface. The local maximum which is further from the ECT tip is resulted from the thermal stress due to the heating and cooling in the process. The other one is due to the concentrated force at the small tool-chip contact zone at end of cut, which is at the same position as the beginning-of-cut. The average stress on the rake surface is high at the end of cut than at the beginning-of-cut due to the increasing temperature in the cutting cycle.

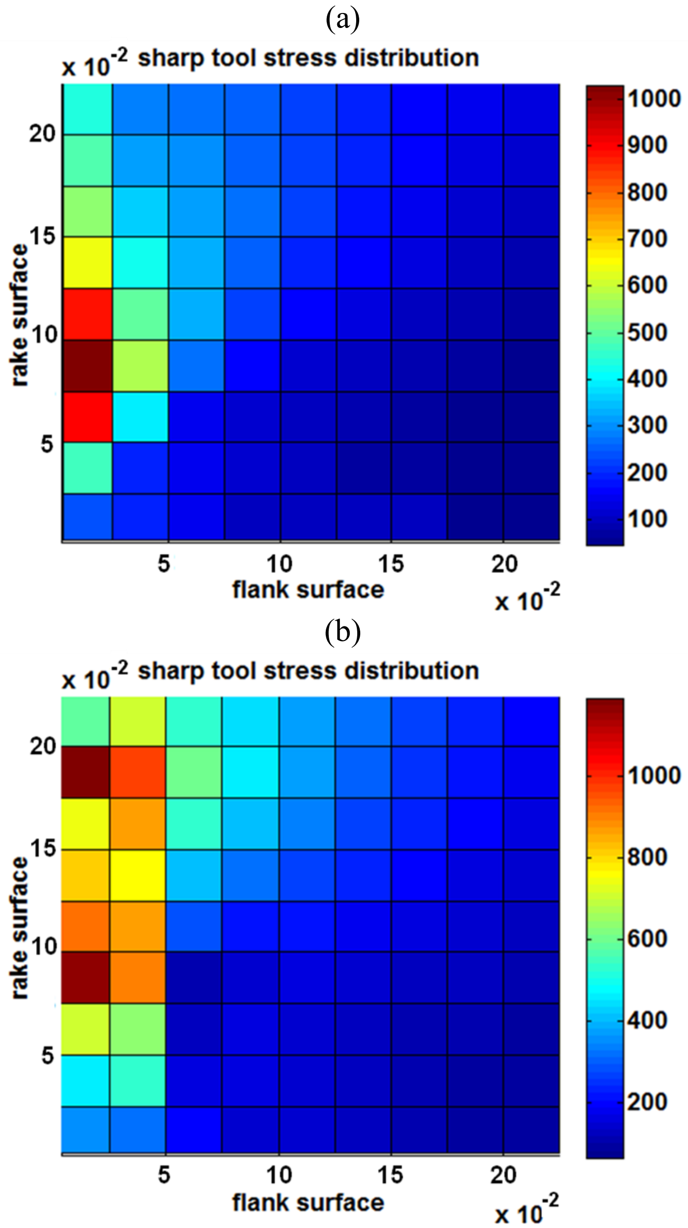

Figure 5.5 Stress distribution of sharp tool when at (a) the beginning-of-cut cycle (b) the end-of-cut cycle

Figure 5.6(a) and (b) show the cyclic load at the two stress peaks location on the rake in Figure 5.5. At both points, there is a stress peak near the beginning-of-cycle and another peak at the end-of-cut cycle. In Figure 5.6(a), the stress is high at the beginning-of-cut because that point is already in the tool-chip contact zone and experience the high mechanical stress due to the forces. The chip load is increasing at the beginning-of-cut cycle, thus the tool-chip contact area where the forces applied increases so the stress decreases. In the end-of-cut, the chip load decreases so the stress increases. At the same time, the increasing cutting temperature results in thermal stress and contributes to large total stress. Similar trend is observed in Figure 5.6(b), at the point which is 0.02 mm from the tool tip. The only difference is that this point experiences mechanical loads later than the point in (a) so the first peak comes after it is inside the tool-chip contact area.

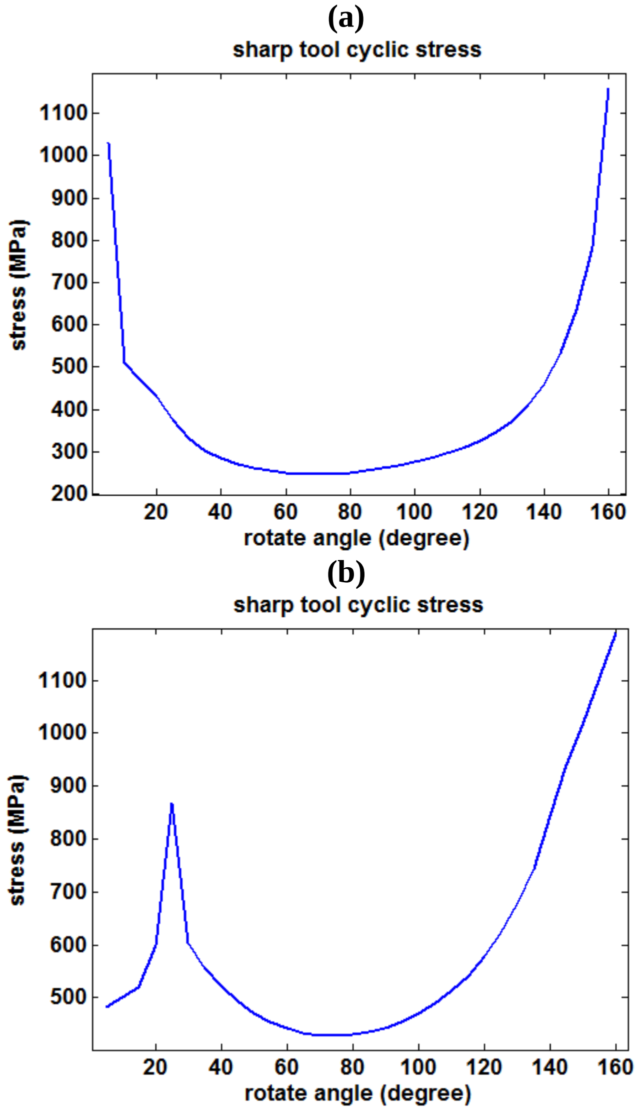

Figure 5.6 Cyclic stress of sharp tool at (a) 0.01 mm (b) 0.2 mm from the ECT tip

5.5.2 Stress of Worn Tool with 0.3 mm Flank Wear

When there is flank wear on the ECT, the flank surface is also under the mechanical loads and experiences heat flux. Figure 5.7 shows the stress distribution in the ECT with flank wear 0.3 mm.

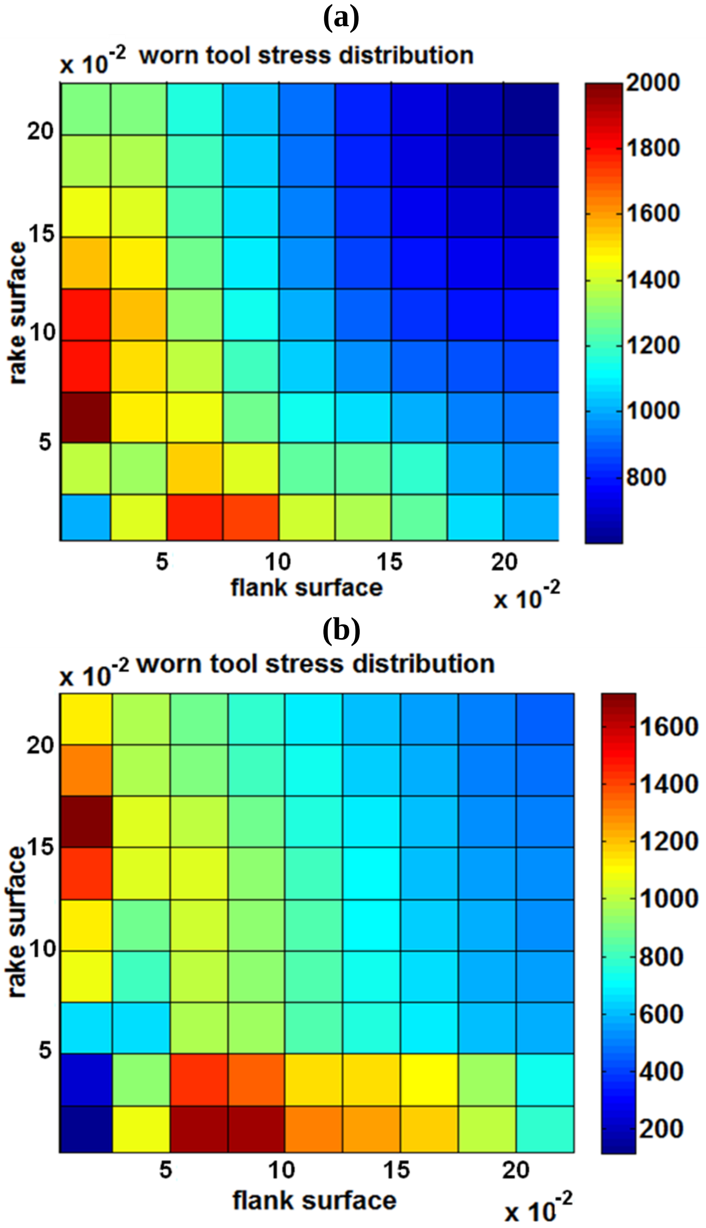

Figure 5.7 Stress distribution of worn tool when at (a) the beginning-of-cut cycle (b) the end-of-cut cycle

At the beginning-of-cut, as shown in Figure 5.7(a), one local maximum stress locates on the rake surface and another one locates on the flank surface. The local maximum locates closer to the tool tip than under the same condition in the sharp tool in Figure 5.5(a). This is because the extra loading on the flank surface makes the stress more concentrated near the tool tip. Similarly, the local maximum on the rake surface locates slightly closer to the tool tip after cut, as shown in Figure 5.7(b). The location of the local maximum on the flank surface does not change in the cutting cycle because the tool flank wear is assumed to be constant due to the short cutting time in a cycle.

Figure 5.8 shows the cyclic stress in the worn tool at the location of local maximums on both rake and flank surfaces. Figure 5.8(a) is the stress cycle at 0.02 mm from the ECT tip on the rake surface. The stress cycle is similar to the points on the rake surface in a sharp tool; there is a stress peak at the beginning of cut, and the stress decreases at the first half of cutting cycle and then increases to another stress peak at end-of-cut. Figure 5.8(b) shows the stress cycle at 0.01 mm from the ECT tip on the flank surface. The peak stress appears when the ECT starts to cut. During the cutting cycle, the stress slightly changes due to the loads on the flank surface. The stress on the flank surface is more steady than the stress on the rake surface because the mechanical and thermal loads on the flank surface are constant during the cutting cycle.

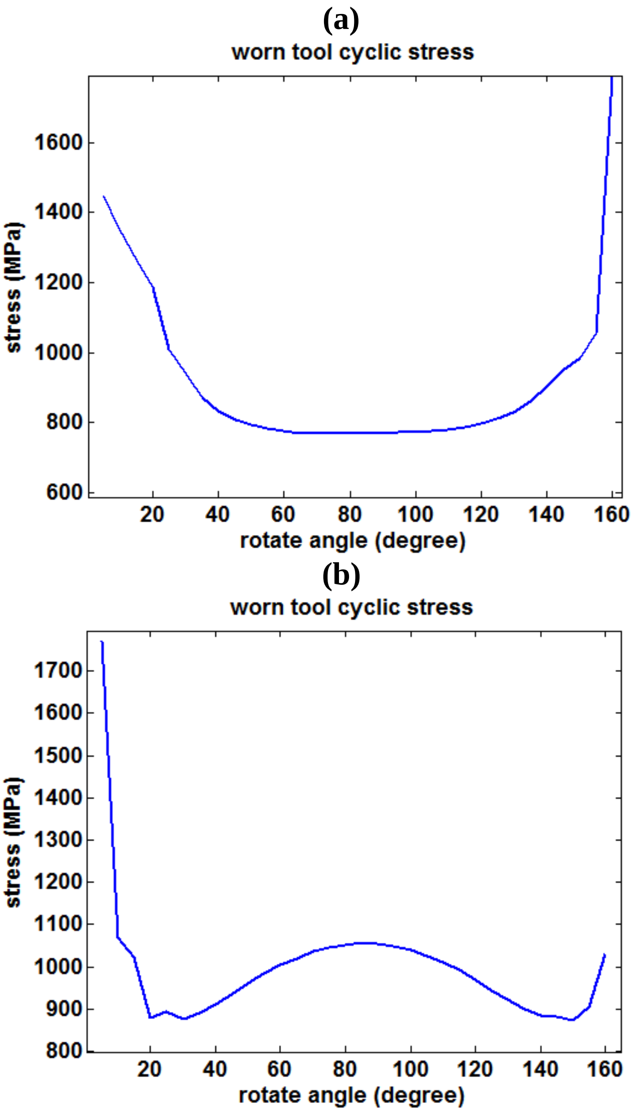

Figure 5.8 Cyclic stress of worn tool (a) on the rake surface 0.017 mm from the ECT tip (b) on the flank surface 0.1 mm from the ECT tip

Finally, from Figure 5.5 and Figure 5.7, it is clearly seen that the maximum stress in the ECT always locates on the rake surface, regardless of the appearance of flank wear. By comparing Figure 5.5 and Figure 5.6 with Figure 5.7 and Figure 5.8, the calculated maximum stress is larger in the worn ECT. This is reasonable due to the extra loading and heat flux on the tool-workpiece contact surface.

From all the modeling results, the maximum stresses under different level of tool wear in the cutting cycle all locate at different position in the tool. For the worst scenario, the maximum stress in the ECT is used in the brittle fracture analysis in order to examine any stress concentration points along the ball-end mill flutes.

5.6 Modified-Mohr Criteria

A criterion for evaluating the stress level is proposed in this session. The tool material used in this study is tungsten carbides, which is one brittle material. Brittle material is sensitive to tensile stress, and is easily to fail under excessive tension. Therefore, the modified Mohr criteria, one commonly used fracture analysis method for brittle material, has been used for examining the maximum stress of every ECT in the cycle.

The principal stresses on the ECT are arranged in order and let

$$\sigma_{\max} = \sigma_A, \tag{5.21}$$

$$\sigma_{\min} = \sigma_B. \tag{5.22}$$

The diagram of the brittle fracture criteria is shown in Figure 5.9.

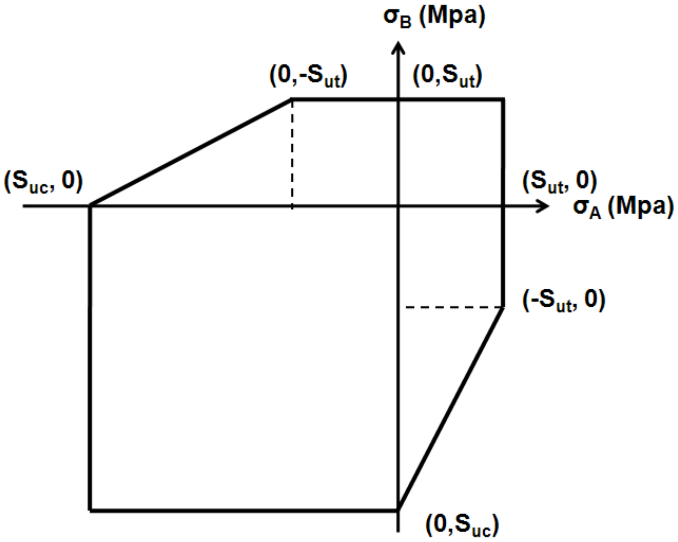

Figure 5.9 Modified Mohr criteria

S_{ut} is the ultimate tensile strength, and S_{uc} is the ultimate compression strength, which is negative. The safety zone is closed in by the linear boundaries formed by the ultimate tensile and compression strength. Therefore, if the maximum and minimum stresses combination falls in the boundaries, the ECT is within reasonable stress load without the possibility of material fracture. WC-Co strength is sensitive to high temperature. Therefore in this study, temperature dependent ultimate tensile and compression strength of WC-Co material were collected from Acchar et al.'s work (1999). The ultimate tensile strength was measured in three point-bending in air at 6 different temperatures between room temperature and 1000°C. Linearly interpolation was used to calculate the material strength in between. The compression strength was assumed to be degraded as the same ratio as the tensile strength with the elevated temperature.

From equation (5.20) and (5.21), the situation in quadrant two will never occur. The criterion is discussed separately for the first, third and fourth quadrant, as shown in Table 5.1. The criteria have been rewritten to a " ratio," as shown in the last column in Table 5.1. Whenever the ratio is larger than 1, the stress level of that ECT is out of the safety region and has high possibility to fail.

Table 5.1: Modified Mohr Criteria

Quadrant	Principle Stresses	Criteria	Ratio
1	$\sigma_A > 0, \sigma_B > 0$	$\sigma_A < S_{ut}, \sigma_B < S_{ut}$	$\frac{\sigma_A}{S_{ut}}, \frac{\sigma_B}{S_{ut}}$
3	$\sigma_A > 0, \sigma_B < 0$	If $\sigma_B > -S_{ut}$, $\sigma_A < S_{ut}$ If $\sigma_B < -S_{ut}$, $\sigma_A - \frac{S_{ut}\sigma_B}{S_{uc} - S_{ut}} < \frac{S_{ut}S_{uc}}{S_{uc} - S_{ut}}$	$\frac{\sigma_A}{S_{ut}}$ $\frac{\sigma_A - \frac{S_{ut}\sigma_B}{S_{uc} - S_{ut}}}{\frac{S_{ut}S_{uc}}{S_{uc} - S_{ut}}}$
4	$\sigma_A < 0, \sigma_B < 0$	$\sigma_A > S_{uc}, \sigma_B > S_{uc}$	$\frac{-\sigma_A}{S_{uc}}, \frac{-\sigma_B}{S_{uc}}$

5.7 Brittle Fracture Analysis along the Ball-end Mill

A ball-end mill design which was observed to have tool chipping at certain location on the long flutes have been analyzed. The principal stresses of each ECT on the flutes in one tool revolution are calculated and the ratio is plotted in Figure 5.10. It is clearly seen that between 0.5 and 0.7 mm height on the flute, there is excessive ratio which indicates high possibility of tool failure.

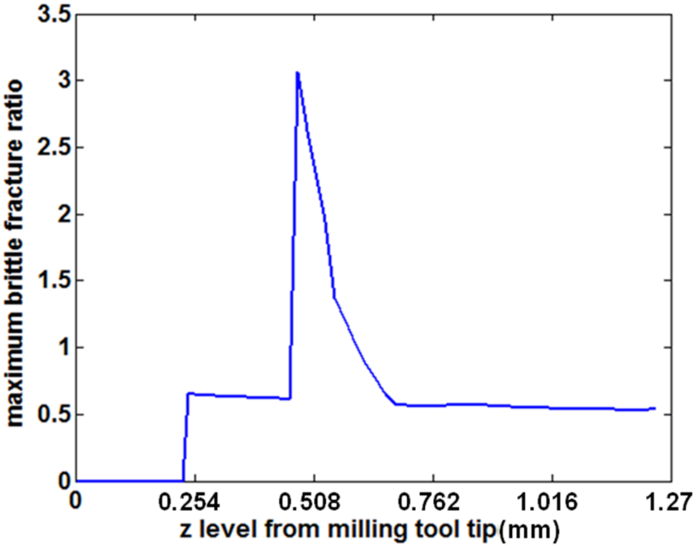

Figure 5.10 The ratio along the flutes in a badly-designed ball-end mill

A photo of the failed tool is shown in Figure 5.11. The tool chipped on the long flutes between the ball-end mill tip and at the height where short flutes start engage in cutting (0.66 mm height from tip). The chipping area is between 0.4 mm to 0.6 mm height from the tool tip and coincides with the identified tool failure location on the ball-end mill in Figure 5.10.

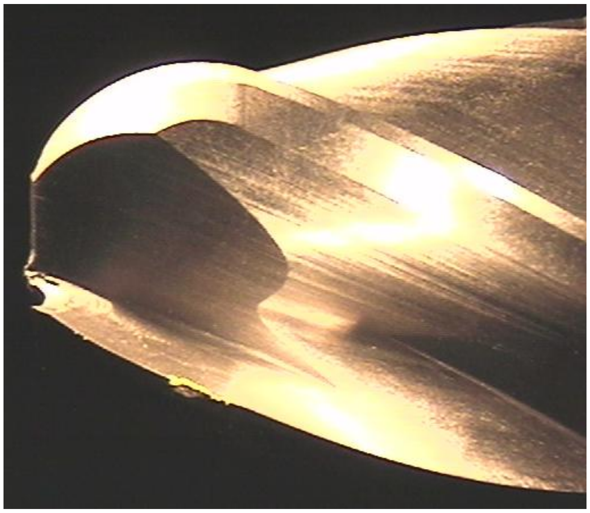

Figure 5.11 Observation of tool failure on the badly-designed tool

From the brittle fracture analysis and the failed tool observation, it is shown that the developed model has the ability to identify the possible failed region on the ball-end mill flute. Therefore, it can be used to examine the CAD model of the new designed tool for evaluating the stress level before a badly-designed tool such as the one in Figure 5.11 is made and tested.

5.8 Conclusions

An analytical model for analyzing the stress of the milling tool is introduced. A new concept is proposed to consider the wedge-shaped ECT as an interaction of two half-plane surfaces and solve the real loads by boundary element method. The boundary load also includes the thermal stress so the thermal and mechanical stresses are not independently considered in the model. The modeling results show that the model is able to estimate the stress distribution inside the tool, the cyclic stress changing during the half cutting cycle and the stress with different tool wear.

Modified-Mohr criteria have been introduced for evaluating the stress level in the tool. The ratio distribution along a badly-design tool is analyzed and compared with the observation of the failed tool. It is shown that the model has the ability to identify the high risk chipping region on the ball-end mill and can be used to analyze the stress of the new designed CAD model before manufacturing and testing.

CHAPTER 6
CONCLUSIONS

6.1 Conclusions

Titanium milling is considered a critical machining process in high-end technology. The high strength, light weight and good mechanical resistance of titanium alloys make them precious materials in both aerospace and bio-technology. Milling process is also non-replaceable because it has the ability to machine any kind of shapes. The traditional method for analyzing the milling process and designing the milling tool is time-consuming and costly experiments. In this study, several models address the important parameters in the titanium milling processes are developed and validated. These models are expected to replace the experimental approach and provide some insight for improving titanium milling technology.

The study of cutting force modeling is the first important step in the evaluation of the tool performance. Based on the literature review, the existed models were limited because they were only feasible when the cutter geometry was defined by certain parameters. Therefore, a mechanistic model with the capability to analyze arbitrary ball-end mill geometry is proposed. The cutter geometry data is directly extracted from the CAD model, including the point coordinates and the vectors normal to both rake and flank surfaces. A novel uncut chip calculation method is proposed in the study to replace the existing sinusoidal function approximation of chip load calculation method. With both improvements, the cutting force model is able to predict the force for more tool geometry variation and for new tool designs in the future. The model also considers if there is appearance of flank wear. The cyclic forces of worn tool from modeling and experimental results match very well. Most important of all, this study provides basis knowledge for the further tool performance analysis in the following chapters.

The estimation of temperature is able to model the transient temperature in milling process with considering both the cooling and flank wear effects. The model uses the heat generation from the forces predicted by the model. The generated heat is varying during the milling process. The changing tool-chip contact length, which is also the heat input length, is considered by determining whether the elements on the rake surface are within the contact length or not. Moreover, whenever the elements are not contact with chip, they are exposed to the coolant and the heat convection is included in the temperature modeling process. The extra heat generated due to the friction between the flank wear and workpiece is modeled in the study, too. Finally, the tool-copper thermocouple method has been applied for the measuring of cutting temperature in the milling process. The method has been redesigned by changing the position of embedded copper foil, and is able to measure temperature of different ECT on the tool and obtain convincing results.

The tool wear study introduces an integrated model which combines several literature models for tool wear progression estimation from a sharp tool. The iteration between the cutting forces and the tool wear solves the limitation that in literature people needed to know one or the other to complete the model. From the proposed method, the only calibration experiment needs to be done is for the force coefficients in the force model. Thus with the same materials, new tool design can be used in the model and the tool wear progression under different cutting conditions can be estimated and evaluated. Moreover, with assumed flank wear criterion, the tool life of the new design tool is able to be predicted. A series of validation experiments have been conducted to compare the modeling and experimental tool lives. Most cutting conditions show convincing results except for one particular condition that tool run-out has been observed to cause the discrepancy.

The last study is the thermo-mechanical stress analysis of the tool. This study proposed an analytical method which considers the wedge-shaped tool tip as two interacting half-plane spaces, and includes the forces on both rake and flank surfaces as the prescribed loads. The prescribed loads are resulted from the real load, the resultant stress from the other surface and the thermal stress. Boundary element method is used to solve the loading situation and find the real loads on both surfaces. Thus the model not only includes the stresses from both surfaces but also combines the thermal and mechanical stresses. The modeling results have been shown and discussed. Finally, brittle fracture analysis with modified-Mohr criteria is used to analyze the stress distribution along the ball-end mill flute. The high risk region of tool failure is identified from the analysis and tool chipping at the same region has been observed on the tested tool.

Each of the study in this research is an individual model for analyzing the titanium milling process. They are also closely related with each other and a lot of information is shared between each other. The mechanistic force model and the temperature model both consider the flank wear effects so they can be applied for the tool wear estimation and stress analysis. Two different kinds of tool failure modes of titanium milling process have been covered in this study. The tool can be evaluated under the wear criterion and the stress criteria to examine the tool performance from the CAD design. With the use of the developed models, the new designed tools can be evaluated by the models instead of the manufacturing process and the trial-and-error tests. Also, the cutting condition is another input which can be varied and better cutting efficiency can obtained. In summary, each chapter of this research has individual contributions. At the same time, the whole study provides a complete view for evaluating the tool performance in the milling of titanium alloys.

6.2 Recommendations for Future Study

The analysis in this study already covered different aspects when analyzing the tool performance. However, there are still some further researches needed to make the whole analysis more completed. One of the direction is to include more practical issue such as tool run-out, deflection, chatter and other machining stability problems. In this study all the models are assumed to be under ideal cutting process. Although ideally we would like to eliminate all these problems and make the cutting process stable, it is not possible in real world.

The stress calculation provides a modeling technique to analyze the stress distribution on the ball-end mill. However, it will be more convincing if the stress can be validated by experiments. Moreover, there are a lot of variation and information that can be dig out and utilized for further tool performance analysis. One possible direction is to use the stress to investigate the crack growth process. Except for excessive stress, the growing of micro cracks inside of the material will lead to tool chipping, too. From the crack growing progression, the tool failure time can be estimated and provided another point of view for tool life modeling.

Another future direction is to include the edge preparation, such as the edge radius and honed edge, into the models. Before this study started, there was lack of technique to properly control and measure the cutting edge on the ball-end mill. Thus we assumed the edge to be sharp in the models. However, the edge preparation may result in larger utting force and temperature; at the same time, it may provide higher strength at the tool tip and avoid tool chipping. Thus, edge preparation will affects tool life significantly and the models would be more accurate and complete with considering the edge preparation.

In the experiments, chip evacuation sometimes may cause problems. They were not the dominant tool failure modes but they influenced the cutter performance. Chip welding on the rake surface and chip clogging inside of the flute area will increase the cutting force, cutting temperature and degrade the cutter. Moreover, the welding chip might change the rake angle and result in different cutter geometries in the models. Thus, proper modeling technique for chip flows and chip temperature will also contribute to the titanium milling process and make the study more complete.

Another future direction is to use all the developed models for tool geometry optimization to obtain maximum tool life. The objective function can be the tool life, and with constraint functions including cutting force, temperature and brittle fracture ratio. Under different cutting conditions, the optimized geometry will be different. This topic will contribute to develop a scientific means of designing new milling tools.

REFERENCES

Abukhshim, N.A., Mativenga, P.T. and Sheikh, M.A., “Heat generation and temperature prediction in metal cutting: A review and implications for high speed machining,” *International Journal of Machine Tools and Manufacture*, 46(7-8), 2006, p782-800

Acchar, W., Gomes, U.U., Kaysser, W.A. and Goring, K., “Strength degradation of a tungsten carbide-cobalt composite at elevated temperatures,” *Materials Characterization*, 43, 1999, p27-32

Agaiou, J.S. and Stephenson, D.A., “Analytical and experimental studies of drill temperature,” *Transactions of ASME*, 116, 1994, p54-60

Alauddin, M., Baradie, M.A. and Hashmi, M.S.J., “Prediction of tool life in end milling by response surface methodology,” *Journal of Materials Processing Technology*, 71, 1997, p456-465

Amaitik, S.M., Tasgin, T.T. and Kilic, S.E., “Tool-life modeling of carbide and ceramic cutting tools using multi-layer regression analysis,” *IMechE*, 220, 2006, p129-136

Archard, J.F., “Contact and rubbing of flat surfaces,” *Journal of Applied physics*, 24(8), 1953, p981-988

Acchar, W., Gomes, U.U., Kaysser, W.A., Goring, J., ” Strength degradation of a tungsten carbide-cobalt composite at elevated temperatures,” *Materials Characterization*, 43, 1999, p27-32

Archibald, F.R., “Analysis of stresses in cutting edge,” *Transactions of ASME*, 78(6), 1956, p1149-1154

Arsecularatne, J.A. and Oxley, P.L.B., “Prediction of cutting forces in machining with restricted contact tools,” *Machining Science and Technology*, 1(1), 1997, p95-112

Arsecularatne, J.A., “On tool-chip interface stress distributions, ploughing force and size effect in machining,” *International Journal of Machine Tools and Manufacture*, 37(7), 1997, p885-899

Arsecularatne, J.A., Zhang, L.Z. and Montross, C., “Wear and tool life of tungsten carbide, PCBN and PCD cutting tools,” *International Journal of Machine Tools and Manufacture*, 46, 2006, p482-491

Astakhov, J.P. and Outeiro, J.C., “Modeling of the contact stress distribution at the tool-chip interface,” *Machine Science and Technology*, 9, 2005, p85-99

Bagghi, A. and Wright, P.K., “Stress Analysis in machining with the use of sapphire tools,” *Proceedings of The Royal Society of London, Series A: Mathematical and Physical Sciences*, 409(1836), 1987, p99-113

Barrow, G., Graham, W., Kurimoto, T. and Leong, Y.F., “Determination of rake faces stress distribution in orthogonal machining,” *International Journal of Machine Tool Design and Research*, 22, 1982, p75-85

Berliner, E.M. and Krainov, V.P., “Analytical calculations of the temperature field and heat flows on the tool surface in metal cutting due to sliding friction,” *Wear*, 143, 1991, p379-395

Bhatia, S.M., Pandey, P.C. and Shan, H.S., “The thermal condition of the tool cutting edge in intermittent cutting,” *Wear,* 61, 1980, p21-30

Bhatia, S.M., Pandey, P.C. and Shan, H.S., ”The thermal condition of the tool cutting edge in intermittent cutting,” *Wear*, 61, 1980, p21-30

Bono, M. and Ni, J., “A method for measuring the temperature distribution along the cutting edges of a drill,” *Journal of Manufacturing Science and Engineering - Technical Briefs*, 124, 2002, p921-923

Bono, M. and Ni, J., “The location of the maximum temperature on the cutting edges of a drill,” *International Journal of Machine Tools and Manufacture*, 46, 2006, p901-907

Budak, E., Altinta, Y. and Armerego, E.J.A., “Prediction of milling force coefficients from orthogonal cutting data,” *Transactions of ASME*, 118, 1996, p216-224

Buryta, D., Sowerby, R., Yellowley, I., “Stress distribution on the rake face during orthogonal machining,” *International Journal of Machine Tools and Manufacture*, 34(5), 1994, p721-739

Chakraborty, P., Asfourm, S., Cho, S., Onar, A., and Lynn, M., “Modeling tool wear progression by using mixed effects modeling technique when end-milling AISI 4340 steel,” *Journal of Materials Processing Technology*, 205, 2008, p190-202

Chakraverti, G., Pandey, P.C. and Mehta, N.K., “Analysis of tool temperature fluctuation in interrupted cutting,” *Precision Engineering*, 6(2), 1984, p99-105

Challen, J.M. and Oxley, P.L.B., “An explanation of the different regimes of friction and wear using asperity deformation models,” *Wear,* 53, 1979, p229-243

Challen, J.M., Oxley, P.L.B. and Hockenhull, B.S., ”Prediction of Archard’s wear coefficient for metallic sliding friction assuming a low cycle fatigue wear mechanism,” *Wear*, 111, 1986, p275-288

Chandrasekaran, H. and Nagarajan, R., “On certain aspects of transient stresses in cutting tools,” *Journal of Engineering for Industry*, 102, 1980, p133-141

Chandrasekaran, H., “Friction and contact stress modeling in a cutting tool during single tooth fly milling of steel,” *Tribology Aspects in Manufacturing*, 2, 1991, p265-278

Chandrasekaran, H., “Friction in machining- comparison of rake and flank wear-land friction,” *Wear*, 36, 1976, p133-145

Chandrasekharan, V., “A model to predict the three-dimensional cutting force system for drilling with arbitrary point geometry,” *PhD Thesis, University of Illinois at Urbana-Champaign*, 1996

Chandrasekharan, V., Kapoor, S.G. and DeVor, R.E., ”Mechanistic approach to predicting the cutting forces in drilling: With application to fiber-reinforced composite materials”, *Journal of engineering for industry*, 117(4), 1995, p559-570

Che Haron, C.H., Ginting, A. and Arshad, H., “Performance of alloyed uncoated and CVD-coated carbide tools in dry milling of titanium alloy Ti-6242S,” *Journal of Materials Processing Technology*, 185, 2007, p77–82

Chiang, S., Tsai, C. and Lee, A., “Analysis of cutting forces in ball-end milling,” *Journal of Materials Processing Technology*, 47, 1995, p231-249

Childs, T.H.C., Maekawa, K. and Maulik, P., “Effects of coolant on temperature distribution in metal machining,” *Materials Science and Technology*, 4, 1988, p1006-1019

Cook, N.H., “Tool wear and tool life,” *Transactions of ASME*, 93, 1973, p931-938

Da Silva, M.B. and Wallbank, J., “Cutting temperature: prediction and measurement methods - a review,” *Journal of Materials Processing Technology*, 88(1), 1999, p195-202,

Dawson, P.R. and Malkin, S., “Inclined moving heat source model for calculating metal cutting temperatures,” *Journal of Engineering for Industry*, 106, 1984, p179-186

DeVor, R.E., Anderson, D.L. and Zdeblick, W.J., “Tool life variation and its influence on the development of tool life models,” *Transactions of ASME*, 99(3), 1977, p578-589

DeVor, R.E., Kline, W.A. and Zdeblick, W.J., “A mechanistic model for the force system in end milling with application to machining airframe structures,” *Manufacturing Engineering Transactions*, 1980, p297-30

Endres, W.J., DeVor, R.E. and Kapoor, S.G., “A dual-mechanism approach to prediction of machining forces: Part I- model development and calibration,” *Transactions of ASME*, 64, 1993, p563-576

Engin, S. and Altintas, Y., “Mechanics and dynamics of general milling cutters. Part I: helical end mills,” *International Journal of Machine Tools and Manufacture*, 41, 2001, p2195-2212

Ezugwu, E. O., Bonney, J., Da Silva, R.B. and Çakir, O., ”Surface integrity of finished turned Ti–6Al–4V alloy with PCD tools using conventional and high pressure coolant supplies,” *International Journal of Machine Tools and Manufacture*, 47, 2007, p884-891

Ezugwu, E.O. and Wang, Z.M., “Titanium alloys and their machinability – a review,” *Journal of Materials Processing Technology*, 68, 1997, p262-274

Feng, H.-Y. and Menq, C.-H., “The prediction of cutting forces in the ball-end milling process – I. Model formulation and mode building procedure,” *International Journal of Machine Tools and Manufacture*, 34(5). 1994, p697-710

Froes, F.H., “Innovations in titanium technology,” *Materials Technology*, 22(2), 2007, p101-104

Fu, S.J., DeVor, R.E. and Kapoor, S.G., “Mechanistic model for the prediction of the force system in face milling operation,” *Journal of engineering for industry*, 1984, 106(1), p81-88

Geng, G.S. and Xu, J.H., “Experimental Study on High Speed Machining of a Titanium Alloy,” *Advanced Materials Research*, 69-70, 2009, p451-455

Ginting, A. and Nouari, M., “Experimental and numerical studies on the performance of alloyed carbide tool in dry milling of aerospace material,” *International Journal of Tools and Manufacture*, 46, 2002, p758-768

Ginting, A. and Nouari, M., “Optimal cutting conditions when dry end milling the aeroengine material Ti-6242S,” *Journal of Materials Processing Technology*, v184, 2007 p319-324

Goldstein, R.J. and Franchett, M.E., “Heat transfer from a flat surface to an oblique impinging jet,” *Transactions of ASME*, 110, 1988, p84-90

Hitomi, K., Nakamura, N. and Inoue, S., “Reliability analysis of cutting tools,” *Transactions of ASME*, 101, 1979, p185-190

Holman, J.P., *Heat Transfer*, McGraw-Hill, New York, 1992

Huang, Y. and Liang, S.Y., “Modeling of CBN tool flank wear progression in finish hard turning,” *Transactions of ASME*, 126, 2004, p98-106

Hughes, J. I., Sharman, A.R.C. and Ridgway, K., ”The effect of cutting tool material and edge geometry on tool life and workpiece surface integrity,” *IMechE*, 220, 2006, p93-107

Hutching, I.M., *Tribology: Friction and Wear of Engineering Materials*, CRC Press, BocaRaton, 1992

Johnson, K.L., *Contact Mechanics*, Cambridge University Press, 1987

Kannatey-Asibu, E. Jr., ”A transport-diffusion equation in metal cutting and its application to analysis of the rate of flank wear,” *Journal of Engineering for Industry*, 107, 1985, p81-89

Karpat, Y. and Özel, T., ”Predictive analytical and thermal modeling of orthogonal cutting process – Part II: Effect of tool flank wear on tool forces, stresses and temperature distribution,” *Journal of Manufacturing Science and Engineering*, 128, 2006, p445-453

Kato, K. “Classification of wear mechanisms/models,” *IMechE*, 216, 2002, p349-355

Kato, S., Yamaguchi, K. and Yamada, M., ”Stress distribution at the interface between the tool and chip in machining,” *Journal of Engineering for Industry,* 98, 1972, p683-689

Klim, Z., Ennajimi, E., Balazinski, M. and Fortin, C., “Cutting tool reliability analysis for variable feed milling of 17-4PH stainless steel,” *Wear*, 195, 1996, p206-213

Kline, W.A., DeVor, R.E. and Lindberg, J.R., “The prediction of cutting forces in end milling with application to cornering cuts,” *International Journal of Machine Tool Design and Research*, 22(1), 1982, p7-22

Komanduri, R. and Hou, Z.B., “Thermal modeling of the metal cutting process Part I – Temperature rise distribution due to shear plane heat source,” *International Journal of Mechanical Sciences*, 42, 2000, p715-1752

Komanduri, R. and Hou, Z.B., “Thermal modeling of the metal cutting process Part II – Temperature rise distribution due to frictional heat source at the tool-chip interface, *International Journal of Mechanical Sciences*, 43, 2000, p57-88

Komanduri, R. and Reed, W.R., “Evaluation of carbide grades and a new cutting geometry for machining titanium alloys,” *Wear*, 92, p113-123, 1983

Kovacevic, R., Cherukuthota, C. and Mazurkiewicz, M., “High pressure waterjet cooling/lubrication to improve machining efficiency in milling,” *International Journal of Machine Tools and Manufacture*, 35(10), 1995, p 1459-1473

Kurt, A., “Modeling of the cutting tool stresses in machining of Inconel 718 using artificial neural networks,” *Expert Systems with Applications*, 36, 2009, p9645-9657

Lazoglu, I. and Altintas, Y., “Prediction of tool and chip temperature in continuous and interrupted machining,” *International Journal of Machine Tools and Manufacture*, 42, 2002, p1011-1022

Lee, P. and Altintas, Y., “Prediction of ball-end milling forces from orthogonal cutting data,” *International Journal of Machine Tools and Manufacture*, 36(9), 1995, p1059-1072

Li, K. and Liang, S.Y., ”Modeling of cutting forces in near dry machining under tool wear effect,” *International Journal of Machine Tools and Manufacture*, 47, 2007, p1292-1301

Li, K.-M. and Liang, S.Y., “Predictive models for flank wear in near dry machining,” *ASME Manufacturing Engineering Division*, 16(1), 2005, p49-51

Li, K.-M. and Liang, S.Y., “Predictive modeling of flank wear in turning under flood cooling,” *Journal of Manufacturing Science and Engineering*,” 129, 2007, p513-519

Li, X., “Study of jet-flow rate of cooling in machining Par 1. Theoretical analysis,” *Journal of Materials Processing Technology*, 62, 1996, p149-156

Li, X., “Study of jet-flow rate of cooling in machining Part 2. Simulation Study,” *Journal of Materials Processing Technology*, 62, 1996, p157-165

Lin, S.Y., Lin, J.C., Lin, C.C., Jywe, W.Y. and Lin, B.J., “Life prediction system using a tool’s geometric shape for high-speed milling,” *International Journal of Advanced Manufacturing Technology*, 30, 2006, p622-630

Loewen, E.G. and Shaw, M.C., “On the analysis of the cutting-tool temperatures,” *Transactions of ASME*, 76, 1954, p217-231

López de lacalle, L.N., Pérez, J., Llorente, J.I. and Sánchea, J.A., “Advanced cutting conditions for the milling of aeronautical alloys,” *Journal of Materials Processing Technology*, 100, 2002, p1-11

Lu, Y., Takeuchi, Y., Takahashi, I. and Anzai, M., “An integrated system development for ball end milling design, creation and evaluation,” *International Advanced Manufacture Technology*, 25, 2005, p628-646

Luo, X., Cheng, K., Holt, R. and Liu, X., “Modeling flank wear of carbide tool insert in metal cutting,” *Wear*, 259, 2005, p1235-1240

Mari, D. and Gonseth, D.R., “A new look at carbide tool life,” *Wear*, 165, 1993, p9-17

Meng, H.C. and Ludema, K.C., “Wear models and predictive equations: their form and content,” *Wear*, 181(183), 1995, p443-457

Merchant, M.E., “Basic mechanics of the metal-cutting process,” *Journal of Applied Mechanics*, 11, 1944, pA168-A175

Meyer, K., “Milling tool performance analysis in high speed milling of titanium alloys,” *Master Thesis, University of Michigan at Ann Arbor*, 2007

Milman, Y.V., Chugunova, S. and Goncharuck, V., “Low and high temperature hardness of WC-6% Co alloys*,” International Journal of Metals and Hard Materials*, 15, 1997, p97-101

Molinari, A., and Nouari, M., “Modeling of tool wear by diffusion in metal cutting,” *Wear*, 252, 2002, p135-149

Monaghan, J. and MacGinley, T., “Modeling the orthogonal machining process using coated carbide cutting tools,” *Computational Materials Science*, 16, 1999, p275-284

Nandy, A. K. and Paul, S., ”Effect of coolant pressure, nozzle diameter, impingement angle and spot distance in high pressure cooling with neat oil in turning Ti-6Al-4V,” *Machining Science and Technology*, 12, 2008, p445-473

Nurul Amin, A.K.M., Ismail, A.F. and Khairusshima, M.K., “Effectiveness of uncoated WC-Co and PCD inserts in end milling of titanium alloy – Ti-6Al-4V,” *Journal of Materials Processing Technology*, 192-193, 2007, p147-158

Okushim, K. and Hoshi, T., “Thermal crack in carbide face-milling cutter - 2nd report. Its significance as cause of tool failures,” *Japan Society of Mechanical Engineers -- Bulletin*, 6 (22), 1963, p317-326

Ong, P.K.L. and Manna, M.A., ”Experimental modeling of cutting forces as a function of tool wear in end miling,” *Material Science Forum*, 437-438, 2003, p371-374

Oxley, P.L.B., “Mechanics of metal cutting,” *International Journal of Machine Tool Design and Research*, 1(1-2), 1961, p89-97

Palanisamy, P., Ragendran, I. and Shanmugasundaram, S., “Prediction of tool wear using regression and ANN models in end-milling operation,” *International Journal of Advanced Manufacturing Technology*, 37, 2008, p29-41

Pan, Y.Z., Ai, X., Zhao, J. and Fu, X.L., “Tool-Life Optimization in High-Speed Milling of Aeronautical Aluminum Alloy 7050-T7451,” *Materials Science Forum*, 626-627, 2009, p117-122

Pirso, J., Ziljus, M. and Letunovitš, S., ”Friction and dry sliding wear behavior of cermets,” *Wear*, 260, 2006, p815-824

Rabinowicz, E., Dunn, L.A. and Russel, P.G., ”A study of abrasive wear under three-body conditions,” *Wear*, 4, 1961, p345-355

Radulescu, R. and Kapoor, S.G., “An analytical model for prediction of tool temperature fields during continuous and interrupted cutting,” *Journal of Engineering for Industry*, 116(2), 1994, p135-143

S.Sharma, V., Dogra, M. and Suri, N.H., ”Cooling techniques for improved productivity in turning,” *International Journal of Machine Tools and Manufacture*, 49, 2009 p435-453

Shatla, M. and Altan, T. “Analytical modeling of drilling and ball end milling,” *Journal of Materials Processing Technology*, 98, 2000, p125-133

Shaw, M.C. and Dirke, S.O., ”On the wear of cutting tools,” *Microtecnic*, 10(4), 1956 , p187

Shaw, M.C., Cook, N.H. and Smith, P.A., “Mechanics of three-dimensional cutting operation,” *Transactions of ASME*, 74(6), 1952, p1055-1064

Skidar,C., Paul, S. and Chattopadhyay, A.B., “Effect of variation in edge geometry on wear and life of coated carbide face milling inserts,” *Wear*, 157, 1992, p111-126

Smithey, D.W., Kapoor, S.G. and DeVor, R.E., ”A new mechanistic model for predicting worn tool cutting forces,” *Machine Science and Technology*, 40, 2000, p1929-1950

Smithey, D.W., Kapoor, S.G. and DeVor, R.E., ”A worn force model for three-dimensional cutting operations,” *Machine Tools and Manufacture*, 5(1), 2001, p23-42

Stephenson, D.A. and Agapior, J.S., *Metal Cutting Theory and Practice*, Marcel Dekker, Inc. 1997

Stephenson, D.A. and Ali, A., “Tool temperature in interrupted metal cutting,” *Journal of Engineering for Industry*, 114, 1992, p127-136

Stephenson, D.A., “Assessment of steady-state metal cutting temperature models based on simultaneous infrared and thermocouple data,” *Journal of Engineering for Industry*, 113, 1991, p121-128

Su, Y., He, N., Li, Li and Li, X.L., ”An experimental investigation of effects of cooling/lubrication conditions on tool wear in high-speed end milling of Ti-6Al-4V,” *Wear*, 261, 2006, p760-766

Sun, J., Wong, Y.S., Rahman, M., Wang, Z.G., Neo, K.S., Tan, C.H. and Onozuka, H., “Effects of coolant supply methods and cutting conditions on tool life in end milling titanium alloy,” *Machining Science and Technology*, 10, 2006, p355-370

Tai, C. and Fuh, K., “A predictive force model in ball-end milling including eccentricity effects*,” International Journal of Machine Tools and Manufacture*, 34(7), 1994, p959-979

Tai, C. and Fuh, K., “Model for cutting forces prediction in ball-end milling,” *International Journal of Machine Tools and Manufacture*, 34(7), 1995, p511-534

Teitenberg, T.M., Bayoumi, A.E. and Yucesan, D., ”Tool wear modeling through an analytical mechanistic model of milling processes,” *Wear*, 154, 1992, p287-304

Tolouei-rad, M. and Bidhendi, I.M., “On the optimization of machining parameters for milling operations,” *International Journal Machine Tools and Manufacture*, 37(1), 1997, p1-16

Trigger, K.J. and Chao, B.T., “The mechanism of crater wear of cemented carbide tools, *Transactions of ASME*, 78(5), 1956, p1119

Tsai, M.K., Lee, M.Y. and Yu, S.F., “A prediction modeling of tool life of high-speed milling for SKD61 tool steel,” *International Journal of Advanced Manufacturing Technology*, 26, 2005, p711-717

Uehara, K., “Fundamental approach to the thermal crack of cermet cutting tools,” *Annals of the CIRP*, 30, 1981, p47-51

Upadhyaya, G.S., *Cemented Tungsten Carbides*, Noyes Publication, 1998

Usui E. and Shirakashi, T., “Analytical prediction of cutting tool wear,” *Wear*, 100, 1984, p129-151

Usui, E. and Takeyama, H., “A photoelastic analysis of machining stress,” *Journal of Engineering for Industry*, 82(4), 1960, p303-307

Usui, E., Sharakashi, T., and Kitagawa, T., ”Analytical prediction of three dimensional cutting process, Part 3: Cutting temperature and crater wear of carbide tool,” *Journal of Engineering for Industry*, 100, 1978, p236-243

Wager, J.G. and Barash, M.M., “Study of distribution of the life of HSS tools,” *Transactions of ASME*, 73(4), 1971, p295-299

Wang, J.-J. J. and Zheng, C.M., “Identification of shearing and ploughing cutting constants from average forces in ball-end milling,” *International Journal of Machine Tools and Manufacture*, 42, 2002, p695-705

Woldorf, D.J., DeVor, R.E. and Kapoor, S.K., ”A slip-line field for ploughing during orthogonal cutting,” *Journal of Manufacturing Science and Engineering*, 120, 1998, p693-699

Wu, W., and Mayer, J.E., “Analysis of thermal cracking of carbide tools in intermittent,” *Journal of engineering for industry*, 101(2), 1979, p159-164

Yang, M. and Park, H., “The prediction of cutting force in ball-end milling,” *International Journal of Machine Tools and Manufacture*, 31(1), 1991, p45-54

Yűcesan, G. and Altintas, Y., “Prediction of ball end milling forces,” *Journal of Engineering for Industry*, 118, 1996, p95-103

Yun, W.-S. and Cho, D.-W., “Accurate 3-D cutting force prediction using cutting condition independent coefficients in end milling,” *International Journal of Machine Tools and Manufacture*, 41, 2001, p463-478

Zelinski, P., “The Right Tool for Milling Titanium,” *Modern Machine Shop*, January 2004

Zhang, Z., Zheng,, L., Zhang, L., Li, Z., Liu, D. and Zhang, B., ”A study on calibration o coefficients in end milling forces model,” *International Journal of Advanced Manufacturing Technology*, 25, 2005, p652-662

Zhao, H., Barber, G.C. and Zou, Q., ”A study of flank wear in orthogonal cutting with internal cooling,” *Wear*, 253, 2002, p957-962

Zhou, J.M., Sturesson, P.O., Sandzvist, H. and Ståhl, J.E., “An approach for on-line cutting edge stress estimation,” *International Journal of Machine Tools and Manufacture*, 34(5), 1994, p741-751